



HAL
open science

Predicting HCN, HCO⁺, multi-transition CO, and dust emission of star-forming galaxies. Constraining the properties of resolved gas and dust disks of local spiral galaxies

Thomas Lizée, Bernd Vollmer, Jonathan Braine, Pierre Gratier, Frank Bigiel

► To cite this version:

Thomas Lizée, Bernd Vollmer, Jonathan Braine, Pierre Gratier, Frank Bigiel. Predicting HCN, HCO⁺, multi-transition CO, and dust emission of star-forming galaxies. Constraining the properties of resolved gas and dust disks of local spiral galaxies. *Astronomy and Astrophysics - A&A*, 2022, 663, 10.1051/0004-6361/202142480 . insu-03764720

HAL Id: insu-03764720

<https://insu.hal.science/insu-03764720>

Submitted on 1 Sep 2022

HAL is a multi-disciplinary open access archive for the deposit and dissemination of scientific research documents, whether they are published or not. The documents may come from teaching and research institutions in France or abroad, or from public or private research centers.

L'archive ouverte pluridisciplinaire **HAL**, est destinée au dépôt et à la diffusion de documents scientifiques de niveau recherche, publiés ou non, émanant des établissements d'enseignement et de recherche français ou étrangers, des laboratoires publics ou privés.



Distributed under a Creative Commons Attribution 4.0 International License

Predicting HCN, HCO⁺, multi-transition CO, and dust emission of star-forming galaxies

Constraining the properties of resolved gas and dust disks of local spiral galaxies

T. Lizée¹ , B. Vollmer¹, J. Braine², P. Gratier², and F. Bigiel³

¹ Université de Strasbourg, CNRS, Observatoire Astronomique de Strasbourg, UMR 7550, 67000 Strasbourg, France
e-mail: thomas.lizee@astro.unistra.fr

² Laboratoire d'Astrophysique de Bordeaux, Univ. Bordeaux, CNRS, B18N, Allée Geoffroy Saint-Hilaire, 33615 Pessac, France

³ Argelander-Institut für Astronomie, Universität Bonn, Auf dem Hügel 71, 53121 Bonn, Germany

Received 19 October 2021 / Accepted 2 May 2022

ABSTRACT

The interstellar medium is a turbulent, multiphase, and multi-scale medium that follows scaling relations that link the surface density, volume density, and velocity dispersion with the cloud size. Galactic clouds range from below 1 pc to about 100 pc in size. Extragalactic clouds appear to follow the same range, although they are only now becoming observable in atomic and molecular lines. Analytical models of galactic gaseous disks need to take the multi-scale and multiphase nature of the interstellar medium into account. They can be described as clumpy star-forming accretion disks in vertical hydrostatic equilibrium, with the mid-plane pressure balancing the gravity of the gaseous and stellar disk. Interstellar medium turbulence is taken into account by applying Galactic scaling relations to the cold atomic and molecular gas phases. Turbulence is maintained through energy injection by supernovae. With the determination of the gas mass fraction at a given spatial scale, the equilibrium gas temperature between turbulent heating and line cooling, the molecular abundances, and the molecular line emission can be calculated. The resulting model radial profiles of infrared, HI, CO, HCN, and HCO⁺ emission are compared to THINGS, HERACLES, EMPIRE, SINGS, and GALEX observations of 17 local spiral galaxies. The model free parameters were constrained for each galactic radius independently. The Toomre parameter, which measures the stability against star formation (cloud collapse), exceeds unity in the inner disk of a significant number of galaxies. In two galaxies it also exceeds unity in the outer disk. Therefore, in spiral galaxies $Q_{\text{tot}} = 1$ is not ubiquitous. The model gas velocity dispersion is consistent with the observed HI velocity dispersion where available. Within our model, HCN and HCO⁺ is already detectable in relatively low-density gas ($\sim 1000 \text{ cm}^{-3}$). We derive CO and HCN conversion factors and molecular gas depletion times. Both conversion factors are consistent with values found in the literature. Whereas in the massive galaxies the viscous timescale greatly exceeds the star-formation timescale, the viscous timescale is smaller than the star-formation timescale within $R \sim 2R_d$, the disk scale length, in the low-mass galaxies. We suggest that massive spiral galaxies undergo starvation in the absence of gas accretion from the halo, whereas in low-mass galaxies the fuel for star formation reaches $R \sim 2R_d$ from outside via a thick gas disk component with a high radial infall velocity observable in the HI line.

Key words. galaxies: ISM – galaxies: evolution – galaxies: star formation

1. Introduction

The interstellar medium (ISM) of spiral galaxies involves multiple scales, multiple densities and temperatures, and multiple phases (ionized, atomic, and molecular). The observed gas velocity dispersions ($\sim 10 \text{ km s}^{-1}$ in the atomic gas and several km s^{-1} in the molecular gas) indicate that the ISM is supersonically turbulent. Within the star-forming disk, turbulence is triggered by thermal instabilities and maintained by the energy injection through stellar feedback. Scaling relations for giant molecular clouds (GMCs) were first established by Larson (1981): power-law relationships between the velocity dispersion and the gas density on the one hand and the size of the emitting regions on the other. The power-law indices were refined by, for example, Heyer et al. (2009) and Lombardi et al. (2010). Galactic HI scaling relations were established by Larson (1979) and Quiroga (1983) and used in the two-phase HI model of the Galaxy by Wolfire et al. (2003).

The molecular gas depletion time, $t_{\text{dep,H}_2} = M_{\text{H}_2}/\text{SFR}$, measured at kiloparsec scales in large spiral galaxies is about constant with $t_{\text{dep,H}_2} \sim 2 \text{ Gyr}$ (e.g., Kennicutt 1998a,b; Bigiel et al. 2008; Leroy et al. 2008; Ellison et al. 2021). This relation between the molecular gas mass and the star-formation rate (SFR) breaks down at scales smaller than a few hundred parsecs (Bigiel et al. 2011; Kruijssen & Longmore 2014; Schinnerer et al. 2019) because of the life cycle of the star-formation process. At the scale of individual GMCs, regions of massive star formation and cold molecular gas are not correlated because subsequent phases of the star-formation process are observed. At these scales, gas depletion times up to 17 times shorter than those of nearby galaxies (Heideman et al. 2010) or broken power laws (Retes-Romero et al. 2017) were found.

The star-formation efficiency, which is the inverse of the gas depletion time, depends on the determination of the molecular gas mass, which is hampered by the uncertainty of the conversion between the observed line emission (mostly CO, but

also HCN and HCO⁺ for dense gas) and the mass of molecular hydrogen. Whereas the Galactic CO conversion factor is well established ($\alpha_{\text{CO}} = \Sigma_{\text{H}_2}/I_{\text{CO}} = 4.3 M_{\odot} \text{pc}^{-2} (\text{K km s}^{-1})^{-1}$ including He; Bolatto et al. 2013) and can be regarded as canonical in star-forming galaxies of about solar metallicity, the widely used HCN conversion factor of $\alpha_{\text{HCN}} = 10 M_{\odot} \text{pc}^{-2} (\text{K km s}^{-1})^{-1}$ was derived by Gao & Solomon (2004) assuming virialized (self-gravitating) optically thick dense gas cores with a gas density of $n \sim 3 \times 10^4 \text{ cm}^{-3}$ and constant brightness temperatures of 35 K. Wu et al. (2010) found a twice higher HCN conversion factor of $\alpha_{\text{HCN}} \sim 20 M_{\odot} \text{pc}^{-2} (\text{K km s}^{-1})^{-1}$.

The Vollmer & Beckert (2003) theory of clumpy gas disks provides analytic expressions for large-scale and small-scale properties of galactic gas disks. The large-scale properties considered are the gas surface density, volume density, disk height, turbulent driving length scale, velocity dispersion, gas viscosity, volume filling factor, and molecular fraction. Small-scale properties are the mass, size, density, turbulent crossing time, free-fall time, and molecular formation timescale of the most massive self-gravitating gas clouds. These quantities depend on the stellar surface density, angular velocity, disk radius R , and three free parameters, which are the Toomre parameter Q of the gas, the mass accretion rate \dot{M} , and the ratio δ between the driving length scale of turbulence and the cloud size. Vollmer & Leroy (2011) determined these free parameters using three independent measurements of the radial profiles of the atomic gas (HI), molecular gas (CO), and SFR (far-ultraviolet + 24 μm) for a sample of 18 mostly spiral galaxies from Leroy et al. (2008). The fits of radial profiles were acceptable, with reduced χ^2 minimizations (defined as the normalized sum of the squared differences divided by the observational uncertainties) generally smaller than 2 for all galaxies except NGC 5194 (M 51):

$$\chi_{\text{tot}}^2 = \sum_i \chi_i^2 = \sum_i \frac{(O_i - M_i)^2}{\sigma_i^2}, \quad (1)$$

where O_i corresponds to a single observational measurement, M_i is the model value, and σ_i is the observational error. It was found that the model star-formation efficiency is very sensitive to the description of the local pressure equilibrium in the disk midplane. The model-derived free-fall timescales of self-gravitating clouds were in good agreement with expectations based on observations. Only low-mass galaxies ($M_* < 10^{10} M_{\odot}$) can balance the gas loss due to star formation with radial gas inflow within the galactic disk. Krumholz & Burkhardt (2016) elaborated a similar model that included radial gas transport and stellar feedback. They concluded that, in spiral galaxies at low redshift, turbulence is driven by star formation.

Vollmer et al. (2017) significantly extended the Vollmer & Leroy (2011) model by introducing ISM scaling relations. The extended model simultaneously calculates the total gas mass, HI/H₂ mass ratio, gas velocity dispersion, infrared luminosity, infrared spectral energy distribution, CO spectral line energy distribution (SLED), HCN(1–0) and HCO⁺(1–0) emission of a galaxy given its size, integrated SFR, stellar mass radial profile, rotation curve, and Toomre Q parameter. The model was applied to the integrated properties of local spiral galaxies, ultra-luminous infrared galaxies (ULIRGs), high- z star-forming galaxies, and submillimeter galaxies. The model reproduced the observed CO luminosities and SLEDs of all sample galaxies within the model uncertainties (~ 0.3 dex). The model CO and HCN conversion factors had uncertainties of a factor of two. Both the HCN and HCO⁺ emission trace the

dense molecular gas to a factor of approximately two for the local spiral galaxies, ULIRGs, and submillimeter galaxies.

In the present article we use the Vollmer et al. (2017) model to calculate the infrared, HI, CO, HCN, and HCO⁺ emission radial profiles and compare them to observations of 17 local spiral galaxies from Leroy et al. (2008). Unlike in Vollmer & Leroy (2011), the assumption of a radially constant mass accretion rate \dot{M} was dropped and the Toomre parameter Q was self-consistently determined at each galactic radius. The new model allowed us to compare the SFR based on the far-ultraviolet (FUV) and 24 μm emission to the infrared radial profile and to calculate the radial variations in (i) the CO and HCN conversion factors and (ii) the star-formation efficiency.

The structure of this article is the following: The observations from the literature are described in Sect. 2. Our model of a turbulent clumpy accretion disk is outlined, the search for the best-fit model is explained, and the detected model degeneracies are presented in Sect. 3. The results are given in Sect. 4, followed by the discussion (Sect. 5) and our conclusions (Sect. 6).

2. Observations

In this section we describe the observational data, which are used for the comparison with the quantities obtained from our models. All multiwavelength data were convolved to the same spatial resolution and were converted to the same unit (i.e., K km s⁻¹) for the atomic and molecular line data and MJy sr⁻¹ for the infrared data.

2.1. Atomic hydrogen HI

The 21 cm HI radial profiles used in this paper were taken from the “HI Nearby Galaxy Survey” (THINGS, CDS VizieR table J/AJ/136/2782) presented in Walter et al. (2008). The spatial resolution is about 7'' with a spectral resolution of 5 km s⁻¹ per channel. With an average of 7 h of observations on source, a typical rms noise of 0.4 mJy beam⁻¹ (which corresponds to 5 K) was reached.

2.2. Carbon monoxide CO(2–1)

The “HERA CO Line Extragalactic Survey” (HERACLES) is presented in detail in Leroy et al. (2009). The data were collected using the HETerodyne Receiver Array (HERA) multi-pixel receiver from the single dish 30 m telescope of the “Institut de Radioastronomie Millimétrique” (IRAM, Pico Veleta, Spain). HERA was tuned near 230 GHz to observe the CO(2–1) rotational transition. On-the-flight (OTF) maps were produced, giving a spatial resolution of 13'', a spectral resolution of 2.6 km s⁻¹ and a rms noise about 20 mK. The HERACLES survey focused on targets that were part of the THINGS galaxy sample. We used the radial profiles presented in Leroy et al. (2008) (CDS VizieR table J/AJ/136/2782) except for NGC 3627, NGC 5194, and NGC 7793, for which we used the CO(2–1) profile presented in den Brok et al. (2021) derived from the “Physics at High Angular resolution in Nearby Galaxies” (PHANGS) data survey (Leroy et al. 2021).

2.3. Carbon monoxide CO(1–0), hydrogen cyanide HCN(1–0), and formylion HCO⁺(1–0)

The CO(1–0), HCN(1–0), and HCO⁺(1–0) radial profiles were taken from the “EMIR Multiline Probe of the ISM Regulating

Table 1. Galaxy properties.

Galaxy ⁽¹⁾	Type	RA J2000	Dec J2000	R_{25} (kpc)	D (Mpc)	i (deg)	PA (deg)	$\log M_{\star}$ ($10^8 M_{\odot}$)	R_d (kpc)	v_{flat} (km s^{-1})	l_{flat} (kpc)
NGC 628	Sc	01 36 41.772	+15 47 0.46	10.4	7.3	7	20	10.1	2.3	217	0.8
NGC 3184	SBc	10 18 16.985	+41 25 27.77	12.0	11.1	16	179	10.3	2.4	210	2.8
NGC 3627	SBb	11 20 15.026	+12 59 28.64	13.8	9.3	62	173	10.6	2.8	192	1.2
NGC 5055	Sbc	13 15 49.274	+42 01 45.73	17.3	10.1	59	102	10.8	3.2	192	0.7
NGC 5194	SBc	13 29 52.698	+47 11 42.93	9.0	8.0	20	172	10.6	2.8	219	0.8
NGC 6946	SBc	20 34 52.332	+60 09 13.24	9.9	5.9	33	243	10.5	2.5	186	1.4
NGC 2841	Sb	09 22 02.655	+50 58 35.32	14.2	14.1	74	153	10.8	4.0	302	0.6
NGC 3198	SBc	10 19 54.990	+45 32 58.88	13.0	13.8	72	215	10.1	3.2	150	2.8
NGC 3351	SBb	10 43 57.733	+11 42 13.00	10.6	10.1	41	192	10.4	2.2	196	0.7
NGC 3521	SBbc	11 05 48.568	-00 02 9.23	13.0	10.7	73	340	10.7	2.9	227	1.4
NGC 4736	Sab	12 50 53.148	+41 07 12.55	5.3	4.7	41	296	10.3	1.1	156	0.2
NGC 7331	SAb	22 37 04.102	+34 24 57.31	19.5	14.7	76	168	10.9	3.3	244	1.3
NGC 925	SBcd	02 27 16.913	+33 34 43.97	14.3	9.2	66	287	9.9	4.1	136	6.5
NGC 2403	SBc	07 36 51.396	+65 36 09.17	7.4	3.2	63	124	9.7	1.6	134	1.7
NGC 2976	Sc	09 47 15.458	+67 54 58.97	3.8	3.6	65	335	9.1	0.9	92	1.2
NGC 4214	Irr.	12 15 39.174	+36 19 36.80	2.9	2.9	44	65	8.8	0.7	57	0.9
NGC 7793	Scd	23 57 49.754	-32 35 27.70	6.0	3.9	50	290	9.5	1.3	115	1.5

Notes. ⁽¹⁾In order of appearance: massive galaxies ($\log M_{\star} > 10$) with EMPIRE data, massive galaxies without EMPIRE data, low-mass galaxies ($M_{\star} < 10^{10} M_{\odot}$) without EMPIRE data.

Galaxy Evolution” (EMPIRE) survey (Jiménez-Donaire et al. 2019; CDS VizieR table J/ApJ/880/127). The EMPIRE observations were carried out at the IRAM 30 m telescope using the dual-polarization “Eight MIXer Receiver” (EMIR) receiver. The spectral resolution is about 4 km s^{-1} per channel, with an rms noise about 2–3 mK for the dense gas ($n_{\text{H}_2} \sim 10^4 \text{ cm}^{-3}$) HCN and HCO⁺ observations. Spatial resolutions are 26”, 33”, and 33” for the CO(1–0), HCN(1–0) and HCO⁺(1–0) data, respectively. In contrast to the other data presented in this paper for which radial profiles with 10” wide rings were extracted from the moment-0 maps, Jiménez-Donaire et al. (2019) used a stacking method to recover the emission from the regions with low signal-to-noise ratio.

2.4. Star-formation rate

Star-formation rate profiles were computed by Leroy et al. (2009) using the FUV “Galaxy Evolution Explorer” (GALEX) data (Gil de Paz et al. 2007) with the 24 μm infrared data from the “Spitzer Infrared Nearby Galaxies Survey” (SINGS) (Kennicutt et al. 2003). Their spatial resolutions are 6” and 5”, respectively. The following linear combination was used to compute the SFR:

$$\dot{\Sigma}_{\star} = (8.1 \times 10^{-2} I_{\text{FUV}} + 3.2 \times 10^{-3} I_{24\mu\text{m}}) \times \cos i, \quad (2)$$

where I_{FUV} and $I_{24\mu\text{m}}$ are the ultraviolet and infrared fluxes in MJy sr^{-1} and i is the inclination angle of the galaxy. The SFR surface density $\dot{\Sigma}_{\star}$ has units of $M_{\odot} \text{ kpc}^{-2} \text{ yr}^{-1}$.

2.5. Far-infrared data profiles and temperature maps

We worked with four far-infrared bands from the “Photodetector Array Camera and Spectrometer” (PACS: 100 μm) and “Spectral and Photometric Imaging Receiver” (SPIRE: 250, 350, and 500 μm) instrument on the *Herschel* satellite. Their spatial resolutions are 7, 18, 25, and 35”, respectively. The far-infrared

profiles were taken from Hunt et al. (2015) (CDS VizieR table J/A+A/576/A33).

2.6. Sample of galaxies

Our sample comprises 17 star-forming galaxies that the surveys presented in the previous section have in common. This galaxy sample is composed of five low-mass ($M_{\star} < 10^{10} M_{\odot}$) galaxies and 12 nearby large spiral galaxies. The general properties of these galaxies are presented in Table 1. The rotation curves of the model galaxies were computed by Leroy et al. (2008) using the following expression (Boissier et al. 2003):

$$v_{\text{rot}} = v_{\text{flat}} \left(1 - \exp\left(-\frac{R}{l_{\text{flat}}}\right) \right), \quad (3)$$

where v_{flat} and l_{flat} were determined by performing a polynomial fit on the observational curves. The common spatial resolution is 400 pc for the low-mass galaxies and 800 pc for the large spiral galaxies.

3. Model fitting

In this section we describe our analytical model and introduce its free parameters. The comparison with the data was performed via a reduced χ^2 minimization (Eq. (1)). We investigated the degeneracies between the free model parameters.

3.1. The model

Our model is a slightly modified version of the analytical model presented by Vollmer et al. (2017), itself derived from previous versions presented in Vollmer & Beckert (2003) and Vollmer & Leroy (2011). A detailed description of the model is given in Appendix A. The analytical model describes galaxies as star-forming, clumpy, and turbulent accretion disks. The ISM is considered as a turbulent multiphase gas. This gas is assumed to

Table 2. Model free parameters.

Q	–	Toomre parameter, gravitational stability of gas clouds (Eq. (A.18))
\dot{M}	$M_{\odot} \text{ yr}^{-1}$	Radial mass accretion rate within the disk (Eq. (A.7))
δ	–	Scaling factor between the driving length scale and the size of self-gravitating structures (Eq. (A.12))
ξ	$\text{pc}^2 \text{ yr}^{-1}$	Constant relating supernovae energy input to star formation (Eq. (A.5))
α_0	$\text{yr } M_{\odot} \text{ pc}^{-3}$	Constant of molecule formation timescale, inverse of the effective stellar yield (Eq. (A.17))
γ	–	Scaling factor of the vertical stellar velocity dispersion (Eq. (A.1))

be in vertical hydrostatic equilibrium, with the mid-plane pressure balancing the weight of the gaseous and the stellar disk (Elmegreen 1989; Eq. (A.1)). The model gas is described as “clumpy”, so the local density can be enhanced relative to the average density of the disk. The local free-fall time of an individual gas clump is taken as the governing timescale for star formation. The SFR is used to calculate the rate of energy injection by supernova (SN) explosions. This rate is related to the turbulent velocity dispersion and the driving scale of turbulence. These quantities in turn provide estimates of the “clumpiness” of gas in the disk (the contrast between local and average density) and the rate at which viscosity moves matter inward. The model relies on several empirical calibrations: the relation between the stellar velocity dispersion and the stellar disk scale length (Eq. (A.2)), the relationship between the SFR and the energy injected into the ISM by SNe (Eq. (A.5)), and the characteristic time of H_2 formation, which is related to the gas metallicity Z (Eqs. (A.15)–(A.17)) and the gas density. The equilibrium between turbulence and star formation depends on three local timescales: the turbulent crossing time t'_{turb} , the molecule formation timescale t'_{mol} , and the local free-fall timescale t'_{ff} of a cloud. In addition, photodissociation of molecules is taken into account.

The model has a large-scale and a small-scale part. The large-scale part gives the surface density, turbulent velocity, disk height, and gas viscosity. The small-scale part begins at densities where gas clouds become self-gravitating ($t'_{\text{ff}} = t'_{\text{turb}}$). The non-self-gravitating and self-gravitating clouds obey different scaling relations, which are set by observations (Appendix A.2.2). For each gas density, the mass fraction is characterized by a log-normal probability distribution function and the Mach number (Padoan et al. 1997). The temperatures of the gas clouds are calculated via the equilibrium between turbulent mechanical and cosmic ray heating and gas cooling via CO and H_2 line emission (Appendix A.2.4). The abundances of the different molecules are determined using the gas-grain code Nautilus (Hersant et al. 2009). The dust temperatures are calculated via the equilibrium between heating by the interstellar UV and optical radiation field and cooling via infrared emission.

The model simultaneously calculates (i) for the large-scale part: the total gas profile, the gas velocity dispersion, the SFR, and the volume filling factor; (ii) for the small-scale part: the molecular fraction, infrared profiles and spectral energy distribution, and molecular line profiles of different molecules, such as CO(1–0), CO(2–1), HCN(1–0), and $\text{HCO}^+(1–0)$. The molecular line emission calculation is based on a two-level approximation and the escape probability formalism. This approximation greatly decreases the computation time. An important ingredient for the line emission is the area-filling factor of the gas clouds, which is a result of the small-scale part of the analytic disk model. The new code was modified to enable an independent treatment of each of the radial data points. The input of a given

radial profile of the Toomre parameter Q and the assumption of a constant mass accretion rate \dot{M} , which were required to produce the molecular line profiles in Vollmer & Leroy (2011), are no longer necessary. The radial profiles of the stellar surface density and the rotation curve (both taken from Leroy et al. 2008) are used as inputs of the model. The model yields the radial profiles of \dot{M} and Q for a given δ , which best fit the available observations (SFR, HI, CO(1–0), CO(2–1)). With these profiles the physical properties of the ISM such as the molecular surface density, the gas velocity dispersion, or the CO and HCN conversion factors can be calculated.

3.2. Model parameters

The model inputs are the rotation curve and the stellar surface density profile. The model contains three main free parameters: (i) the Toomre parameter Q of the gas, which indicates the gravitational stability ($Q = 1$) of a gas cloud, (ii) the mass accretion rate \dot{M} , which sets the gas turbulent velocity, and (iii) δ , the ratio between the turbulent driving length scale and the size of the largest self-gravitating clouds. At a given disk radius R the model yields the SFR per unit area and the HI and molecular line emission for a given set of Q , \dot{M} , and δ .

Unlike Vollmer et al. (2017), we decided to vary other parameters that were previously constant. These parameters present large uncertainties and were identified as having a significant impact on the results. The first parameter, ξ , relates the SFR to the energy injected into the ISM by SNe (Eq. (A.5)). The second parameter, α_0 , relates the characteristic time to form H_2 out of H to the local free-fall time (Eq. (A.16)). This parameter depends on to the gas metallicity of the galaxy (Eq. (A.17)). The last parameter, γ , controls the vertical component of the stellar velocity dispersion and thus the gravitational restoring force of the stellar disk (Eq. (A.1)). This is motivated by a possible heating of the stellar disk following a gravitational interaction. Because of the large computation time of the models we limited ourselves to four values for δ , five values of ξ and α_0 , and three values for γ : $\delta = [3, 5, 7, 9]$, $\xi = (0.25, 0.5, 1, 2, 4) \times 4.6 \times 10^{-8} (\text{pc yr}^{-1})^2$, $\alpha_0 = (0.25, 0.5, 1, 2, 4) \times 2.2 \times 10^7 \text{ yr } M_{\odot} \text{ pc}^{-3}$, and $\gamma = 0.5, 1, 2$. We individually varied each of these parameters, with default values corresponding to unity for ξ , α_0 , and γ . Because of the large computation times we did not consider combinations of these variations. All these free parameters are summarized in Table 2.

The infrared emission also depends on the gas-to-dust ratio (GDR) and exponent β of the wavelength dependence of the dust absorption coefficient. For the search of $[Q(R), \dot{M}(R), \delta, \alpha_0, \xi, \gamma]$ we used $\text{GDR} = 100$ and $\beta = 1.5$. As a last step, we kept best-fit $[Q(R), \dot{M}(R), \delta, \alpha_0, \xi, \gamma]$ constant and varied GDR and β to determine their values by searching for the best fit of the observed infrared profiles.

Finally, different values of the cosmic ray ionization rate were applied to the best-fit models. The value that was assumed

in previous versions of the model was $\zeta_{\text{CR}} = 10^{-17} \text{ s}^{-1}$, which corresponds to the standard value for GMCs (Dalgarno 2006). Additionally, we used $\zeta_{\text{CR}} = 3 \times 10^{-18} \text{ s}^{-1}$ and 10^{-18} s^{-1} .

3.3. Determination of the best-fit model using χ^2 minimizations

For each set of $[\delta, \alpha_0, \xi, \gamma]$ we performed a χ^2 minimization at each radius independently to find the best-fit Q and \dot{M} . The contributions from the different radial profiles (SFR, HI, CO(1–0), and CO(2–1)) were summed to obtain a total χ^2 :

$$\chi_{\text{tot}}^2 = \sum_i \frac{(O_i - M_i)^2}{\sigma_i^2} = \chi_{\text{HI}}^2 + \chi_{\text{SFR}}^2 + \chi_{\text{CO}}^2, \quad (4)$$

where O_i and M_i are the observed and model data points and σ_i the uncertainties of the observations. For the majority of galaxies, we set $\chi_{\text{CO}}^2 = \chi_{\text{CO(2-1)}}^2$ with the CO(2–1) data from the HERACLES survey. We increased the uncertainties of the PHANGS radial profiles of NGC 3627 and NGC 5194 to those typically found for the HERACLES profiles. Without this increase in the uncertainties, the PHANGS profiles would dominate the total χ^2 . For galaxies observed by the EMPIRE survey, we set $\chi_{\text{CO}}^2 = \chi_{\text{CO(2-1)}}^2/2 + \chi_{\text{CO(1-0)}}^2/2$ to take the CO(1–0) emission in the determination of the best-fit model into account. It turned out that the inclusion of the CO(1–0) emission led to somewhat different fitting results. For consistency between the results of all galaxies, we also performed χ^2 minimizations including only CO(2–1) emission for the galaxies observed by EMPIRE. The comparison of the line brightness temperatures obtained with our model and those obtained with RADEX (van der Tak et al. 2007) showed good agreement (within ~50%) for the CO lines but much less good agreement for the HCN and HCO⁺ lines (up to a factor of two to three). Therefore, χ_{HCN}^2 and $\chi_{\text{HCO}^+}^2$ based on the line brightness temperatures obtained with our model were calculated but not included in the χ_{tot}^2 calculation. We worked within a parameter grid of twenty values of Toomre parameter $Q = [1:10]$ and twenty values of the accretion rate $\dot{M} = [10^{-3}:1]$ for each radius. These intervals were chosen according to the results of Vollmer & Leroy (2011). We did not consider gas disks that are unstable to fragmentation ($Q < 1$). The outer radius of the model is set by the detection limit of the CO observations.

The best-fit models for each galaxy are listed in Table 3 for galaxies with EMPIRE data and Table 4 for the rest of the sample. The corresponding radial profiles of Q and \dot{M} are shown in Figs. 2 and B.1–B.16 and discussed in Sect. 4.3.1. The models presented in the two tables correspond to the models that present a $\chi_{\text{tot}}^2 \in [\chi_{\text{tot,min}}^2, \chi_{\text{tot,min}}^2 + 0.1\chi_{\text{tot,min}}^2]$. In Table 3, the values between parentheses correspond to the $\chi_{\text{CO(1-0)}}^2$ that are not included in the χ_{tot}^2 calculations.

Because the determination of the best-fit basic models were very time consuming, we decided to vary GDR, β , and ζ_{CR} separately: a second, independent χ^2 minimization was performed on the basic model to determine the value of β and GDR to fit the 100, 250, and 500 μm infrared radial profiles. This minimization generally led to values of GDR and β , which are higher than the default values, decreasing the dust optical depth and infrared emission. The corresponding change of the molecular line emission due to a lower background temperature is less than one percent. The values of β and GDR for each galaxy are presented in Table 5. We found a mean $\beta = 2$ and a mean GDR ~250, which is more than twice the value found by Sandstrom et al. (2013). The difference probably lies in the dust illumination of our model

and that of Draine & Li (2007). In our model the radiation field is proportional to the SFR, which is constant at a given galactic radius. In the Draine & Li model the dust mass is exposed to a power-law distribution of starlight intensities between U_{min} and U_{max} with $dM/dU \propto U^{-1}$. This leads to higher dust temperatures and lower dust masses in our model compared to those derived by the Draine & Li model.

A third χ^2 minimization was finally performed on the basic model to find which cosmic ray ionization rate reproduces the HCN and HCO⁺ radial profiles best, with three different values of $\zeta_{\text{CR}} = [10^{-18}, 3 \times 10^{-18}, 10^{-17}] \text{ s}^{-1}$. These values correspond to the observed range of the cosmic ray ionization rate (see Sect. 4.3.2). The best-fit values of ζ_{CR} are presented in Table 6.

3.4. Degeneracies between free parameters

The study of the models revealed several degeneracies between the input parameters. Most of the results stated here have been discussed in our previous work (Lizée et al. 2021). First, the exact value of δ never appears to be important for the determination of the best-fit model. A constant value of $\delta = 5$ as used in Vollmer & Leroy (2011) and Vollmer et al. (2017) is thus justified. Second, increasing the value of ξ by a factor of two leads to similar model χ^2 , Q , and \dot{M} as dividing the value of α_0 by a factor of two. Third, increasing the value of α_0 by a factor of two leads to similar model χ^2 , Q , and \dot{M} as multiplying the stellar velocity dispersion by a factor of two.

The first degeneracy is illustrated in Tables 3 and 4. In the case of NGC 5055, NGC 3351, NGC 3521, NGC 4736, NGC 7331, NGC 2403, and NGC 4214 although either a division of α_0 by two or a multiplication of ξ by two is favored by most best-fit models, the second degeneracy mentioned above becomes evident when inspecting the ten models with the lowest χ^2 for these galaxies. In addition, the best-fit models of NGC 7793 needed a decreased metallicity ($2 \times \alpha_0$) with respect to the leaky box model (Eq. (A.16)). The lower metallicities are consistent with observations (Moustakas et al. 2010; Stanghellini et al. 2015) and can be understood as a consequence of external accretion of metal-poor gas.

The division of α_0 by two is equivalent to a doubling of the metallicity, which is in conflict with existing metallicity measurements (e.g., Moustakas et al. 2010; Kreckel et al. 2019; Berg et al. 2020). A higher value of ξ can be justified in the following way: Thornton et al. (1998) have shown by modeling SN explosions in different environments that the kinetic energy of the remnants is about ten percent of the total SN energy irrespective of the density and metallicity of the ambient medium. The SN energy input into the ISM is $E_{\text{SN}}^{\text{kin}} \sim 10^{50}$ ergs. The integrated number of type II SNe in the Galaxy is taken to be $\dot{N}_{\text{SN}} \sim 1/60 \text{ yr}^{-1}$ (Rozwadowska et al. 2021). The Galactic SFR is taken to be $M_* = 1.6 M_{\odot} \text{ yr}^{-1}$ (Licquia & Newman 2015). With a kinetic to total SN energy fraction of 16% one obtains $\xi = 9.2 \times 10^{-8} (\text{pc yr}^{-1})^2$, a factor two higher than the value used by Vollmer & Beckert (2003) and Vollmer & Leroy (2011). The improved large-scale model presented in Appendix A is equivalent to the model used by Vollmer & Leroy (2011) provided that $\xi = 9.2 \times 10^{-8} (\text{pc yr}^{-1})^2$.

4. Results

Unlike the model presented in Vollmer et al. (2017), the current model is able to produce radial profiles of the infrared fluxes and molecular line emission. In this way we can directly compare the observational radial profiles to our models. Typical uncertainties of the derived \dot{M} and Q are 0.3 dex and 0.2 dex, respectively.

Table 3. Best-fit models of the EMPIRE galaxies.

Galaxy	δ	ξ	α_0	γ	χ^2_{HI}	χ^2_{SFR}	$\chi^2_{\text{CO}(2-1)}$	$\chi^2_{\text{CO}(1-0)}$	χ^2_{tot}
NGC 628	5	–	0.5×	–	32	22	79	401	294
	3	–	0.5×	–	31	19	62	468	315
	9	2×	–	–	26	18	65	1074	614
	5	–	–	0.5×	6	10	7	(2285)	23
	7	–	–	0.5×	6	5	12	(2147)	23
	5	–	–	–	4	8	13	(2714)	24
	9	–	–	–	5	6	12	(2132)	24
	9	–	0.5×	–	34	108	27	107	209
NGC 3184	9	2×	–	–	24	49	30	254	214
	5	2×	–	–	14	74	26	234	218
	7	–	0.5×	–	27	129	29	105	224
	7	2×	–	–	52	57	31	200	224
	5	2×	–	–	5	7	9	(1261)	20
	9	2×	–	–	5	7	8	(1258)	20
	3	2×	–	–	12	5	9	(1738)	26
	9	–	0.5×	–	209	225	31	1208	1053
NGC 3627	9	–	0.5×	–	235	275	31	1117	1083
	7	–	0.5×	–	273	323	30	1059	1141
	3	–	0.5×	–	3	1	40	(12 612)	44
	9	–	0.5×	–	2	4	39	(33 875)	44
	5	–	0.5×	–	2	2	40	(27 516)	45
	3	2×	–	–	42	50	211	353	374
NGC 5055	5	2×	–	–	25	75	220	368	394
	7	2×	–	–	39	59	202	410	404
	7	2×	–	–	41	45	91	(1450)	177
	9	2×	–	–	36	52	91	(1443)	179
	3	2×	–	–	42	39	99	(1206)	181
	5	2×	–	–	35	59	89	(1756)	182
	3	2×	–	–	90	73	29	259	307
	5	–	0.5×	–	143	113	27	107	322
NGC 5194	3	2×	–	–	90	73	29	259	307
	9	–	0.5×	–	10	4	16	(20 647)	30
	3	2×	–	–	11	8	16	(24 194)	35
	7	–	0.5×	–	12	5	19	(29 896)	36
	9	–	0.5×	–	182	1355	97	1033	2102
	7	–	0.5×	–	281	1523	94	893	2297
NGC 6946	5	–	0.5×	–	820	1572	97	438	2659
	7	–	0.5×	–	7	7	25	(224 629)	40
	9	–	0.5×	–	6	10	26	(209 394)	42
	5	–	0.5×	–	7	10	26	(248 890)	43

Notes. Values between parentheses are not included into the total χ^2 calculation. All the parameters are described in Table 2. The best models are for most galaxies those with $\alpha_0/2$ or $\xi \times 2$ (see Sect. 3.4).

This translates into uncertainties of 2–3 km s^{−1} for the turbulent velocity dispersion of the ISM and 0.1–0.2 dex for the CO and HCN conversion factors.

In this section we focus on the results of NGC 6946 as an example; the results for the other galaxies are available in Appendix B. The best-fit models presented in Table 3 are computed using our molecular emission recipe (Appendix A.2.5) to fix the values of δ , ξ , α_0 , and γ , and to produce radial profiles of Q and \dot{M} . We then recalculated the molecular line emission of our best-fit models using RADEX instead of our molecular emission recipe to produce the final radial profiles. Since the use of RADEX is time consuming, we could not use it for the Q – \dot{M} grid calculations. As a consistency check we used RADEX for the Q – \dot{M} grid calculations for NGC 6946 with the best-fit values

of δ , ξ , α_0 , and γ given in Table 3. The resulting RADEX best-fit model yields a better fit to the CO(1–0) and CO(2–1) line emission, a less good fit to the SFR in the inner disk, a lower Q parameter ($Q = 1$), a comparable \dot{M} , and a somewhat lower gas velocity dispersion compared to the model where RADEX was used a posteriori. Since these changes are within the uncertainties of the model, we are confident that our derived model parameters are meaningful.

4.1. NGC 6946

The best-fit models for NGC 6946 obtained with our molecular emission calculation recipe are presented in Figs. 1c and d. The best-fit models using RADEX for the molecular line emission

Table 4. Best-fit models of the THINGS galaxies without EMPIRE data.

Galaxy	δ	ξ	α_0	γ	χ^2_{HI}	χ^2_{SFR}	$\chi^2_{\text{CO}(2-1)}$	χ^2_{tot}
NGC 2841	7	–	–	0.5×	5	2	2	9
	3	–	0.5×	–	3	3	4	10
	5	–	0.5×	–	2	4	5	11
NGC 3198	9	0.5×	–	–	2	8	16	26
	7	0.5×	–	–	4	8	14	26
	9	–	–	–	8	9	10	27
NGC 3351	5	0.5×	–	–	13	45	39	96
	9	0.5×	–	–	22	27	48	97
	7	0.5×	–	–	29	43	36	108
NGC 3521	9	2×	–	–	83	135	52	270
	7	2×	–	–	97	111	67	275
	5	2×	–	–	108	124	69	300
NGC 4736	3	–	2×	–	4	8	6	18
	5	–	2×	–	5	6	10	21
	9	–	2×	–	2	9	12	24
NGC 7331	9	–	–	2×	31	11	23	65
	5	–	–	2×	32	16	34	81
	7	–	–	2×	37	19	24	79
NGC 925	3	–	0.5×	–	59	192	216	468
	5	–	0.5×	–	56	167	307	531
	7	–	0.5×	–	69	135	358	562
NGC 2403	3	2×	–	–	31	29	28	88
	5	2×	–	–	29	39	25	93
	7	2×	–	–	34	36	32	102
NGC 2976	7	–	0.5×	–	108	86	89	283
	9	–	0.5×	–	131	90	54	275
	3	–	0.5×	–	116	85	90	291
	5	–	0.5×	–	120	83	80	283
NGC 4214	3	2×	–	–	1	14	2	17
	3	–	–	–	2	13	3	18
	5	2×	–	–	1	13	8	22
NGC 7793	5	–	2×	–	37	10	68	115
	7	–	2×	–	38	11	70	118
	9	–	2×	–	42	13	64	119
	3	–	2×	–	41	13	76	130

Notes. All the parameters are described in Table 2. The best models are for most galaxies those with $\alpha_0/2$ or $\xi \times 2$ (see Sect. 3.4).

with and without CO(1–0) in the χ^2 minimization are compared in Figs. 1a and b, respectively. The total χ^2_{tot} without $\chi^2_{\text{CO}(1-0)}$ is 40, much lower than the one obtained when $\chi^2_{\text{CO}(1-0)}$ is included in χ^2_{tot} ($\chi^2_{\text{tot}} = 2102$; see Table 3). The very small errors given for the CO(1–0) EMPIRE data obtained via stacking tend to favor the CO(1–0) profile over the other quantities and lead to larger χ^2_{tot} values. The χ^2_{HI} with $\chi^2_{\text{CO}(1-0)}$ in χ^2_{tot} is 182 compared to $\chi^2_{\text{HI}} = 7$ without $\chi^2_{\text{CO}(1-0)}$ in χ^2_{tot} . The difference is mainly due to the central part of the galaxy ($R \lesssim 2$ kpc) that is not well reproduced by the model. Likewise, $\chi^2_{\text{SFR}} = 7$ is much lower in the model without $\chi^2_{\text{CO}(1-0)}$ than in the model with $\chi^2_{\text{CO}(1-0)}$ in χ^2_{tot} ($\chi^2_{\text{SFR}} = 1355$) because of the poor fit within the central 2 kpc. Both HI and SFR radial profiles are reproduced within the error bars from 2 kpc to the edge of the disk with or without $\chi^2_{\text{CO}(1-0)}$ in χ^2_{tot} . The best-fits of the CO(2–1) radial profiles remain fairly comparable with or without $\chi^2_{\text{CO}(1-0)}$ in χ^2_{tot} ($\chi^2_{\text{CO}(2-1)} = 97$ instead of 25).

The comparison of the model and observed infrared profiles shows that without CO(1–0) the model is much better at repro-

ducing the radial profiles in the central part of the galaxy. Beyond 2 kpc, the 250 and 500 μm profiles are also well reproduced without CO(1–0). The profile of the 100 μm emission, on the other hand, is not well reproduced by the model with or without $\chi^2_{\text{CO}(1-0)}$ in χ^2_{tot} . The radial profiles of the model 250 and 500 μm profiles are somewhat steeper than the observed profiles in the model including $\chi^2_{\text{CO}(1-0)}$ in the χ^2 minimization. The free parameters β and GDR, do not modify the slope of the far-infrared profiles.

The main improvement provided by the use of the CO(1–0) is the fit of the HCN(1–0) and HCO⁺(1–0) profiles with a significantly lower $\chi^2_{\text{dense}} = \chi^2_{\text{HCN}} + \chi^2_{\text{HCO}^+}$, 5524 instead of 20 430 (see Table 6). However, χ^2_{HI} and χ^2_{SFR} increase by a factor of about 25 and 200, respectively, when $\chi^2_{\text{CO}(1-0)}$ is included in χ^2_{tot} . The model is therefore not able to reproduce the infrared (and thus the SFR) and the dense molecular line emission simultaneously in the central part of the galaxy.

The physical parameters Q and \dot{M} associated with the best-fit models are presented in Figs. 2a and b. The Toomre parameter Q_{gas} increases from around unity near the galaxy center to

Table 5. Infrared profile parameters.

Galaxy	$\beta^{(a)}$	GDR ^(a)
NGC 628	2	300
	2	300
NGC 3184	2	500
	2	400
NGC 3627	2	300
	2	200
NGC 5055	2	100
	2	200
NGC 5194	1.5	400
	1.5	200
NGC 6946	2.5	200
	2.5	200
NGC 2841	2	200
NGC 3198	2.5	100
NGC 3351	2	500
NGC 3521	2	200
NGC 4736	2	600
NGC 7331	2	200
NGC 925	2.5	100
NGC 2403	1.5	200
NGC 2976	2	100
NGC 4214	0.5	500
NGC 7793	2	100
\bar{x}	1.9 ± 0.5	294 ± 201

Notes. ^(a)Upper line: with $\chi_{\text{CO}(1-0)}^2$ in the χ^2 calculations. Lower line: without $\chi_{\text{CO}(1-0)}^2$. β : exponent of the wavelength dependence of the dust absorption coefficient. GDR: gas-to-dust ratio.

$Q_{\text{gas}} = 2-3$ toward the outer disk for both χ^2 calculations. The accretion rate \dot{M} increases monotonically from 1 to 6 kpc by a factor of ~ 10 from the center to the edge of the disk. The combination of these two parameters leads to a total velocity dispersion $\sigma_{\text{disp}} = \sqrt{v_{\text{turb}}^2 + c_s^2}$, which increases slightly from the canonical value of 10 km s^{-1} at 1 kpc to more than 13 km s^{-1} at 6 kpc (see Fig. 2, panels c and d). The model without $\chi_{\text{CO}(1-0)}^2$ in χ_{tot}^2 shows velocity dispersions higher than 15 km s^{-1} at radii larger than 6 kpc.

We compared the model velocity dispersion profiles to the observed profiles based on THINGS and HERACLES data presented by Caldú-Primo et al. (2013). Ianjamasimanana et al. (2015) found a constant velocity dispersion around the canonical value of 10 km s^{-1} up to R_{25} in NGC 6946. The model velocity dispersion profile including $\chi_{\text{CO}(1-0)}^2$ in the χ^2 minimization is consistent with the observed profiles Figs. 2c and d. The model without $\chi_{\text{CO}(1-0)}^2$ in χ^2 significantly overestimates the velocity dispersion for $R > 6 \text{ kpc}$. We conclude that this increase in the model velocity dispersion on the order of 8 km s^{-1} is not physical. This issue is further discussed in Sect. 4.3.1.

The profiles of the gas depletion and viscous timescales of the best-fit models are presented in Figs. 2e and f. The viscous timescale is defined as

$$t_{\text{vis}}(R) = \frac{R^2}{\sqrt{3}v_{\text{turb}}l_{\text{driv}}}, \quad (5)$$

where l_{driv} is the turbulent driving length. The gas depletion time corresponds to the time that a galaxy takes to locally convert

its gas into stars. The timescale of radial gas transport is given by the viscous timescale. By comparing these two times, it is possible to estimate whether or not a galaxy can maintain its star formation via radial gas transport without external accretion. For the best-fit models with and without $\chi_{\text{CO}(1-0)}^2$ in the χ_{tot}^2 calculations the gas depletion time is almost constant beyond 2 kpc with $t_{\text{dep}} \sim 1-2 \text{ Gyr}$, which is consistent with the average value for spiral galaxies (Bigiel et al. 2008; Leroy et al. 2008; Ellison et al. 2021). The viscous timescale is much longer than the gas depletion time for all radii. Therefore, there must be external accretion onto the galactic disk to maintain the observed SFR for more than a few gigayears.

We computed the CO and HCN conversion factor profiles of NGC 6946 (see Fig. 2, panels g and h). For both χ^2 calculations, the CO-to- H_2 conversion factors increase from the galaxy center to the edge of the CO emission distribution, with a mean α_{CO} close to the Galactic value of $\alpha_{\text{CO}}^{\text{MW}} = 4.36 M_{\odot} \text{ pc}^{-2} (\text{K km s}^{-1})^{-1}$ (Bolatto et al. 2013).

The HCN-to-dense gas conversion factor, defined as the ratio between the flux I_{HCN} and the molecular gas formed in clouds with density over $n = 3 \times 10^4 \text{ cm}^{-3}$, of the model with $\chi_{\text{CO}(1-0)}^2$ in χ_{tot}^2 is about a factor of two higher than the value of $\alpha_{\text{HCN}} = 10 M_{\odot} \text{ pc}^{-2} (\text{K km s}^{-1})^{-1}$ (Gao & Solomon 2004) and consistent with the value found by Wu et al. (2010). Since the model underpredicts the observed HCN emission by a factor of two, the model HCN conversion factor is probably overestimated by the same factor. On the other hand, the HCN-to-dense gas conversion factor of the model without $\chi_{\text{CO}(1-0)}^2$ in χ_{tot}^2 is about a factor of two lower than the value of Gao & Solomon (2004). The difference is mainly caused by higher HCN abundances at a cosmic ray ionization rate of $\zeta_{\text{CR}} = 10^{-17} \text{ s}^{-1}$ compared to the HCN abundances at a three times lower ζ_{CR} . We estimate the HCN conversion factor to be $\alpha_{\text{HCN}} = 5-10 M_{\odot} \text{ pc}^{-2} (\text{K km s}^{-1})^{-1}$. In both models the HCN-to-dense gas conversion factor decreases within the inner kpc.

4.2. The galaxy sample

In this section we review the results obtained for the other galaxies of the sample. The $\chi_{\text{CO}(1-0)}^2$ and $\chi_{\text{CO}(2-1)}^2$ are those calculated with excitation temperatures obtained from the method outlined in Appendix A.2.5. The corresponding figures, which show the integrated line emission based on the results of RADEX, are available in Appendix B, ordered in the same way as in Tables 3 and 4.

We first discuss the galaxies for which EMPIRE data are available (Table 3). Whereas most of these galaxies have a χ_{tot}^2 including $\chi_{\text{CO}(1-0)}^2$ between 200 and 400, the χ_{tot}^2 of NGC 3627 and NGC 6946 are 1053 and 2102, respectively. As discussed in Sect. 4.1, the high χ_{tot}^2 of NGC 6946 is caused by an overestimation of the central SFR. In NGC 3627, the star formation and HI radial profiles could not be fitted in a satisfactory way. The model without $\chi_{\text{CO}(1-0)}^2$ reproduces the available observations significantly better than the model with $\chi_{\text{CO}(1-0)}^2$ in the χ_{tot}^2 calculations. We thus adopted the model with $\chi_{\text{CO}(1-0)}^2$ in χ_{tot}^2 for all EMPIRE galaxies except NGC 3627.

For all EMPIRE galaxies the model infrared profiles are broadly consistent with observations. In general, the model infrared profiles are steeper than the observed infrared profiles. This effect becomes stronger at smaller wavelengths. The preferred CR ionization rate is $\zeta_{\text{CR}} = 10^{-18} \text{ s}^{-1}$.

For all EMPIRE galaxies except NGC 6946 the Toomre parameter Q_{gas} decreases with radius. The highest central Q_{gas}

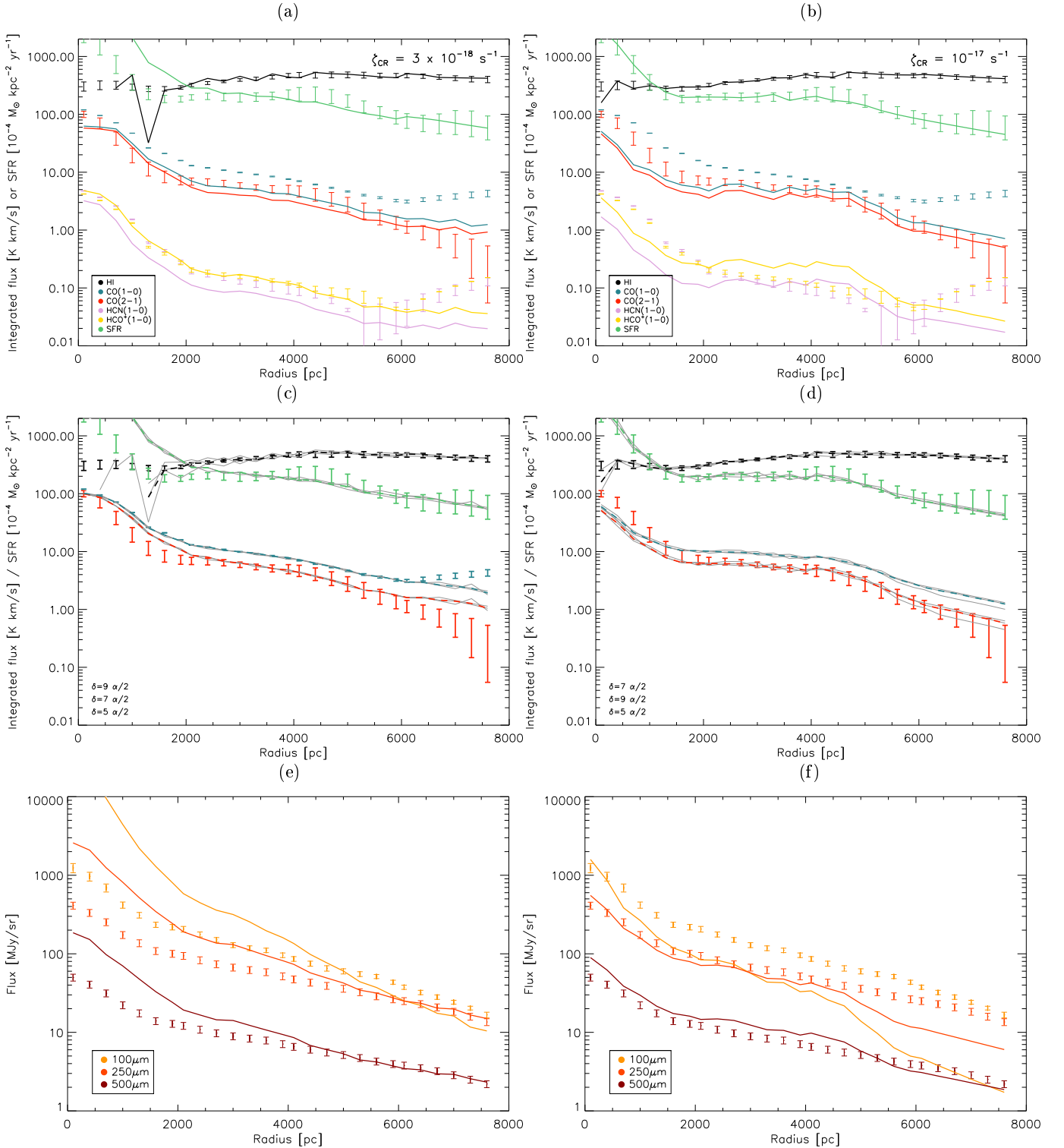


Fig. 1. NGC 6946. Errors bars correspond to the observations. Solid lines correspond to the median results of the best-fit models and thin gray lines to the best-fit models. The values of the secondary parameters for these best-fit models are given in the lower-left corner of the *middle panels*. (a) Best-fit model including χ^2_{CO10} using RADEX. (b) Best-fit model without χ^2_{CO10} using RADEX. (c) Best-fit models including χ^2_{CO10} . (d) Best-fit models without χ^2_{CO10} . (e) Infrared profiles of the best-fit model including χ^2_{CO10} . (f) Infrared profiles of the best-fit model without χ^2_{CO10} . The cosmic ray ionization rate ζ_{CR} is given for each model in the *upper panels*.

are found in NGC 628 and NGC 5055 ($Q \sim 8$). In NGC 3627 the Toomre parameter decreases from $Q_{\text{gas}} = 4-6$ in the galaxy center to $Q_{\text{gas}} = 1.5-2$ at $R = 5$ kpc. The NGC 5194 model yields a Toomre parameter, which decreases from $Q_{\text{gas}} = 2$ in the center to about unity at $R = 1.5$ pc.

The radial profiles of the mass accretion rate generally increase with radius. In NGC 628 and NGC 3184 the mass accretion rate increases in the inner 2 kpc and stays approximately constant at larger radii. The mass accretion rate is about constant $\dot{M} \sim 0.1 M_{\odot} \text{ yr}^{-1}$ in NGC 3627 and NGC 5055. In NGC 5194 the

Table 6. Determination of the HCN and HCO⁺ best-fit models for different cosmic ray ionization rates ζ_{CR} .

Galaxy	With $\chi^2_{\text{CO}(1-0)}$			Without $\chi^2_{\text{CO}(1-0)}$		
	10^{-17} s^{-1}	$3 \times 10^{-18} \text{ s}^{-1}$	10^{-18} s^{-1}	10^{-17} s^{-1}	$3 \times 10^{-18} \text{ s}^{-1}$	10^{-18} s^{-1}
NGC 628	710	121	74	2485	490	202
NGC 3184	16 781	3594	3348	10 373	2032	2217
NGC 3627	826	422	502	4209	594	349
NGC 5055	8468	1264	257	74 241	16433	6849
NGC 5194	13 747	5370	4316	8130	6658	6026
NGC 6946	175 271	5524	6751	20 430	37 300	41 532

Notes. The bold characters correspond to the lowest χ^2 for each of the galaxies.

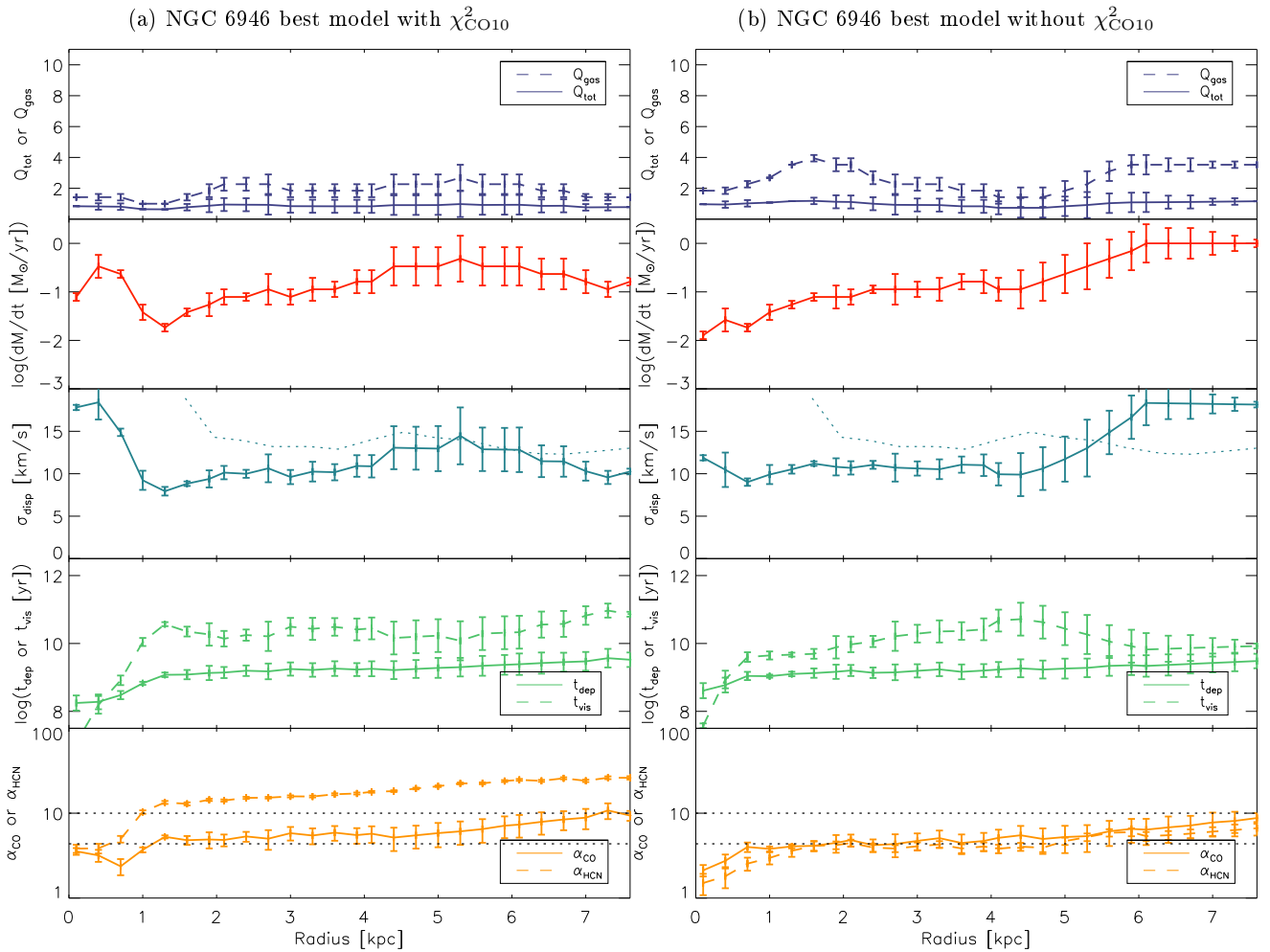


Fig. 2. NGC 6946: radial profiles of the main physical quantities with and without χ^2_{CO} in calculations. *First panels:* (dark blue) show the total (solid) and gaseous (dashed) Toomre Q parameter. *Second panels:* (red) show the mass accretion rate \dot{M} . *Third panels:* (blue) show the velocity dispersion profiles σ_{disp} (solid) with the observed HI moment-2 linewidth (Caldú-Primo et al. 2013; dotted). *Fourth panels:* (green) show the depletion (t_{dep} ; solid) and viscous (t_{vis} ; dashed) timescales. *Fifth panel:* (yellow) shows the CO-to-H₂ (α_{CO} ; solid) and HCN-to-dense gas (α_{HCN} ; dashed) conversion factors. Dotted lines correspond to the Galactic value of $\alpha_{\text{CO}}^{\text{MW}} = 4.36 M_{\odot} \text{ pc}^2 (\text{K km s}^{-1})^{-1}$ and the Gao & Solomon value $\alpha_{\text{HCN}}^{\text{MW}} = 10 M_{\odot} \text{ pc}^2 (\text{K km s}^{-1})^{-1}$.

mass accretion rate is about $\dot{M} = 10^{-2} M_{\odot} \text{ yr}^{-1}$ in the inner disk and increases to almost $10^{-1} M_{\odot} \text{ yr}^{-1}$ at $R = 5.5$ kpc.

The resulting velocity dispersions are about 10 km s^{-1} in NGC 628, NGC 3184, NGC 3627, and NGC 5055. They are consistent with observations when available. In NGC 5194, $\sigma_{\text{disp}} \sim 8 \text{ km s}^{-1}$, significantly lower than the observed velocity dispersion of $\sim 15 \text{ km s}^{-1}$. The high observed velocity dispersion could

be due to noncircular motions induced by the gravitational interaction with NGC 5195. The strong increase in the model velocity dispersion at $R = 7$ kpc is not observed.

The CO conversion factors are fairly constant or increase slightly with radius. Whereas NGC 628 and NGC 3184 show a CO conversion factor about twice as high as the Galactic value, those of NGC 3627 and NGC 5055 are about Galactic.

In NGC 5194 the CO conversion factor increases slightly from the Galactic value at $R = 1$ kpc to 1.5 times this value at $R = 4$ kpc. Like CO conversion factors, the HCN conversion factors are fairly constant or increase slightly with radius. The HCN conversion factor is close to the Gao & Solomon value in NGC 5055 and somewhat lower than the Gao & Solomon value in NGC 628, NGC 3184, and NGC 5194. The lowest HCN conversion factor is found in NGC 3627. All conversion factors, except the CO conversion factor in the outer disk of NGC 3184, are located within the observed ranges ($3 \leq \alpha_{\text{HCN}} \leq 30 M_{\odot} \text{pc}^2 (\text{K km s}^{-1})^{-1}$, Onus et al. 2018; $2 \leq \alpha_{\text{HCN}} \leq 10 M_{\odot} \text{pc}^2 (\text{K km s}^{-1})^{-1}$, Bolatto et al. 2013). In four out of six EMPIRE galaxies the CO conversion factor exceeds the HCN conversion factor.

Whereas the radial profiles of the gas depletion timescale are relatively flat in all EMPIRE galaxies, those of the viscous timescales increase with radius. In all EMPIRE galaxies the viscous timescale exceeds the gas depletion timescale for $R > 1$ kpc.

For the rest of the massive galaxies ($M_* > 10^{10} M_{\odot}$), where no EMPIRE data are available, the model is able to fit the observational profiles in a satisfactory way. The χ_{tot}^2 of NGC 2841, NGC 3198, and NGC 4736 are the lowest of all galaxies, with values below 30. With a value of 270, NGC 3521 shows the highest χ_{tot}^2 (including only $\chi_{\text{CO}(2-1)}^2$) of the whole galaxy sample. This is mainly due to an underestimation of the model CO(2–1) integrated line emission. Nevertheless, we consider that this is still an acceptable fit. The resulting radial profiles of Q_{gas} and \dot{M} are similar to those described above.

The model velocity dispersion profiles are approximately flat except for those of NGC 3521 and NGC 7331, where the velocity dispersion suddenly increases by $\sim 8 \text{ km s}^{-1}$ in the outer disk. We think that this is a limitation of the model, which needs to significantly increase the value of \dot{M} in the regions where the SFR changes from a molecular-gas-dominated regime to an atomic-gas-dominated one (i.e., where the CO flux becomes negligible compared to the HI flux) to fit the observational profiles satisfactorily (see Sect. 4.3.1). The viscous timescales are significantly higher than the gas depletion times in all galaxies. The CO conversion factors are approximately constant around one half and twice the Galactic value. Only NGC 3351 shows a CO conversion factor that exceeds twice the Galactic value.

For most of the low-mass galaxies ($M_* < 10^{10} M_{\odot}$) where no EMPIRE data are available, the χ_{tot}^2 are considerably higher than those found for the high-mass galaxies, with values ranging from about 3000 for NGC 2976 to more than 7000 for NGC 925. For each of the low-mass galaxies, the fit of the CO(2–1) and SFR profiles becomes worse in the outer galactic disk. Whereas the molecular depletion times of the inner disks are similar to that commonly observed in star-forming spiral galaxies (Bigiel et al. 2008; Leroy et al. 2008), they are significantly higher in the outer disks of the low-mass galaxies, except for NGC 7793. The model cannot accommodate these high molecular depletion times, which leads to the high χ_{tot}^2 . We can only speculate that gas compression due to external accretion might be the cause of such a large amount of molecular gas in the outer disks of low-mass galaxies, which forms stars with a significantly lower efficiency than in the inner disk. A high Toomre parameter $Q_{\text{gas}} \sim 8$ is found in the inner disks of NGC 2403, NGC 2967, NGC 4214, and NGC 7793 decreasing to $Q_{\text{gas}} \sim 1.5$ – 2 in the outer disks. The observed infrared profiles of all low-mass galaxies are well reproduced by the model. In contrast to the high-mass galaxies, the radial profiles of the model gas velocity dispersion slightly decrease with radius. Where measured, the

model profiles are consistent with the observed profiles. The viscous timescales exceed the gas depletion time in NGC 2403, NGC 2967, NGC 4214, and NGC 7793 beyond $R \sim 2R_{\text{d}}$, the radius within which half of the galaxy’s luminosity is contained. The CO conversion factors all increase with radius. In the outer disks they are significantly higher than the Galactic value.

4.3. General results

In this section we summarize and generalize the results obtained for all galaxies.

4.3.1. Toomre parameters Q , accretion rate \dot{M} , and turbulent velocity dispersion v_{turb}

The Toomre Q parameter can be interpreted as a stability criterion, where disks with $Q < 1$ are subject to fragmentation (see Eq. (A.18)). It can also be interpreted as a measure of the gas mass with respect to the maximum stable gas mass ($Q_{\text{gas}} = 1$) for a given angular velocity and gas velocity dispersion. The radial profiles of the Toomre parameters Q_{gas} generally decrease with radius (Fig. 3). We found $Q_{\text{gas}} > 5$ in the central parts of six galactic disks. In the outer parts of the disks Q_{gas} rarely exceeds $Q_{\text{gas}} = 3$. An exception is NGC 2841, where $Q_{\text{gas}} > 4$ in the entire gas disk. The total (gas and stars) Toomre parameter Q_{tot} exceeds unity in the inner disk of a significant number of galaxies. Q_{tot} is close to unity in the outer disks, except for NGC 628 and NGC 2841.

In all massive galaxies except NGC 3351, the mass accretion rate increases with radius from $\dot{M} \sim 10^{-2} M_{\odot} \text{yr}^{-1}$ in the center to $\dot{M} \sim 10^{-1} M_{\odot} \text{yr}^{-1}$ at the edge of the CO distribution (Fig. 3). Three low-mass galaxies show the opposite trend. In addition, NGC 925 and NGC 7793 have roughly constant mass accretion rates. Our mass accretion rates ($\sim 0.1 M_{\odot} \text{yr}^{-1}$) are significantly lower than those derived by Schmidt et al. (2016), which can reach up to $\sim 1 M_{\odot} \text{yr}^{-1}$. They are consistent with the net mass accretion rates derived by Di Teodoro & Peek (2021): in their sample of 54 local spiral galaxies all galactic disks show some degree of radial gas flows, with radial velocities typically of a few km s^{-1} , but these flows do not seem to have a preferential direction. As a consequence, the average radial velocity and mass flow rate across the sample at a given radius are nearly constant and close to zero.

The Toomre parameter Q and the accretion rate \dot{M} are partially degenerate: an increase in either parameter leads to an increase in the turbulent velocity dispersion of the gas. In the massive galaxies, an increase in the accretion rate is accompanied by a decrease in the Toomre parameter, leading to a relatively constant velocity dispersion around the canonical value of $v_{\text{turb}} \sim 10 \text{ km s}^{-1}$ (Fig. 4). The velocity dispersions of the less massive galaxies decrease with radius. We need to take into account the finite lifetime of molecular clouds ($f_{\text{mol}}^{\text{life}}$) for the molecular gas fraction (Eq. (A.23)). Models without the finite lifetime systematically lead to radially increasing profiles of the gas velocity dispersion, which is contrary to observations. The slight increase in the velocity dispersion profiles close to the edge of the CO distribution can be explained by the difficulty of the model to fit regions with very low molecular gas surface densities in the outer galactic disks where the gas is dominated by the atomic phase. To fit the HI and SFR observational profiles, the accretion rate has to be significantly increased within the model, resulting in an increase in the velocity dispersion. However, this result is contrary to observations (Caldú-Primo et al. 2013; Injamasimanana et al. 2015). We observe the strongest

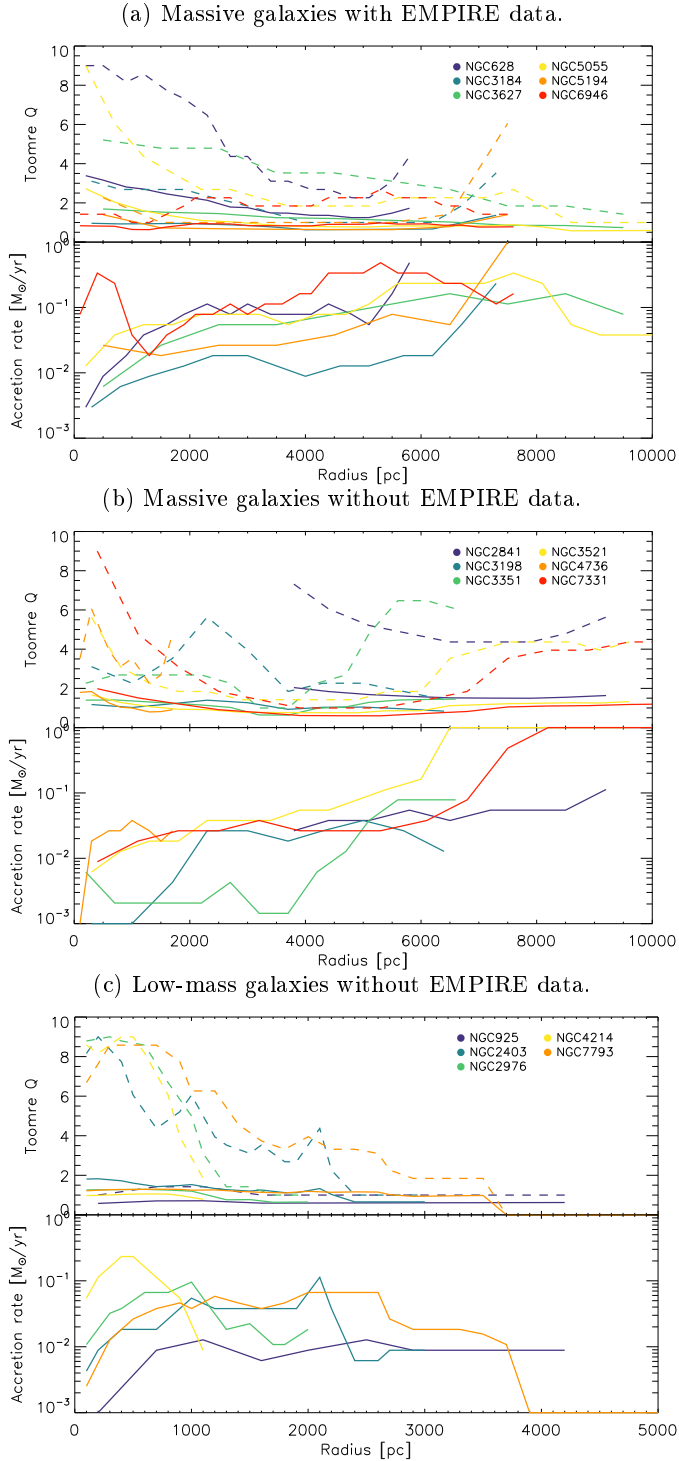


Fig. 3. Toomre parameter Q (solid: Q_{tot} ; dashed: Q_{gas}) and mass accretion rate \dot{M} of the high-mass galaxies with EMPIRE data (*upper panel*), high-mass galaxies without EMPIRE data (*middle panel*), and low-mass galaxies (*lower panel*; $M_* < 10^{10} M_{\odot}$).

discrepancy between our velocity dispersion profiles and the observed profiles for NGC 3521 and NGC 7331. In these galaxies, the velocity dispersion increases sharply at $R \sim 6\text{--}7$ kpc.

This behavior is caused by a change in the regime of energy injection. Whereas in the inner disk the energy injection by SNe dominates, the energy injection through accretion (Eq. (A.5)) is comparable to that of SNe in the outer disks of NGC 3521,

and NGC 7331. Indeed, model calculations without the additional term of energy injection due to accretion show no sudden increase in the gas velocity dispersion in the outer disk (dashed lines in the middle panel of Fig. 4). The sudden increase in the velocity dispersion can also be avoided by a decrease in the gravitational potential of the galactic disk. This can be achieved by a local increase in the stellar velocity dispersion by a factor of two compared to our best fit models. Since NGC 7331 already needs an increase in the stellar velocity dispersion to fit the available data, a further increase might not be realistic. Alternatively, it is expected that an increase in the metallicity in the outer disk also leads to a decrease in the gas velocity dispersion. However, this would flatten the metallicity gradient of these galaxies, which is not consistent with the observed metallicity gradient (Moustakas et al. 2010). As a third possibility the star-formation timescale might be increased in the outer disk (Vollmer & Leroy 2011). These authors replaced the local free-fall time by the molecule formation time as the relevant timescale for star formation in the outer galactic disk. All these modifications increase the molecular gas depletion time.

We compared the profiles of the Toomre parameter Q and the mass accretion rate \dot{M} of the model with the values presented by Vollmer & Leroy (2011) where the gas velocity dispersion was included in the χ^2 calculations and the radial profile of Q was given as input and \dot{M} was constant for the entire disk. In addition, Vollmer & Leroy (2011) assumed a Galactic CO conversion factor. The mass accretion rate was determined by the total SFR of the galactic disks. In particular, our model of NGC 5194 led to a significantly better fit to the available observations than the Vollmer & Leroy (2011) model.

The models of 6 out of 17 galaxies have mass accretion rates that are more than three times lower than those of the Vollmer & Leroy (2011) model for the following reasons: in NGC 5055, NGC 4736, and NGC 7331 Vollmer & Leroy (2011) used the observed HI velocity dispersions of Tamburro et al. (2009), which are more than 5 km s^{-1} higher than those obtained by our model. Given that the observed velocity dispersions are upper limits because of the beam smearing of noncircular motions, we are confident that our model yields more realistic mass accretion rates for these galaxies. NGC 3351 shows a particularly low mass accretion rate. Whereas our model preferred $Q_{\text{gas}} \sim 2.5$, Vollmer & Leroy (2011) set $Q = 8$. Again, our gas velocity dispersion is significantly smaller than that of Vollmer & Leroy (2011). The same observation is true for NGC 925 and NGC 2976. We conclude that Q_{gas} , \dot{M} , and thus σ_{disp} might have been overestimated by Vollmer & Leroy (2011).

4.3.2. Ionization rate ζ_{CR}

Without any source of ionization, the network of reactions responsible for the great richness of the ISM cannot be initiated. The dominant mechanism responsible for the ionization of molecules in dense clouds is cosmic ray ionization. The cosmic ray ionization rate ζ_{CR} was estimated by many studies, resulting in a range from more than 10^{-16} s^{-1} for diffuse regions to a few 10^{-18} s^{-1} for the densest gas clouds (e.g., Spitzer & Tomasko 1968; van Dishoeck & Black 1986; Indriolo et al. 2007). Indriolo & McCall (2012) investigated the value of ζ_{CR} in diffuse regions and found that the rate varies around an average value of $\zeta_{\text{CR}} = 3 \times 10^{-16} \text{ s}^{-1}$. Within

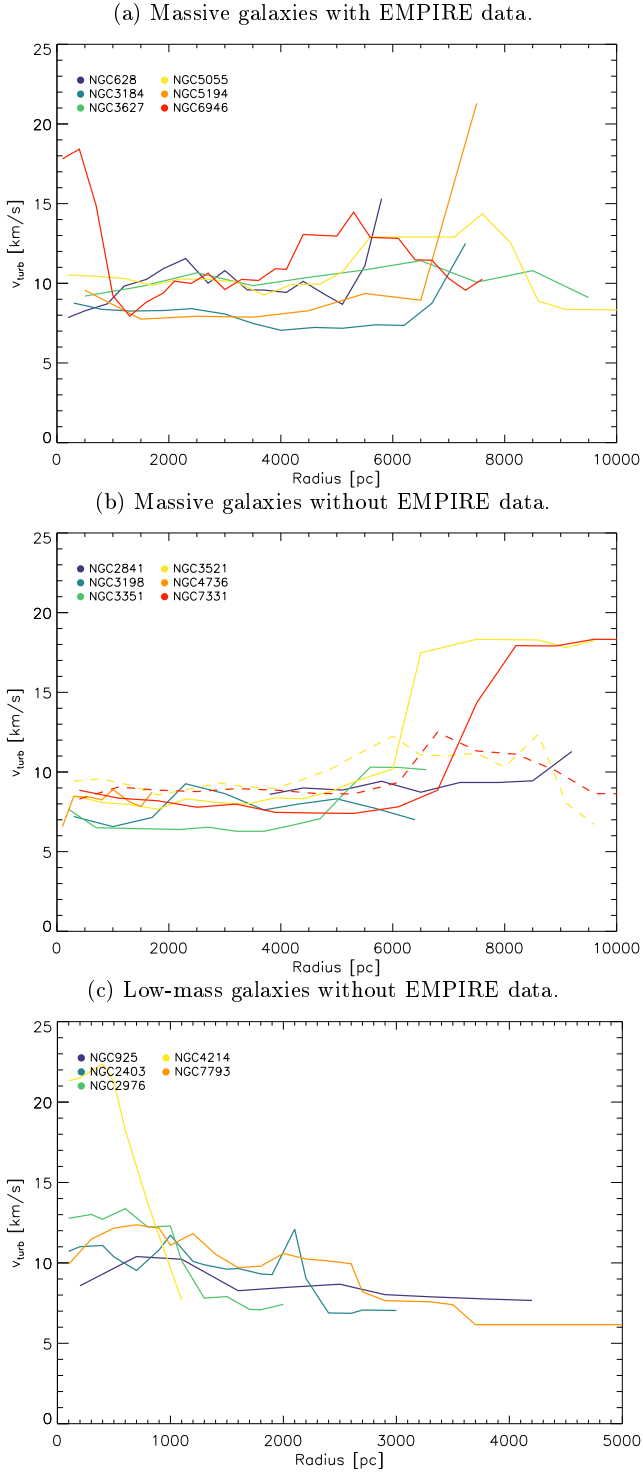


Fig. 4. Gas velocity dispersion profiles $\sigma_{\text{disp}} = \sqrt{v_{\text{turb}}^2 + c_s^2}$ of the high-mass galaxies with EMPIRE data (*upper panel*), high-mass galaxies without EMPIRE data (*middle panel*), and low-mass galaxies (*lower panel*; $M_* < 10^{10} M_\odot$). The dashed lines are for NGC 3521 and NGC 7331 models without the term for turbulent energy injection due to the gain of potential energy (Eq. (A.5)).

dense molecular clouds, the cosmic ray ionization rates cover a range of about two orders of magnitude (10^{-18} – 10^{-16} s^{-1}) and are subject to considerable uncertainties (Padovani et al. 2009). Dalgarno (2006) suggested that $\zeta_{\text{CR}} = 10^{-17} \text{ s}^{-1}$ corresponds to the lower limit of the ionization rate in dense regions. In

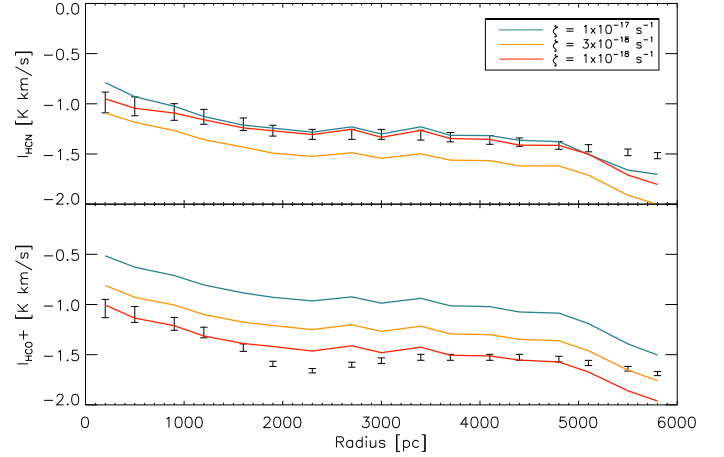


Fig. 5. NGC 628: best-fit models of HCN and HCO⁺ integrated line emission with different cosmic ray ionization rates ζ_{CR} .

our model ζ_{CR} is mainly determined by the HCO⁺ abundance. In addition, a decrease in ζ_{CR} leads to a slight decrease in the CO emission and a slight variation of the HCN line emission. The model HCO⁺-to-CO emission ratio is approximately proportional to ζ_{CR} . NGC 628 shows the lowest HCO⁺-to-CO ratio. The comparison of the best-fit models for NGC 628 with the different values of ζ_{CR} is presented in Fig. 5. We found that only the model using an ionization rate of $\zeta_{\text{CR}} = 10^{-18} \text{ s}^{-1}$ is able to reproduce the observed HCO⁺-to-CO and HCN-to-HCO⁺ ratio. This value is at the lower end of the range given by Padovani et al. (2009).

For all galaxies included in the EMPIRE survey, we varied the value of ζ_{CR} to determine the CR ionization rate that provides the best fit to the observed emission line profiles. The $\chi^2_{\text{dense}} = \chi^2_{\text{HCN}} + \chi^2_{\text{HCO}^+}$ for the different ionization rates $\zeta_{\text{CR}} = 10^{-17}$, 3×10^{-18} and, 10^{-18} s^{-1} are presented in Table 6. For most galaxies, a cosmic ray ionization rate smaller than $\zeta_{\text{CR}} = 10^{-17} \text{ s}^{-1}$ is needed.

4.3.3. Molecular line emission as a function of density

Star formation occurs in the densest regions of the ISM, within GMCs. In general, the SFR correlates with the available amount of molecular gas, whose main tracer is CO emission (Schmidt 1959). CO emission traces gas with densities $n \gtrsim 100 \text{ cm}^{-3}$. Gas of higher densities can be detected in the HCN and HCO⁺ lines (e.g., Gao & Solomon 2004). Gao & Solomon (2004) defined the dense gas fraction as the ratio between the gas mass with densities $n(\text{H}_2) > 3 \times 10^4 \text{ cm}^{-3}$ and the total gas mass. They found a linear relationship between the infrared and HCN luminosities, which they interpreted as a linear relation between the SFR and the dense gas mass. Mangum & Shirley (2015) and Kauffmann et al. (2017) questioned the hypothesis that HCN is mainly emitted by dense gas. Based on observations of the Orion A cloud, they found that HCN is already emitted from regions with a density of approximately $n(\text{H}_2) \sim 10^3 \text{ cm}^{-3}$. For the calculations of the HCN-to-dense gas model conversion factor, we use the definition of the dense gas fraction of Gao & Solomon (2004). To investigate at which densities most of the HCN is emitted, we show the brightness temperatures as a function of gas density for the CO(2–1), HCN(1–0) and HCO⁺(1–0) lines

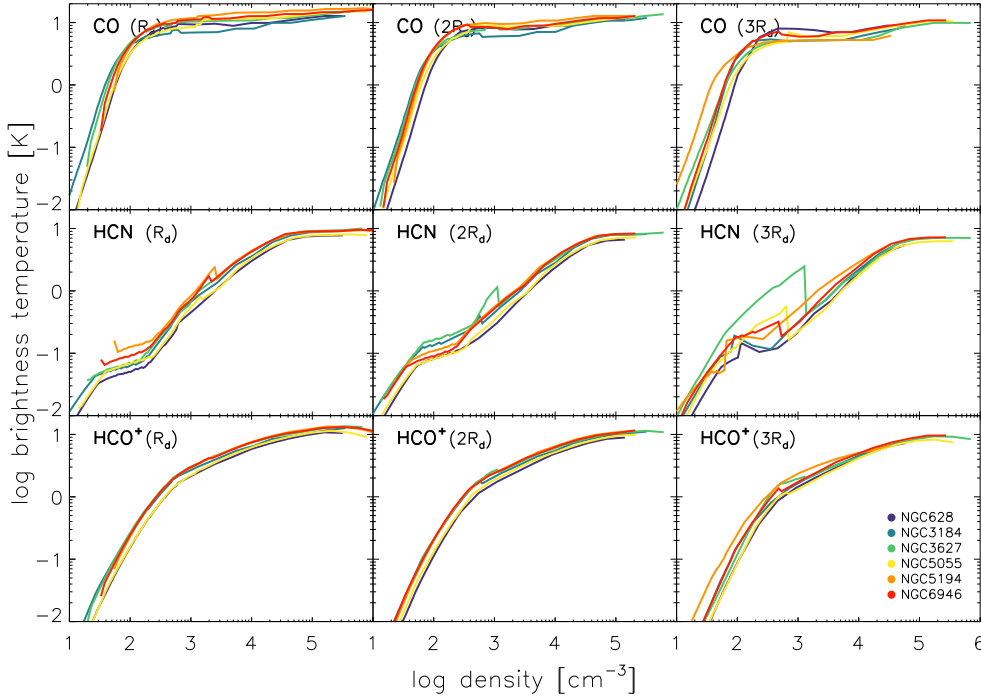


Fig. 6. CO(2–1), HCN(1–0), and HCO⁺(1–0) brightness temperature as a function of gas density. From left to right, the panels correspond to one to three times the characteristic length scale of the stellar disk R_d .

at three galactic radii for the EMPIRE galaxies in Fig. 6. The dependence of the brightness temperatures on galactic radius is weak. The model CO brightness temperatures of the different galaxies are quite uniform. The CO brightness temperature reaches the typical sensitivity of ALMA observation of ~ 0.1 K at densities between 20 and 30 cm^{-3} . Likewise, the HCN and HCO⁺ brightness temperatures are homogeneous except for NGC 3627, which shows higher HCN brightness temperatures for densities $500 \lesssim n \lesssim 1000 \text{ cm}^{-3}$ at $R = 2R_d$ and $100 \lesssim n \lesssim 1000 \text{ cm}^{-3}$ at $R = 3R_d$.

In the model, the CO(2–1) brightness temperature reaches its maximum at a few 100 cm^{-3} . The CO brightness temperature exceed 1 K for densities higher than $\sim 10^2 \text{ cm}^{-3}$, those of HCN and HCO⁺ at densities higher than $\sim 10^3 \text{ cm}^{-3}$. The HCN brightness temperature increases for density from 10^2 to 10^3 cm^{-3} and then stays constant at about 1 K. The HCO⁺ gradually increases from 10^2 to 10^4 cm^{-3} .

We used the brightness temperatures to calculate the integrated line emission using Eq. (A.29). The resulting integrated line emission as a function of density is presented in Fig. 7. The peak of the integrated line emission around $n \sim 10^3 \text{ cm}^{-3}$ occurs close to the transition between the diffuse and self-gravitating gas in our analytical model. The additional factor of 0.6 (Appendix A.2.1) decreases the integrated line emission of self-gravitating clouds. In the inner part of the galaxy ($R \sim R_d$, the disk scale length) the CO line emission mostly originates in diffuse (i.e., non-self-gravitating) gas of density $n < 10^3 \text{ cm}^{-3}$. A non-negligible fraction of the HCN and HCO⁺ emission originates from gas at these densities as well.

By integrating the line intensities of Fig. 7, we determined the density at which half of the line flux is emitted (Table 7). At $R = R_d$, we found average values of $n_{(1/2)} \sim 200\text{--}500 \text{ cm}^{-3}$ for CO(2–1), $n_{(1/2)} \sim 1000\text{--}3000 \text{ cm}^{-3}$ for HCN(1–0), and about $n_{(1/2)} \sim 1000\text{--}3000 \text{ cm}^{-3}$ for HCO⁺. None but one of the mid-flux densities significantly changes with radius by more than a factor of three. The HCN and HCO⁺ mid-flux density thresholds

are low compared to the thresholds usually assumed in the literature in dense gas clouds $3 \times 10^4 \text{ cm}^{-3}$; (Gao & Solomon 2004). These high densities are based on assumed HCN and HCO⁺ brightness temperature of about 30 K (Gao & Solomon 2004). Leroy et al. (2017) found that lognormal gas distributions with low mean densities and small widths generate most of their HCN emission from low densities $\lesssim 10^3\text{--}10^4 \text{ cm}^{-3}$. If a power law tail is added to the distribution most HCN is emitted by gas with densities exceeding 10^4 cm^{-3} . Onus et al. (2018) calculated the HCN emission from simulated dense, star-forming cores and found that HCN emission traces gas with a luminosity-weighted mean number density of $\sim 10^4 \text{ cm}^{-3}$. Based on 100 pc resolution observations of NGC 3627, Bešlić et al. (2021) found that HCN and HCO⁺ to CO(2–1) line ratios show greater scatter than ¹³CO and C¹⁸O to CO(2–1) line ratios, which might suggest that they trace densities above the mean molecular gas density. On the other hand, Liszt & Pety (2016) showed that the HCN and HCO⁺ lines can be excited and detected in diffuse gas because the emission brightness at the limit of detectability is independent of the critical density and varies only as the $n(\text{H})\text{--}N(\text{HCN})$ product.

We also computed the fractional integrated line intensity for $n > 10^3, 10^{3.5}, 10^4$, and $10^{4.5} \text{ cm}^{-3}$ (Table C.1). A significant fraction of the HCN (25–30%) and HCO⁺ (15–20%) emission stems from gas with densities exceeding $n = 10^4 \text{ cm}^{-3}$. Pety et al. (2017) studied the ratio of the molecular line fluxes originating from the dense gas within the Orion B GMC. Based on 0.04 pc resolution observations within a field of view of $5.6 \times 7.5 \text{ pc}$, they found that the fraction of the total flux emitted from the densest regions with $n > 7.3 \times 10^3 \text{ cm}^{-3}$ corresponds to 8% for the CO, 18% for the HCN, and 16% for the HCO⁺. Since the mean density $n_{\text{H}_2} \sim 400 \text{ cm}^{-3}$ (Pety et al. 2017) of the Orion B cloud is comparable to the density of self-gravitating clouds in our model, the comparison of their flux fractions to the corresponding model flux fractions is relevant for the HCN and HCO⁺ emission. We calculated the flux ratios based on the model profiles with the same density thresholds. The results are presented in Table 8. There is little variation of the flux ratios at

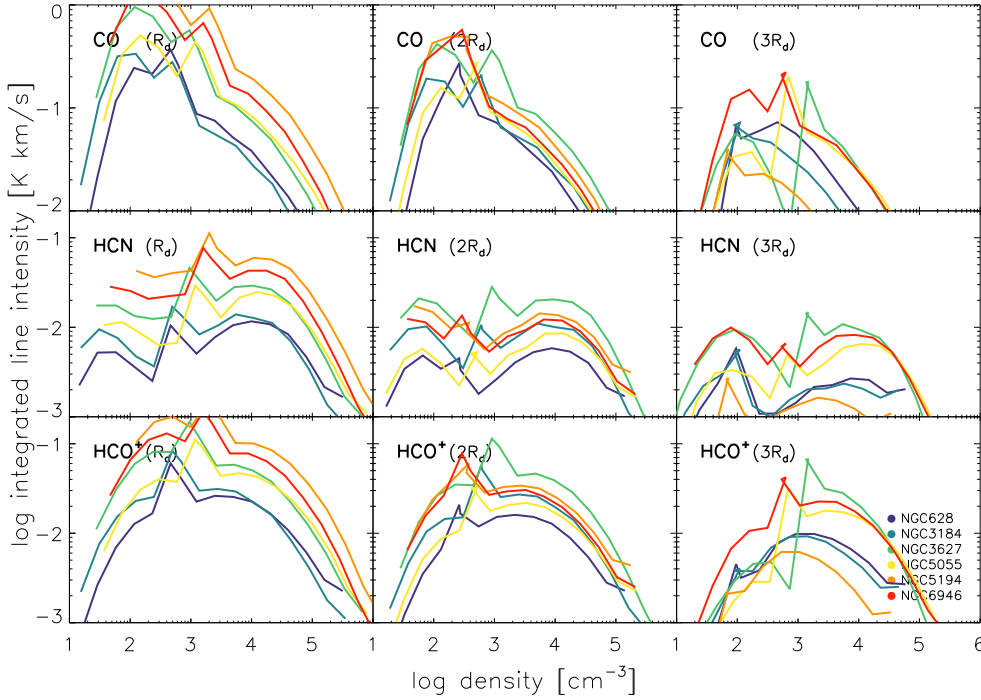


Fig. 7. CO(2–1), HCN(1–0), and HCO⁺(1–0) integrated line intensity as a function of gas density. From left to right, panels correspond to one to three times the characteristic length scale of the disk R_d .

the three different galactic radii. Our CO and HCO⁺ flux ratios at $R = 3 \times R_d$ (roughly solar radius) are comparable to the values given by Pety et al. (2017) whereas our HCN flux ratio is about 50% higher than the ratio found by these authors. Within our model the flux fraction depends on the probability density distribution of the gas density and the brightness temperature of the molecular lines, which in turn depends on the gas dispersion velocity, density, molecular gas surface density, and temperature. A sizable fraction of the model CO emission is produced by dense, non-self-gravitating gas at larger scales than those of GMCs. It is somewhat surprising that the CO flux fraction within a GMC, as Orion B, is comparable to our model CO flux fraction.

4.3.4. Conversion factors

In most galaxies the radial profiles of the CO conversion factor increase monotonically with radius (Fig. 8). The conversion factors range between half and twice the Galactic value in most of the galaxies. Notable exceptions are NGC 3351 and the outer disks of NGC 2976 and NGC 4214 where the CO conversion factors are higher than twice the Galactic value. Our CO conversion factors are about 50% higher than those found by Sandstrom et al. (2013) (Table 9). There is a big discrepancy for NGC 4736 where our CO weighted conversion factor is five times higher than that of Sandstrom et al. (2013). Likewise, our model CO conversion factor in the inner kpc of NGC 3351 is about a factor of five higher than that of Teng et al. (2022) based on 100 pc resolution ¹²CO, ¹³CO, and C¹⁸O observations and assuming a CO abundance of 3×10^{-4} . A lower CO abundance caused by a low metallicity, as suggested by Díaz et al. (2007), decreases the difference between the Teng et al. (2022) and our conversion factors.

The models suggest that the conversion factors are slightly sub-Galactic in the center and exceed the Galactic value by up to a factor of two at the edge of the CO-emitting disk. For the HCN-to-dense gas conversion factor, the model yields values between half and twice the Gao & Solomon value. As for α_{CO} , the radial

profiles tend to increase slightly from the galaxy center to the edge of the molecular disk.

4.3.5. Gas depletion and viscous timescales

The radial profiles of the gas depletion and viscous timescale are presented in Fig. 9. For all massive galaxies, except NGC 628, the viscous timescales exceed the depletion timescales for $R > R_d$ by a factor of about ten. For NGC 628, t_{vis} is particularly small in the inner 2.5 kpc, and close to the gas depletion timescale of 2–3 Gyr.

For the low-mass galaxies, with $M_* < 10^{10} M_\odot$, the model yields $t_{vis} \leq t_{dep}$ up to $R \sim 2 R_d$ for NGC 4214, NGC 2403, and NGC 7793 and up to $R \sim R_d$ for NGC 2976. This suggests that for low-mass galaxies, star formation can be maintained by radial gas accretion within the disk from the center to $R \sim 2 R_d$ (see also Vollmer & Leroy 2011). On the other hand, for massive galaxies ($M_* > 10^{10} M_\odot$) external gas accretion is needed to supply star formation with fresh gas, especially in the inner disk region. In the absence of external gas accretion, the gas surface density of the inner disk will significantly decrease within a few gigayears, leading to a high Q_{gas} and to a Q_{tot} exceeding unity (see Sect. 4.3.1). Condensation of halo gas on galactic fountains (e.g., Fraternali 2017) might be an important source of gas accretion onto the inner galactic disk.

5. Discussion

5.1. Low cosmic ray ionization rates ζ_{CR}

As discussed in Sect. 4.3.2, our model requires particularly low ionization rates to reproduce the observed HCO⁺ radial profiles. Our initial assumption of $\zeta_{CR} = 10^{-17} \text{ s}^{-1}$ corresponds already to the lower limit suggested by Dalgarno (2006). In general, lower cosmic ray ionization rates are derived in gas of higher densities (Padovani et al. 2009; Neufeld & Wolfire 2017). For four out of six EMPIRE galaxies (NGC 628, NGC 3184, NGC 5055,

Table 7. Density thresholds where 50% of the total flux is emitted, in cm^{-3} .

Galaxy	R_d			$2 R_d$			$3 R_d$		
	CO(2–1)	HCN(1–0)	HCO ⁺ (1–0)	CO(2–1)	HCN(1–0)	HCO ⁺ (1–0)	CO(2–1)	HCN(1–0)	HCO ⁺ (1–0)
NGC 628	377	1241	4961	275	2200	2200	461	1843	1843
NGC 3184	153	688	2751	247	1263	1263	180	359	1435
NGC 3627	193	1310	2620	243	1197	1197	1367	1367	2734
NGC 5055	315	1557	6227	426	3402	1701	704	5630	2815
NGC 5194	309	1630	2717	251	1378	689	267	1065	1065
NGC 6946	247	1839	2202	238	1633	817	537	1074	1074

Table 8. Percentage of total flux originating from dense clouds ($n > 7.3 \times 10^3 \text{ cm}^{-3}$; Pety et al. 2017).

Galaxy	R_d			$2 R_d$			$3 R_d$		
	CO(2–1)	HCN(1–0)	HCO ⁺ (1–0)	CO(2–1)	HCN(1–0)	HCO ⁺ (1–0)	CO(2–1)	HCN(1–0)	HCO ⁺ (1–0)
NGC 628	7%	43%	26%	7%	38%	26%	8%	34%	27%
NGC 3184	4%	31%	18%	6%	30%	21%	4%	20%	16%
NGC 3627	4%	35%	19%	7%	32%	24%	9%	25%	22%
NGC 5055	8%	42%	26%	5%	34%	21%	10%	40%	28%
NGC 5194	7%	37%	22%	4%	29%	19%	3%	21%	14%
NGC 6946	6%	40%	24%	3%	27%	16%	7%	31%	23%
Orion B							8%	18%	16%

and NGC 5194) the lowest cosmic ray ionization rate of $\zeta_{\text{CR}} = 10^{-18} \text{ s}^{-1}$ is required. The first two galaxies have particularly low gas surface densities below $20 M_{\odot} \text{ pc}^{-2}$. We can only speculate that these galaxies have a low magnetic field strength and a significant fraction of the ionizing cosmic ray particles escape from the galactic gas disk in the vertical direction. Energy equipartition between the cosmic ray particles and the magnetic field is commonly assumed in spiral galaxies (e.g., Beck & Krause 2005). Cosmic ray particles and magnetic fields are supposed to be strongly coupled and to exchange energy until equilibrium is reached. A lower magnetic field can thus confine fewer cosmic ray particles.

5.2. The CO conversion factor of NGC 6946

Bigiel et al. (2020) estimated the α_{CO} conversion factor based on [CII] and CO radial profiles of NGC 6946 using the Accurso et al. (2017) model. They obtained an increasing trend for α_{CO} with galactocentric radius, in broad agreement with the metallicity gradient. This behavior is consistent with prior observational works based on a combination of HI, CO, and infrared data involving the GDR (e.g., Sodroski et al. 1995; Braine et al. 1997; Sandstrom et al. 2013). Our radial profile of α_{CO} has approximately the same shape as that of Bigiel et al. (2020) but is about a factor of two higher. Sandstrom et al. (2013) determined the CO conversion factor via

$$\alpha_{\text{CO}} = \frac{1}{I_{\text{CO}}} (\text{GDR } \Sigma_{\text{D}} - \Sigma_{\text{HI}}), \quad (6)$$

simultaneously solving for α_{CO} and the GDR by assuming that the GDR is approximately constant on kiloparsec scales. With our inferred GDR of ~ 200 for NGC 6946 (see Table 5), the CO conversion factor of Sandstrom et al. (2013) would increase to a value close to the Galactic conversion factor. We conclude that our radial profile of the CO conversion factor is consistent within

a factor of two with that of Sandstrom et al. (2013) and independent of the GDR.

5.3. The effects of CO photodissociation in low-mass galaxies

In an externally irradiated gas cloud, a significant H_2 mass may lie outside the CO region, which is dark in CO in the outer regions of the cloud where the gas phase carbon resides in C or C^+ . In this region, H_2 self-shields or is shielded by dust from UV photodissociation, whereas CO is photo-dissociated. Following Wolfire et al. (2010), the dark gas mass fraction for a cloud of constant density is

$$f_{\text{DG}} = \frac{M_{\text{H}_2} - M_{\text{CO}}}{M_{\text{H}_2}} = 1 - \left(1 - \frac{2\Delta A_{\text{V,DG}}}{A_{\text{V}}}\right)^3, \quad (7)$$

with

$$\Delta A_{\text{V,DG}} = 0.53 - 0.045 \ln \left(\frac{\Sigma_{*}/(10^{-8} M_{\odot} \text{ pc}^{-2} \text{ yr}^{-1})}{n_{\text{cl}}} \right) - 0.097 \ln \left(\frac{Z}{Z_{\odot}} \right) \quad (8)$$

and $A_{\text{V}} = 2(Z/Z_{\odot})N_{\text{cl}}/(1.9 \times 10^{21} \text{ cm}^{-2})$, where N_{cl} is the H_2 column density. The mass fraction of CO-emitting gas is then

$$f_{\text{CO}} = f_{\text{H}_2} \left(1 - \frac{2\Delta A_{\text{V,DG}}}{A_{\text{V}}}\right)^3. \quad (9)$$

We tested the influence of the CO photodissociation on the observed CO brightness temperature for the low-mass galaxies where the effect is expected to be important (Fig. 10). In these galaxies we detected no significant effect. This is consistent with the fact that most of these galaxies are relatively CO-bright, meaning that CO emission is detected beyond $R \sim 2 R_d$. Even in

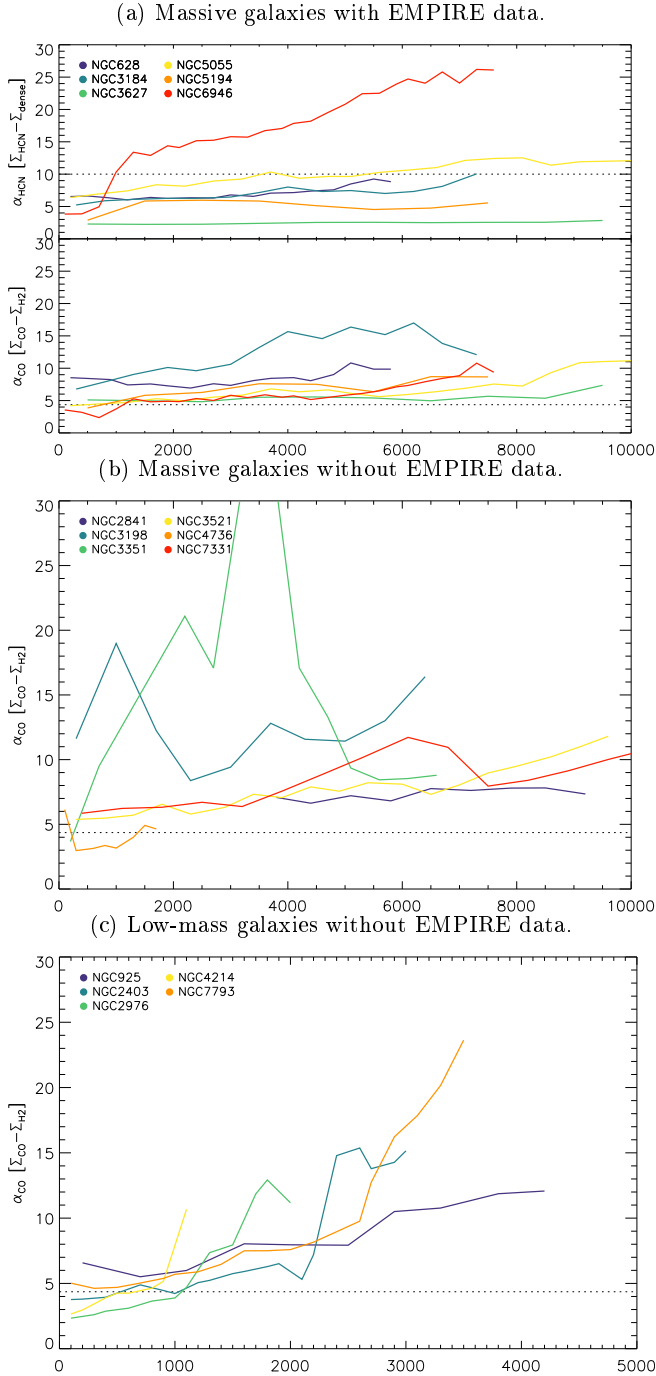


Fig. 8. CO-to-H₂ (α_{CO}) and HCN-to-dense gas (α_{HCN}) conversion factors of the high-mass galaxies with EMPIRE data (*upper panel*), high-mass galaxies without EMPIRE data (*middle panel*), and low-mass galaxies (*lower panel*; $M_* < 10^{10} M_\odot$). Dense gas corresponds to $n > 3 \times 10^4 \text{ cm}^{-3}$.

the CO-dim galaxy NGC 7793 CO photodissociation only leads to a decrease in the CO emission by $\sim 50\%$ in the inner disk and by a factor of about two in the outer disk. This translates into an increase in the CO flux by a factor of 1.7 in the absence of CO photodissociation.

5.4. Anomalous gas in NGC 2403

Vollmer & Leroy (2011) suggested that only low-mass galaxies ($M_* < 10^{10} M_\odot$) can sustain their SFR through radial accre-

Table 9. CO-weighted conversion factors.

Galaxy	Mean $\alpha_{\text{CO}}^{\text{Model}}$	Mean $\alpha_{\text{CO}}^{\text{Sandstrom}}$
NGC 628	6.4	5.1
NGC 3184	5.9	6.3
NGC 3627	5.5	1.8
NGC 5055	5.9	3.7
NGC 5194	5.7	–
NGC 6946	3.1	1.8
NGC 2841	9.0	5.7
NGC 3198	15.8	11.9
NGC 3351	6.7	2.9
NGC 3521	7.9	7.3
NGC 4736	5.4	1.1
NGC 7331	9.0	10.7
NGC 925	11.1	10.0
NGC 2403	8.9	–
NGC 2976	6.7	4.7
NGC 4214	5.5	–
NGC 7793	9.3	–

tion within the galactic disk. Within the framework of our model, this is only possible within $R \sim 2 R_d$ (Sect. 4.3.5 and Fig. 9). In order to sustain star formation through radial gas accretion within the thin gas disk, the gas mass has to be transported in a different way from large radii to $R \sim 2 R_d$. In NGC 2403, Fraternali et al. (2002a) found a faint extended and kinematically anomalous gas component. The cold HI disk is surrounded by a thick and clumpy HI layer characterized by slow rotation and infall motion ($10\text{--}20 \text{ km s}^{-1}$) toward the center. The gas surface density of the anomalous component is about $1 M_\odot \text{ pc}^{-2}$. The mass accretion rate is given by

$$\dot{M} = 2\pi\nu\Sigma = 2\pi R v_R \Sigma \sim 0.3 M_\odot \text{ yr}^{-1}, \quad (10)$$

where ν is the gas viscosity (Eq. (A.9)) and v_R the radial velocity (see also Fraternali et al. 2002b). This is exactly the radial mass accretion rate found by our model at $R \sim 2 R_d$ (Fig. B.13). Therefore, we suggest that the fuel for star formation reaches this radius from outside via a thick disk component. From $R \sim 2 R_d$ inward the gas is transported radially through turbulent gas viscosity, fully sustaining star formation. We can only speculate that a comparable mechanism acts in the other low-mass galaxies in our sample.

6. Conclusions

The Vollmer et al. (2017) model of a turbulent clumpy gas accretion disk was used to calculate the SFR, HI, CO(1–0), CO(2–1), HCN(1–0), and HCN⁺ radial profiles of a sample of 17 nearby spiral galaxies observed by the THINGS and HERACLES surveys. A subsample of six galaxies was observed by the EMPIRE survey. The large-scale properties of the model are the gas surface density, density, disk height, turbulent driving length scale, velocity dispersion, gas viscosity, volume filling factor, and molecular fraction. Small-scale properties are the mass, size, and density of clouds, the associated timescales (the crossing, the free-fall and the H₂ formation timescales) of the most massive self-gravitating gas clouds. These quantities depend on the stellar surface density, the angular velocity Ω , the disk radius R , and three free parameters, which are the Toomre parameter Q of the gas, the mass accretion rate \dot{M} , and the ratio δ between the

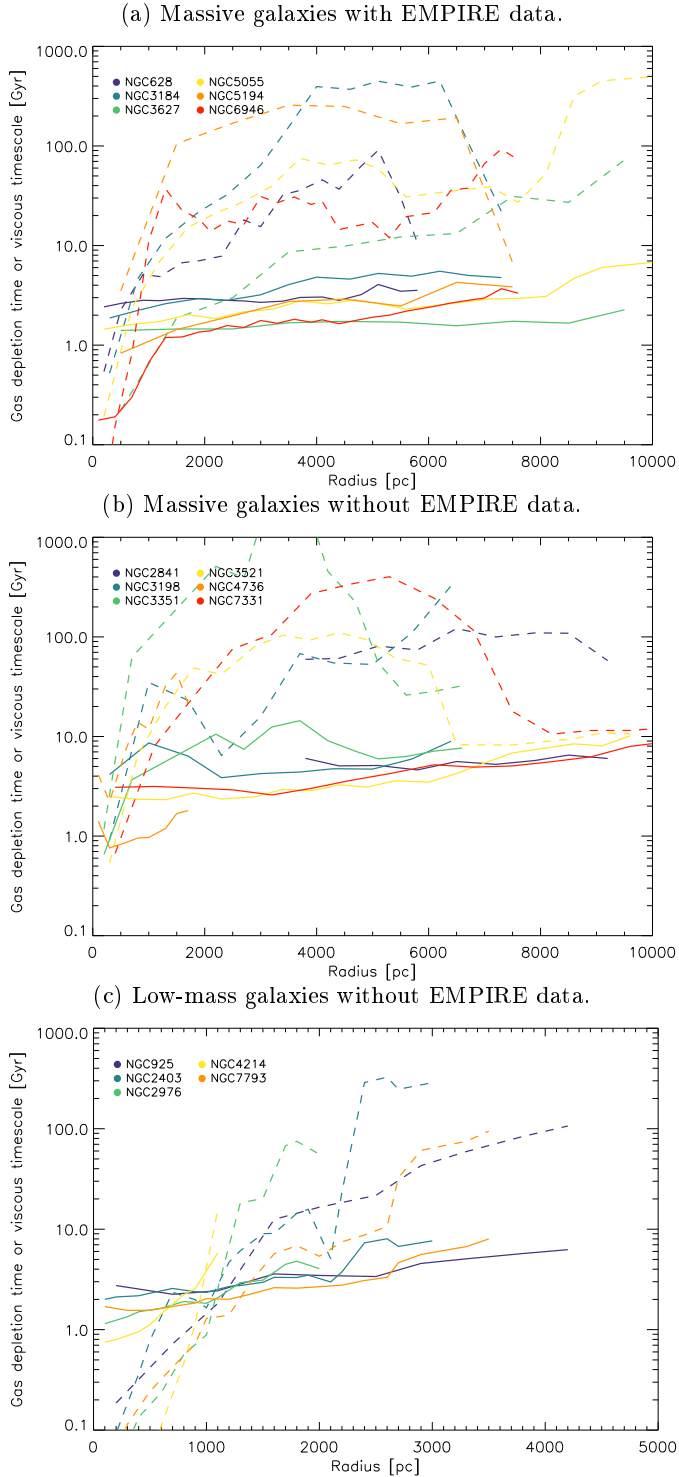


Fig. 9. Gas depletion (solid lines) and viscous timescale (dashed lines) of the high-mass galaxies with EMPIRE data (*upper panel*), high-mass galaxies without EMPIRE data (*middle panel*), and low-mass galaxies (*lower panel*; $M_* < 10^{10} M_\odot$).

driving length scale of turbulence and the cloud size. In addition, Galactic scaling laws for the dependence of the gas density and velocity dispersion on the cloud size were included in the model. The gas temperature was calculated through the equilibrium between turbulent mechanical heating and molecular line cooling. The molecular abundances were determined via NAU-

TILUS (Hersant et al. 2009) and the molecular line emission via RADEX (van der Tak et al. 2007).

For different values of δ we determined the free parameters Q and \dot{M} at each galactic radius using three independent measurements: the neutral gas (HI), molecular gas (CO), and SFR (FUV + $24\mu\text{m}$). We did not consider gas disks that are unstable to fragmentation ($Q < 1$). The model also yields the far-infrared radial profiles, which can be directly compared to *Herschel* data as a validation of our SFR recipe based on FUV and $24\mu\text{m}$ data. Furthermore, we determined the cosmic ray ionization rate by comparing the model HCN and $\text{HCO}^+(1-0)$ emission to EMPIRE observations (Jiménez-Donaire et al. 2019).

Based on the model fitting of the radial profiles of the total SFR, HI, CO, HCN, and HCO^+ , we conclude that:

1. The Toomre parameter Q_{tot} exceeds unity in the inner disk of a significant number of galaxies (Fig. 3). In two galaxies, Q_{tot} also exceeds unity in the outer disk. Thus, in spirals galaxies $Q_{\text{tot}} = 1$ is not ubiquitous.
2. The finite lifetime of molecular clouds ($f_{\text{mol}}^{\text{life}}$) has to be taken into account for the molecular gas fraction (Sect. 4.3.1).
3. The model gas velocity dispersions are consistent with the observed HI velocity dispersions (Fig. 4).
4. In all but one of the six galaxies observed by the EMPIRE survey, the model cosmic ray ionization rate is found to be significantly smaller than $\zeta_{\text{CR}} = 10^{-17} \text{ s}^{-1}$ (Table 6). For four out of six galaxies, we find $\zeta_{\text{CR}} = 10^{-18} \text{ s}^{-1}$.
5. Within our model, HCN and HCO^+ are already detectable in relatively low-density gas ($\sim 1000 \text{ cm}^{-3}$; Fig. 7). The model HCN(1-0) and $\text{HCO}^+(1-0)$ line emission traces densities of several 10^3 cm^{-3} (Table 7).
6. The derived CO conversion factor of most of the massive galaxies ($M_* > 10^{10} M_\odot$) is close to the Galactic value and increases slightly with galactic radius (Fig. 8).
7. In low-mass galaxies ($M_* < 10^{10} M_\odot$) the CO conversion factor can increase steeply with radius (Fig. 8).
8. The CO-dark gas mass is not relevant in the CO-bright low-mass galaxies (Fig. 10). In the CO-dim galaxy NGC 7793, the inclusion of CO photodissociation leads to CO emission that is lower by $\sim 50\%$ in the inner disk and $\sim 200\%$ in the outer disk.
9. The derived HCN conversion factors are consistent within a factor of two with the $\alpha_{\text{HCN}} = 10 M_\odot \text{ pc}^{-2} (\text{K km s}^{-1})^{-1}$ from Gao & Solomon (2004) and increase with galactic radius (Fig. 8).
10. In all galaxies the molecular gas depletion timescale ranges between 1 and 5 Gyr (Fig. 9).
11. In almost all massive galaxies the viscous timescale greatly exceeds the star-formation timescale (Fig. 9). In the absence of gas accretion from the galactic halo, the galaxies will undergo starvation (Larson et al. 1980), where the cold gas is exhausted by the star-formation activity of the galaxy. This naturally leads to $Q_{\text{tot}} > 1$.
12. In the low-mass galaxies the viscous timescale is smaller than the star-formation timescale for $R \lesssim 2R_d$. Thus, the SFR can be sustained by radial mass inflow within the galactic disk within $R \sim 2R_d$ (Fig. 9).
13. We suggest that the fuel for star formation reaches $R \sim 2R_d$ from the outskirts of the galaxy via a thick gas disk component as in NGC 2403 (Sect. 5.4).

The combination of the large-scale model of a turbulent clumpy star-forming galactic gas disk together with a local scaling relation based on Galactic observations is thus able to simultaneously reproduce SFR, infrared, HI, CO, HCN, and HCO^+ radial profiles of local spiral galaxies. The resulting gas velocity

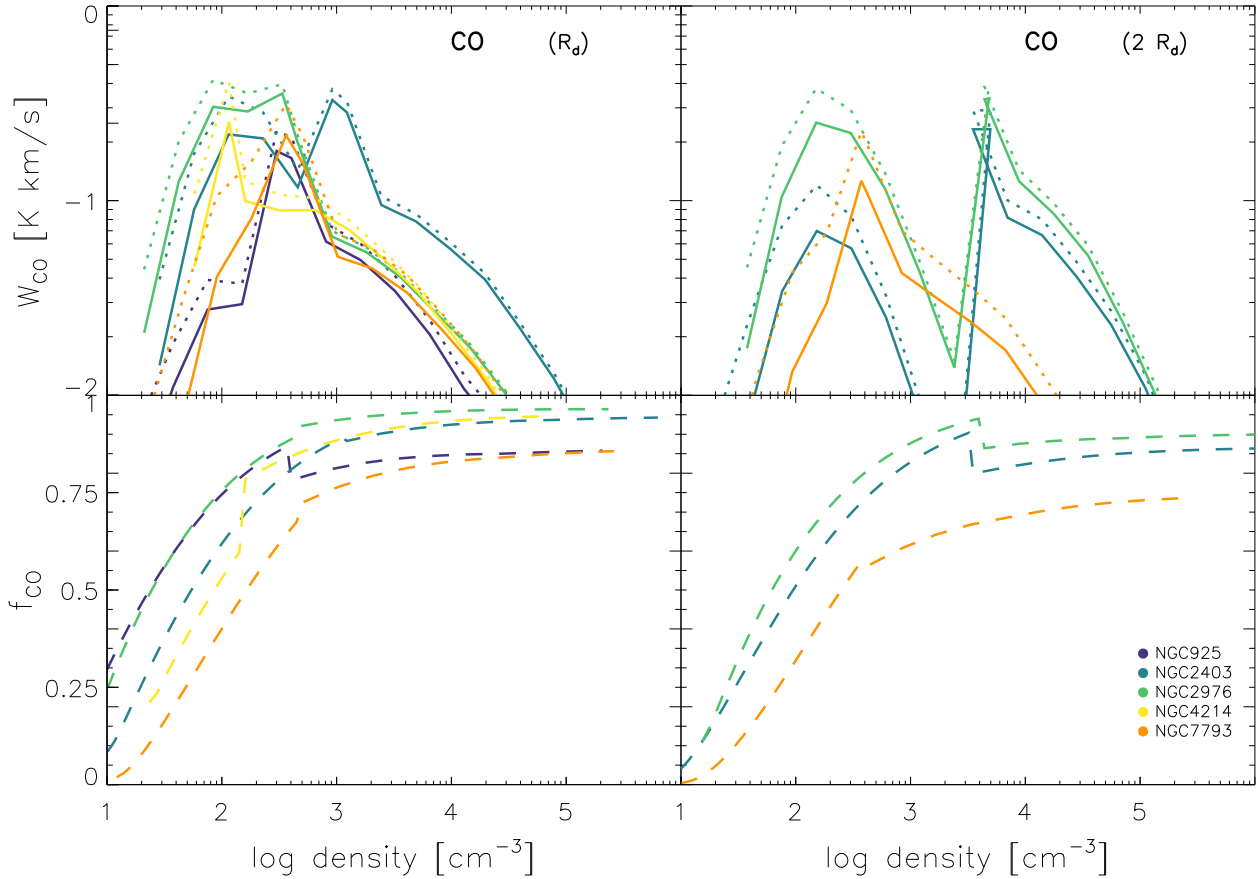


Fig. 10. Influence of the CO photo-dissociation in low-mass galaxies. *Upper panels:* integrated CO line intensity as a function of density for the four low-mass galaxies. Dotted lines indicate with photodissociation CO and solid lines without. *Lower panels:* mass fraction of CO-emitting gas as a function of density in the presence of CO photodissociation (Eq. (9)).

dispersions and CO and HCN conversion factors are in agreement with those found in the literature. As a potential next step, the model can be applied to high-resolution observations of ULIRGs and high- z star-forming galaxies.

Acknowledgements. We would like to thank Adam Leroy for his comments, which helped to improve the article and J. den Brok for making the PHANGS CO(2–1) radial profiles of NGC 3627 and NGC 5194 available to us. We also thank the anonymous referee for their useful comments, which helped to significantly improve the article.

References

- Accurso, G., Saintonge, A., Catinella, B., et al. 2017, *MNRAS*, **470**, 4750
- Battisti, A. J., & Heyer, M. H. 2014, *ApJ*, **780**, 173
- Beck, R., & Krause, M. 2005, *Astron. Nachr.*, **326**, 414
- Berg, D. A., Pogge, R. W., Skillman, E. D., et al. 2020, *ApJ*, **893**, 96
- Bešlić, I., Barnes, A. T., Bigiel, F., et al. 2021, *MNRAS*, **506**, 963
- Bigiel, F., Leroy, A., Walter, F., et al. 2008, *AJ*, **136**, 2846
- Bigiel, F., Leroy, A., & Walter, F. 2011, in *Computational Star Formation*, eds. J. Alves, B. G. Elmegreen, J. M. Girart, & V. Trimble, 270, 327
- Bigiel, F., de Looze, I., Krabbe, A., et al. 2020, *ApJ*, **903**, 30
- Boissier, S., Prantzos, N., Boselli, A., & Gavazzi, G. 2003, *MNRAS*, **346**, 1215
- Bolatto, A. D., Wolfire, M., & Leroy, A. K. 2013, *ARA&A*, **51**, 207
- Braine, J., Guélin, M., Dumke, M., et al. 1997, *A&A*, **326**, 963
- Caldú-Primo, A., Schruba, A., Walter, F., et al. 2013, *AJ*, **146**, 150
- da Cunha, E., Groves, B., Walter, F., et al. 2013, *ApJ*, **766**, 13
- Dale, D. A., Aniano, G., Engelbracht, C. W., et al. 2012, *ApJ*, **745**, 95
- Dalgarno, A. 2006, *Proc. Natl. Acad. Sci.*, **103**, 12269
- den Brok, J. S., Chatzigiannakis, D., Bigiel, F., et al. 2021, *MNRAS*, **504**, 3221
- Díaz, Á. I., Terlevich, E., Castellanos, M., & Hägele, G. F. 2007, *MNRAS*, **382**, 251
- Di Teodoro, E. M., & Peek, J. E. G. 2021, *ApJ*, **923**, 220
- Draine, B. T., & Bertoldi, F. 1996, *ApJ*, **468**, 269
- Draine, B. T., & Li, A. 2007, *ApJ*, **657**, 810
- Dumouchel, F., Faure, A., & Lique, F. 2010, *MNRAS*, **406**, 2488
- Ellison, S. L., Lin, L., Thorp, M. D., et al. 2021, *MNRAS*, **501**, 4777
- Elmegreen, B. G. 1989, *ApJ*, **338**, 178
- Elmegreen, B. G., & Scalo, J. 2004, *ARA&A*, **42**, 211
- Flower, D. R. 1999, *MNRAS*, **305**, 651
- Fraternali, F. 2017, in *Gas Accretion onto Galaxies*, eds. A. Fox, & R. Davé, *Astrophys. Space Sci. Lib.*, **430**, 323
- Fraternali, F., van Moorsel, G., Sancisi, R., & Oosterloo, T. 2002a, *AJ*, **123**, 3124
- Fraternali, F., Cappi, M., Sancisi, R., & Oosterloo, T. 2002b, *ApJ*, **578**, 109
- Gao, Y., & Solomon, P. M. 2004, *ApJ*, **606**, 271
- Gil de Paz, A., Boissier, S., Madore, B. F., et al. 2007, *ApJS*, **173**, 185
- Goldsmith, P. F. 2001, *ApJ*, **557**, 736
- Gordon, K. D., Roman-Duval, J., Bot, C., et al. 2014, *ApJ*, **797**, 85
- Green, S., & Thaddeus, P. 1976, *ApJ*, **205**, 766
- Heiderman, A., Evans, N. J., II, Allen, L. E., Huard, T., & Heyer, M. 2010, *ApJ*, **723**, 1019
- Hersant, F., Wakelam, V., Dutrey, A., Guilloteau, S., & Herbst, E. 2009, *A&A*, **493**, L49
- Heyer, M., Krawczyk, C., Duval, J., & Jackson, J. M. 2009, *ApJ*, **699**, 1092
- Hollenbach, D. J., & Tielens, A. G. G. M. 1997, *ARA&A*, **35**, 179
- Hunt, L. K., Draine, B. T., Bianchi, S., et al. 2015, *A&A*, **576**, A33
- Ianjamasimanana, R., de Blok, W. J. G., Walter, F., et al. 2015, *AJ*, **150**, 47
- Indriolo, N., & McCall, B. J. 2012, *ApJ*, **745**, 91
- Indriolo, N., Geballe, T. R., Oka, T., & McCall, B. J. 2007, *ApJ*, **671**, 1736
- Jiménez-Donaire, M. J., Bigiel, F., Leroy, A. K., et al. 2019, *ApJ*, **880**, 127
- Kauffmann, J., Goldsmith, P. F., Melnick, G., et al. 2017, *A&A*, **605**, L5
- Kennicutt, R. C., Jr. 1998a, *ApJ*, **498**, 541
- Kennicutt, R. C., Jr. 1998b, *ARA&A*, **36**, 189
- Kennicutt, R. C., Jr., Armus, L., Bendo, G., et al. 2003, *PASP*, **115**, 928
- Kreckel, K., Ho, I. T., Blanc, G. A., et al. 2019, *ApJ*, **887**, 80
- Kregel, M., van der Kruit, P. C., de Blok, W. J. G., & Freeman, K. C. 2002, in *Disks of Galaxies: Kinematics, Dynamics and Perturbations*, eds. E. Athanassoula, A. Bosma, & R. Mujica, *ASP Conf. Ser.*, **275**, 47

- Kruijssen, J. M. D., & Longmore, S. N. 2014, *MNRAS*, **439**, 3239
- Krumholz, M. R., & Burkhardt, B. 2016, *MNRAS*, **458**, 1671
- Krumholz, M. R., McKee, C. F., & Tumlinson, J. 2008, *ApJ*, **689**, 865
- Krumholz, M. R., McKee, C. F., & Tumlinson, J. 2009, *ApJ*, **693**, 216
- Krumholz, M. R., Dekel, A., & McKee, C. F. 2012, *ApJ*, **745**, 69
- Larson, R. B. 1979, *MNRAS*, **186**, 479
- Larson, R. B. 1981, *MNRAS*, **194**, 809
- Larson, R. B., Tinsley, B. M., & Caldwell, C. N. 1980, *ApJ*, **237**, 692
- Leroy, A. K., Walter, F., Brinks, E., et al. 2008, *AJ*, **136**, 2782
- Leroy, A. K., Walter, F., Bigiel, F., et al. 2009, *AJ*, **137**, 4670
- Leroy, A. K., Usero, A., Schrubba, A., et al. 2017, *ApJ*, **835**, 217
- Leroy, A. K., Hughes, A., Liu, D., et al. 2021, *ApJS*, **255**, 19
- Li, A., & Draine, B. T. 2001, *ApJ*, **554**, 778
- Licquia, T. C., & Newman, J. A. 2015, *ApJ*, **806**, 96
- Liszt, H. S., & Pety, J. 2016, *ApJ*, **823**, 124
- Lizée, T., Vollmer, B., Braine, J., & Nehlig, F. 2021, *A&A*, **645**, A111
- Lombardi, M., Alves, J., & Lada, C. J. 2010, *A&A*, **519**, L7
- Mac Low, M.-M., & Klessen, R. S. 2004, *Rev. Mod. Phys.*, **76**, 125
- Mangum, J. G., & Shirley, Y. L. 2015, *PASP*, **127**, 266
- Moustakas, J., Kennicutt, R. C., Jr., Tremonti, C. A., et al. 2010, *ApJS*, **190**, 233
- Neufeld, D. A., & Wolfire, M. G. 2017, *ApJ*, **845**, 163
- Onus, A., Krumholz, M. R., & Federrath, C. 2018, *MNRAS*, **479**, 1702
- Padoan, P., Nordlund, A., & Jones, B. J. T. 1997, *MNRAS*, **288**, 145
- Padovani, M., Galli, D., & Glassgold, A. E. 2009, *A&A*, **501**, 619
- Pety, J., Guzmán, V. V., Orkisz, J. H., et al. 2017, *A&A*, **599**, A98
- Quiroga, R. J. 1983, *Ap&SS*, **93**, 37
- Retes-Romero, R., Mayya, Y. D., Luna, A., & Carrasco, L. 2017, *ApJ*, **839**, 113
- Rozwadowska, K., Vissani, F., & Cappellaro, E. 2021, *New Astron.*, **83**, 101498
- Sandstrom, K. M., Leroy, A. K., Walter, F., et al. 2013, *ApJ*, **777**, 5
- Schinnerer, E., Hughes, A., Leroy, A., et al. 2019, *ApJ*, **887**, 49
- Schmidt, M. 1959, *ApJ*, **129**, 243
- Schmidt, T. M., Bigiel, F., Klessen, R. S., & de Blok, W. J. G. 2016, *MNRAS*, **457**, 2642
- Schoeier, F. L., van der Tak, F. F. S., van Dishoeck, E. F., & Black, J. H. 2005, *VizieR Online Data Catalog: J/A+A/432/369*
- Sodroski, T. J., Odegard, N., Dwek, E., et al. 1995, *ApJ*, **452**, 262
- Solomon, P. M., Rivolo, A. R., Barrett, J., & Yahil, A. 1987, *ApJ*, **319**, 730
- Spitzer, L., Jr., & Tomasko, M. G. 1968, *ApJ*, **152**, 971
- Stanghellini, L., Magrini, L., & Casasola, V. 2015, *ApJ*, **812**, 39
- Tamburro, D., Rix, H. W., Leroy, A. K., et al. 2009, *AJ*, **137**, 4424
- Teng, Y.-H., Sandstrom, K. M., Sun, J., et al. 2022, *ApJ*, **925**, 72
- Thornton, K., Gaudlitz, M., Janka, H. T., & Steinmetz, M. 1998, *ApJ*, **500**, 95
- Toomre, A. 1964, *ApJ*, **139**, 1217
- Utomo, D., Sun, J., Leroy, A. K., et al. 2018, *ApJ*, **861**, L18
- van der Tak, F. F. S., Black, J. H., Schöier, F. L., Jansen, D. J., & van Dishoeck, E. F. 2007, *A&A*, **468**, 627
- van Dishoeck, E. F., & Black, J. H. 1986, *ApJS*, **62**, 109
- Vollmer, B., & Beckert, T. 2003, *A&A*, **404**, 21
- Vollmer, B., & Leroy, A. K. 2011, *AJ*, **141**, 24
- Vollmer, B., Gratier, P., Braine, J., & Bot, C. 2017, *A&A*, **602**, A51
- Vollmer, B., Fossati, M., Boselli, A., et al. 2021, *A&A*, **645**, A121
- Walter, F., Brinks, E., de Blok, W. J. G., et al. 2008, *AJ*, **136**, 2563
- Weingartner, J. C., & Draine, B. T. 2001, *ApJ*, **548**, 296
- Wolfire, M. G., McKee, C. F., Hollenbach, D., & Tielens, A. G. G. M. 2003, *ApJ*, **587**, 278
- Wolfire, M. G., Hollenbach, D., & McKee, C. F. 2010, *ApJ*, **716**, 1191
- Wu, J., Evans, N. J., II, Shirley, Y. L., & Knez, C. 2010, *ApJS*, **188**, 313
- Yang, B., Stancil, P. C., Balakrishnan, N., & Forrey, R. C. 2010, *ApJ*, **718**, 1062
- Zubko, V., Dwek, E., & Arendt, R. G. 2004, *ApJS*, **152**, 211

Appendix A: Detailed description of the model

The analytical model of a turbulent clumpy star-forming galactic disk has a large-scale and a small-scale part.

A.1. Large-scale part

In this subsection we describe in detail the physics that govern the large-scale part of the model.

A.1.1. Hydrostatic equilibrium

Within the model the ISM is considered as a single turbulent gas in vertical hydrostatic equilibrium. The turbulent pressure is defined as $P_{\text{turb}} = \rho\sigma_{\text{disp}}^2$, where σ_{disp} is the total velocity dispersion that takes into account both, the velocity dispersion caused by turbulence v_{turb} and a constant thermal velocity $v_{\text{therm}} = c_s = 6 \text{ km s}^{-1}$ such as $\sigma_{\text{disp}} = \sqrt{v_{\text{turb}}^2 + c_s^2}$. Following Elmegreen (1989), we can establish the first main equation of the model:

$$P_{\text{turb}} = \rho\sigma_{\text{disp}}^2 = \frac{\pi}{2}G\Sigma\left(\Sigma + \Sigma_{\star}\frac{\sigma_{\text{disp}}}{\gamma\sigma_{\text{disp}}^{\star}}\right), \quad (\text{A.1})$$

where ρ is the midplane density, Σ is the total gas surface density, Σ_{\star} is the stellar surface density, $\sigma_{\text{disp}}^{\star}$ is the vertical stellar velocity dispersion, and γ is a fudge factor. Given the stellar surface density and the stellar length scale of the disk l_{\star} , the vertical stellar velocity dispersion can be computed following Kregel et al. (2002):

$$\sigma_{\text{disp}}^{\star} = \sqrt{2\pi G\Sigma_{\star}\frac{l_{\star}}{7.3}}. \quad (\text{A.2})$$

A.1.2. Energy transfer by turbulence

In galaxies ISM turbulence is mainly maintained by stellar feedback such as SN explosions, ionizing radiation, or stellar winds (Mac Low & Klessen 2004; Elmegreen & Scalo 2004). Within the framework of our model we consider SN explosions as the dominant source of energy. Turbulence is expected to form eddies with a typical size l_{driv} (the turbulent driving length scale) at the origin of the formation of the densest gas clouds. The SNe energy is cascaded from the largest to the smallest scales. The energy per unit time, which is carried by turbulence, is

$$\dot{E} \simeq -\dot{E}_{\text{SN}} = -\frac{\rho\nu}{2} \int \frac{v_{\text{turb},3\text{D}}^2}{l_{\text{driv}}^2} dV, \quad (\text{A.3})$$

where ν is the viscosity of the gas defined as $\nu = v_{\text{turb},3\text{D}}l_{\text{driv}}$ with the 3D turbulent velocity dispersion $v_{\text{turb},3\text{D}} = \sqrt{3}v_{\text{turb}}$. If we define the surface density of the gas as $\Sigma = \rho H$ and assume the integration over the volume $\int dV = V = AH$, we can connect the energy input into the ISM by SNe directly to the SFR with the assumption of a constant initial mass function as

$$\frac{\dot{E}_{\text{SN}}}{\Delta A} = \frac{\Sigma\nu}{2} \frac{v_{\text{turb},3\text{D}}^2}{l_{\text{driv}}^2} = \xi\dot{\Sigma}_{\star}, \quad (\text{A.4})$$

where \dot{E}_{SN} is the energy injected by the SN explosions, ΔA is the unit area, and $\dot{\Sigma}_{\star}$ is the SFR. The factor ξ relates the energy injection by SN explosions to the SFR. It is considered as constant and its canonical value was estimated from observations in

the Milky Way, given $\xi = 4.6 \times 10^{-8} \text{ pc}^2/\text{yr}^2$ (Vollmer & Beckert 2003). In the presence of high disk mass accretion rates, the energy injection through the gain of potential energy can be important. In this case, Eq. A.4 becomes

$$\frac{\Sigma\nu}{2} \frac{v_{\text{turb},3\text{D}}^2}{l_{\text{driv}}^2} = \xi\dot{\Sigma}_{\star} + \frac{1}{2\pi}\dot{M}\Omega^2, \quad (\text{A.5})$$

where \dot{M} is the mass accretion rate and Ω is the angular velocity.

A.1.3. Viscosity and accretion

The model is based on the assumption that turbulence redistributes the angular momentum within the disk via gas viscosity. The galactic gas disk is treated as a turbulent clumpy accretion disk, where angular momentum is transported outward, permitting the gas to move inward. Assuming a continuous and nonzero external gas mass accretion $\dot{\Sigma}_{\text{ext}}$, the simplified time evolution of the disk surface density is given by

$$\frac{\partial\Sigma}{\partial t} \sim \frac{\nu\Sigma}{R^2} - \dot{\Sigma}_{\star} + \dot{\Sigma}_{\text{ext}}. \quad (\text{A.6})$$

The mass accretion rate within the disk is

$$\dot{M} = -2\pi R\Sigma v_{\text{rot}} = \frac{1}{v_{\text{rot}}}\frac{\partial}{\partial R}\left(2\pi\Sigma R^3\frac{d\Omega}{dR}\right). \quad (\text{A.7})$$

With the approximation $\partial/\partial R \sim R$ and $v_{\text{rot}} = \Omega R$, one obtains

$$\nu\Sigma = -\frac{\dot{M}}{2\pi R}\Omega\left(\frac{d\Omega}{dR}\right)^{-1}, \quad (\text{A.8})$$

where the viscosity of the gas ν is defined as

$$\nu = \sqrt{3}v_{\text{turb}}l_{\text{driv}}. \quad (\text{A.9})$$

Contrary to Vollmer & Leroy (2011), where it was assumed that $\dot{\Sigma}_{\text{ext}} = \dot{\Sigma}_{\star}$ and thus $\partial\Omega/\partial t = 0$, and $\dot{M} = cte$, the mass accretion derived from the observational radial profiles varies with radius. We are mostly interested in the viscous timescale $t_{\text{vis}} \sim R^2/\nu$ (see Sect. 4.1).

A.1.4. Self-gravitating clouds and star-formation

The clumpiness of the model gas disk implies that the density of a single gas cloud ρ_{cl} depends directly on the average density of the disk ρ . In the model, these two quantities are linked by the volume filling factor ϕ_v , such that $\rho_{\text{cl}} = \phi_v^{-1}\rho$. Following Vollmer & Leroy (2011) and Vollmer et al. (2021), the SFR per unit volume is given by

$$\dot{\rho}_{\star} = \phi_v\rho_{\text{ff,cl}}^{-1}. \quad (\text{A.10})$$

For self-gravitating clouds with a virial parameter of unity, the turbulent crossing time $t_{\text{turb,cl}}$ equals twice the free-fall time $t_{\text{ff,cl}}$ (Vollmer et al. 2021):

$$t_{\text{turb,cl}} = \frac{\sqrt{3}}{2}\frac{l_{\text{cl}}}{v_{\text{turb,cl}}} = 2t_{\text{ff,cl}} = \sqrt{\frac{3\pi\phi_v}{32G\rho}}, \quad (\text{A.11})$$

where l_{cl} and $v_{\text{turb,cl}}$ are the size and the turbulent 3D velocity dispersion of a single gas cloud, respectively. Following Larson's

law (Larson 1981), we can simplify the expression of the turbulent crossing time:

$$\frac{\sqrt{3}}{2} \frac{l_{\text{cl}}}{v_{\text{turb,cl}}} = \frac{\sqrt{3}}{2} \frac{l_{\text{driv}}}{v_{\text{turb}} \sqrt{\delta}}, \quad (\text{A.12})$$

where δ is the scaling between the driving length scale and the size of the largest self-gravitating structures, such as $\delta = l_{\text{driv}}/l_{\text{cl}}$. All these considerations lead us to the second expression of the SFR in the model:

$$\dot{\rho}_{\star} = \frac{4\sqrt{\delta}}{\sqrt{3}} \phi_{\text{v}} \rho \frac{v_{\text{turb}}}{l_{\text{driv}}} \quad (\text{A.13})$$

and $\dot{\Sigma}_{\star} = \dot{\rho}_{\star} l_{\text{driv}}$. This SFR recipe is close to the prescription suggested by Krumholz et al. (2012):

$$\dot{\Sigma}_{\star} = f_{\text{H}_2} \epsilon_{\text{ff}} \frac{\Sigma}{t_{\text{ff}}}, \quad (\text{A.14})$$

where ϵ_{ff} is the star-formation efficiency per free-fall time. The relevant size scale for the density entering t_{ff} is that corresponding to the outer scale of the turbulence that regulates the SFR, which corresponds to l_{driv} in our model. For a consistency check we directly compared the two SFR prescriptions and found that both have comparable slopes and normalizations (Fig. A.1).

We calculated the star-formation efficiency per free-fall time by injecting our model SFR into Eq. A.14 for each galaxy and found $\langle \epsilon_{\text{ff}} \rangle = 0.8\%$ for our sample, which is consistent with the values measured by Utomo et al. (2018) and Jiménez-Donaire et al. (2019).

A.1.5. Metallicity

One of the main assumptions of the model is that molecular clouds are relatively short-lived, appearing and disappearing in a cloud crossing time. They might not reach chemical equilibrium within their lifetime, which is about the free-fall time. We defined the characteristic time of H_2 formation as

$$\tau_{\text{mol}} = \frac{\alpha}{\rho_{\text{cl}}}, \quad (\text{A.15})$$

where α is the constant of molecule formation that depends on the gas metallicity and temperature (Draine & Bertoldi 1996). The metallicity of the model is estimated using a leaky box model with an effective yield based on the gas fraction

$$\alpha = \alpha_0 \times \left(\ln \left(\frac{\Sigma_{\star} + \Sigma}{\Sigma} \right) \right)^{-1}, \quad (\text{A.16})$$

where $\alpha_0 = 3.6 \times 10^7 \text{ yr } M_{\odot} \text{ pc}^{-3}$. The relation between the metallicity and the constant of molecule formation is the following:

$$\frac{Z}{Z_{\odot}} = \frac{\alpha_{\odot}}{\alpha}, \quad (\text{A.17})$$

where $\alpha_{\odot} = 2.2 \times 10^7 \text{ yr } M_{\odot} \text{ pc}^{-3}$ (Hollenbach & Tielens 1997). The metallicity can be linked to the effective yield y_{eff} defined as $y_{\text{eff}} = Z/\ln(1/f_{\text{gas}})$, where f_{gas} is the gas fraction. Vollmer & Leroy (2011) showed that these metallicities are consistent with those measured by Moustakas et al. (2010).

A.1.6. Gas fragmentation and Toomre parameter Q

One of the main parameters of the model is the Toomre parameter Q (Toomre 1964). It describes the stability of the gas disk regarding radial gas fragmentation:

$$Q = \frac{\sigma_{\text{disp}}^{\kappa}}{\pi G \Sigma}, \quad (\text{A.18})$$

where κ is the epicyclic frequency,

$$\kappa = \sqrt{4\Omega^2 + R \frac{d\Omega^2}{dR}}. \quad (\text{A.19})$$

The Toomre Q parameter is also used as a measure of the gas content of the disk, with $Q = 1$ for the maximum disk gas mass.

A.2. Small-scale part

In this subsection the physics that govern the small-scale part of the model are described. This involves scaling relations for the density and velocity dispersion of the gas clouds.

A.2.1. Mass fraction

The small-scale part is divided into two distinct subscales, non-self-gravitating and self-gravitating gas clouds of density ρ_{cl} . For each density, the mass fraction of the gas is determined by a lognormal probability distribution function (Padoan et al. 1997):

$$p(x)dx = \frac{1}{x\sqrt{2\pi\sigma^2}} \exp\left(-\frac{(\ln x + \sigma^2/2)^2}{2\sigma^2}\right) dx, \quad (\text{A.20})$$

where $x = \rho_{\text{cl}}/\rho$ is the overdensity and the standard deviation σ is determined by the Mach number \mathcal{M} :

$$\sigma^2 \simeq \ln\left(1 + (\mathcal{M}/2)^2\right). \quad (\text{A.21})$$

The mass fraction of gas with overdensities exceeding x is thus defined as

$$\frac{\Delta M}{M} = \frac{1}{2} \left(1 + \text{erf} \left(\frac{\sigma^2 - 2 \ln x}{2^{3/2} \sigma} \right) \right). \quad (\text{A.22})$$

Based on the results of Battisti & Heyer (2014), who found that the fraction of the GMC mass residing within regions with densities higher than $n \sim 10^3 \text{ cm}^{-3}$ is about 10%, and following Pety et al. (2017), the mass fraction of self-gravitating cloud was decreased by a constant factor of 0.6. The inclusion of this factor was necessary to fit the observed integrated CO, HCN and HCO^+ line fluxes (Vollmer et al. 2017).

A.2.2. ISM scaling relations

We assumed different scaling relations for the two density regimes: (i) for non-self-gravitating clouds, we adopted the scaling relations found for galactic HI by Quiroga (1983): $\rho_{\text{cl}} \propto l^{-2}$, $v_{\text{turb,cl}} \propto l^{1/3}$, and thus $v_{\text{turb,cl}} = v_{\text{turb}}(\rho_{\text{cl}}/\rho)^{-1/6}$, where v_{turb} and ρ are the turbulent velocity and the density of the disk, respectively. Since the minimum density considered in this work is $\sim 100 \text{ cm}^{-2}$, the maximum turbulent velocity of diffuse clouds is $\sim v_{\text{turb}}/2 \sim 5 \text{ km s}^{-1}$. (ii) For self-gravitating clouds, we adopt the scaling relations of Lombardi et al. (2010): $\rho_{\text{cl}} \propto l^{-1.4}$, $v_{\text{turb,cl}} \propto l^{1/2}$. As described in Sect. A.1.4, the scale of the largest self-gravitating clouds l_{cl} is smaller than the turbulent driving

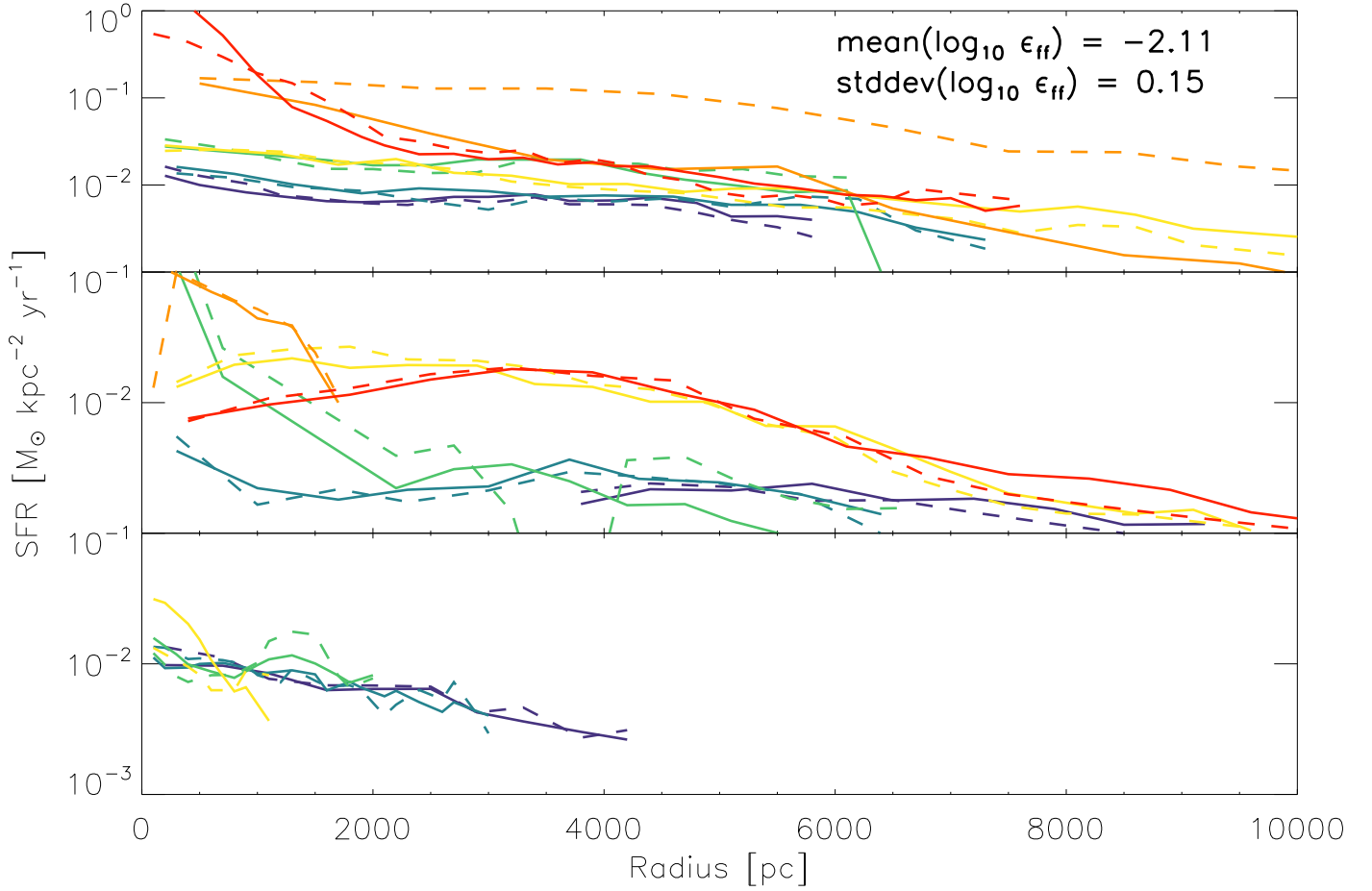


Fig. A.1. Star-formation rate per unit area as a function of galactic radius. Upper panel: Massive galaxies with EMPIRE data. Middle panel: Massive galaxies without EMPIRE data. Lower panel: Low-mass galaxies. Solid lines show our model SFR prescription (Eq. A.13) and dashed lines Krumholz et al. 2012 SFR prescription (Eq. A.14).

length scale l_{driv} by a factor $\delta = l_{\text{driv}}/l_{\text{cl}}$. We assume that the turbulent velocity dispersion of the largest self-gravitating clouds of density ρ_{sg} is $v_{\text{turb,cl}} = v_{\text{turb}}/\sqrt{\delta}$, where v_{turb} is the velocity dispersion of the disk. Furthermore, we assume $\rho_{\text{cl}} \propto l^{-1}$ and $v_{\text{turb,cl}} = v_{\text{turb}}/\sqrt{\delta(\rho_{\text{cl}}/\rho_{\text{sg}})^{-1/2}} \propto l^{1/2}$ (Solomon et al. 1987).

A.2.3. Molecule abundances from chemical network

For the determination of the H₂ column density of a gas cloud, we take into account (i) the photodissociation of H₂ molecules and (ii) the influence of the finite cloud lifetime on the H₂ formation. For the photodissociation of H₂ molecules, we follow the approach of Krumholz et al. (2008) and Krumholz et al. (2009). In a second step, we take into account the molecular fraction due to the finite lifetime of the gas cloud,

$$f_{\text{mol}}^{\text{life}} = t_{\text{ff}}^{\text{cl}}/t_{\text{mol}}^{\text{cl}}/(1 + t_{\text{ff}}^{\text{cl}}/t_{\text{mol}}^{\text{cl}}). \quad (\text{A.23})$$

If the H₂ formation timescale t_{mol} is longer than the free-fall timescale, the gas cloud will be mainly atomic during its lifetime. The inclusion of the cloud lifetime decreases the molecular gas surface density and thus the CO emission in the outer disks. The best fit to the CO data then leads to a lower Q and/or \dot{M} resulting in a lower gas velocity dispersion compared to the model without the inclusion of the cloud lifetime. The total molecular fraction of a cloud is $f_{\text{mol}} = f_{\text{mol}}^{\text{life}} \times f_{\text{mol}}^{\text{diss}}$. The molecular

fraction due to the finite lifetime $f_{\text{mol}}^{\text{life}}$ has the highest influence on f_{mol} at large galactic radii.

The abundances of the different molecules are determined using the gas-grain code NAUTILUS presented in Hersant et al. (2009). This code computes the abundances of chemical species as a function of time by solving the rate equations for a network of reactions. The input parameters are the crossing time, density, gas temperature, UV flux, cosmic ray ionization rate, and the initial elemental abundances of the model gas clouds. We assume a UV flux that is proportional to the large-scale SFR and a constant cosmic ray ionization rate. The gas temperature of the clouds is calculated by the equilibrium between gas heating and cooling (Sect. A.2.4).

A.2.4. Heating and cooling mechanisms

Gas heating is provided via two distinct mechanisms: (i) turbulent mechanical heating and (ii) radiation heating via cosmic rays ionization. The main mechanisms for gas cooling are CO and H₂ line emission.

The thermal balance of gas and dust is determined by gas-dust collisions in the model. To determine this balance, we simultaneously solved the following equations:

$$\Gamma_{\text{g}} - \Lambda_{\text{g}} - \Lambda_{\text{gd}} = 0 \quad (\text{A.24})$$

and

$$\Gamma_{\text{d}} - \Lambda_{\text{d}} + \Lambda_{\text{gd}} = 0, \quad (\text{A.25})$$

where Λ_d is the dust cooling rate, Λ_g corresponds to the molecular line cooling, Γ_d is the radiative heating of dust grains, Γ_g the heating via turbulence and cosmic rays, and Λ_{gd} the dust cooling energy transfer between dust and gas due to collisions.

A.2.5. Brightness temperatures and molecular line emission

The molecular line emission is computed using the brightness temperature formalism. The difference in brightness temperature between on- and off- positions is given by

$$\Delta T_A^* = (1 - e^{-\tau}) \frac{h\nu}{k} \left(\frac{1}{e^{h\nu/kT_{\text{ex}}} - 1} - \frac{1}{e^{h\nu/kT_{\text{bg}}} - 1} \right), \quad (\text{A.26})$$

where τ is the optical depth of the line, ν the frequency of the observations, h and k the Planck and Boltzmann constants, and T_{ex} and T_{bg} the excitation and background brightness temperatures.

For simplicity only a single collider (H_2) is considered. The excitation temperature is

$$\frac{1}{T_{\text{ex}}} = \left(\frac{1}{T_g} + \left(\frac{A_{ul}}{nq_{ul}} \frac{T_{\text{bg}}}{T_*} \right) \frac{1}{T_{\text{bg}}} \right) / \left(1 + \frac{A_{ul}}{nq_{ul}} \frac{T_{\text{bg}}}{T_*} \right), \quad (\text{A.27})$$

where $T_* = h\nu_{ul}/k$, n is the gas density, nq_{ul} the collisional de-excitation rate, and A_{ul} the Einstein coefficients of the transition ul . The background brightness temperature T_{bg} is the sum of the effective emission temperatures of the galaxy's dust $T_{\text{eff,dust}}$ and the cosmic background at the galaxy redshift T_{CMB} (see Eq. (17) of [da Cunha et al. 2013](#)). For optically thin transitions, the ratio of the radiative and collisional rates is the ratio of the density to the critical density for a given transition:

$$n_{\text{crit}} = \frac{A_{ul}}{q_{ul}}. \quad (\text{A.28})$$

We consider two-level molecular systems, in which the level populations are determined by a balance of collisions with H_2 , spontaneous decay and line photon absorption, and stimulated emission with $\tau > 1$. The molecular abundances were calculated by NAUTILUS (see Sect. A.2.3). For simplicity, we neglected the hyperfine structure of HCN.

The rotation constants, Einstein coefficients, and collision rates were taken from the Leiden Atomic and Molecular Database (LAMDA; [Schoeier et al. 2005](#)). The CO collision rates were provided by [Yang et al. \(2010\)](#). The HCN collision rates were taken from the He–HCN rate coefficients calculated by [Dumouchel et al. \(2010\)](#), scaled by a factor of 1.36 to go to HCN– H_2 (see [Green & Thaddeus 1976](#)). The HCO^+ collision rates were taken from [Flower \(1999\)](#).

We compared the brightness temperatures obtained by our approximate recipe to those calculated with the statistical equilibrium radiative transfer code RADEX from [van der Tak et al. \(2007\)](#). RADEX is a 1D nonlocal thermodynamic equilibrium radiative transfer code that uses the escape probability formulation assuming an isothermal and homogeneous medium without large-scale velocity fields. We systematically specify when the results presented were obtained using RADEX.

The integrated line emission, in K km s^{-1} , is computed using the following expression:

$$W = 2.35 \sum_{i=1}^N (\Delta T_A^*)_i (\phi_A)_i (v_{\text{turb,cl}})_i \left(\frac{\Delta M}{M} \right)_i, \quad (\text{A.29})$$

where T_A^* is the brightness temperature, ϕ_A is the surface filling factor, $\frac{\Delta M}{M}$ is the mass fraction as defined in Eq. A.22, and $v_{\text{turb,cl}}$ is the turbulent velocity of the cloud at a given density. The factor 2.35 links the turbulent velocity to the linewidth. CO photodissociation is taken into account following [Wolfire et al. \(2010\)](#).

A.2.6. Interstellar radiation field and cosmic ray ionization

The stellar radiation field is set by the SFR (Sect. 2.4) and stellar mass radial profiles Σ_* :

$$\frac{F}{F_0} = k \times \left(\frac{\Sigma_*}{10^{-8} M_\odot \text{pc}^{-2} \text{yr}^{-1}} + \frac{\Sigma_*}{40 M_\odot \text{pc}^{-2}} \right), \quad (\text{A.30})$$

where $F_0 = 5.3 \times 10^{-3} \text{ ergs cm}^{-2} \text{ s}^{-1}$ ([Goldsmith 2001](#)). The constant cosmic ray ionization rate is constrained by the observed $\text{HCO}^+(1-0)$ emission. In practice, we calculated models with different ionization rates and chose the value that yielded the best fit to the $\text{HCO}^+(1-0)$ radial profile.

A.2.7. Thermal dust emission

The dust temperature T_d of a gas cloud of a given density and size illuminated by a local mean radiation field is calculated by solving Eq. A.25. With the dust mass absorption coefficient of $\kappa(\lambda) = \kappa_0(\lambda_0/\lambda)^\beta$, the dust optical depth is

$$\tau(\lambda) = \kappa(\lambda) \Sigma_{\text{cl}} (\text{GDR})^{-1}, \quad (\text{A.31})$$

where Σ_{cl} is the cloud surface density in g/cm^2 . We used $\kappa_0(250 \mu\text{m}) = 4.8 \text{ cm}^2 \text{ g}^{-1}$ ([Li & Draine 2001](#); [Dale et al. 2012](#)) and $\beta = 1.5$. The absorption coefficient at $160 \mu\text{m}$ is $\kappa_0(160 \mu\text{m}) = 9.4 \text{ cm}^2 \text{ g}^{-1}$. This value is consistent with but at the lower end of the range found in the literature $\kappa_0(160 \mu\text{m}) = 10 - 15 \text{ cm}^2 \text{ g}^{-1}$ ([Weingartner & Draine 2001](#); [Zubko et al. 2004](#); [Draine & Li 2007](#); [Gordon et al. 2014](#)).

The infrared emission at a given wavelength at a given galactic radius R is calculated in the following way:

$$I_{\text{dust}}(\lambda) = \sum_{i=1}^N (\Phi_A)_i \left(\frac{\Delta M}{M} \right)_i (1 - \exp(-\tau(\lambda)))_i B(\lambda, T_d)_i, \quad (\text{A.32})$$

where $B(\lambda, T_d)$ is the Planck function and $\Phi_A = 1.5 (\Delta M/M) (\Sigma/\Sigma_{\text{cl}})$ the area filling factor. The factor 1.5 takes into account that the mean cloud surface density is 1.5 times lower than the surface density in the cloud center $\Sigma_{\text{cl}} = \rho_{\text{cl}} l_{\text{cl}}$.

Appendix B: Best-fit models

The model and observed HI, SFR, and molecular line and infrared emission radial profiles are presented in the upper part of each figure for the different galaxies of our sample. The model parameters and derived physical quantities are shown in the lower parts of the figures.

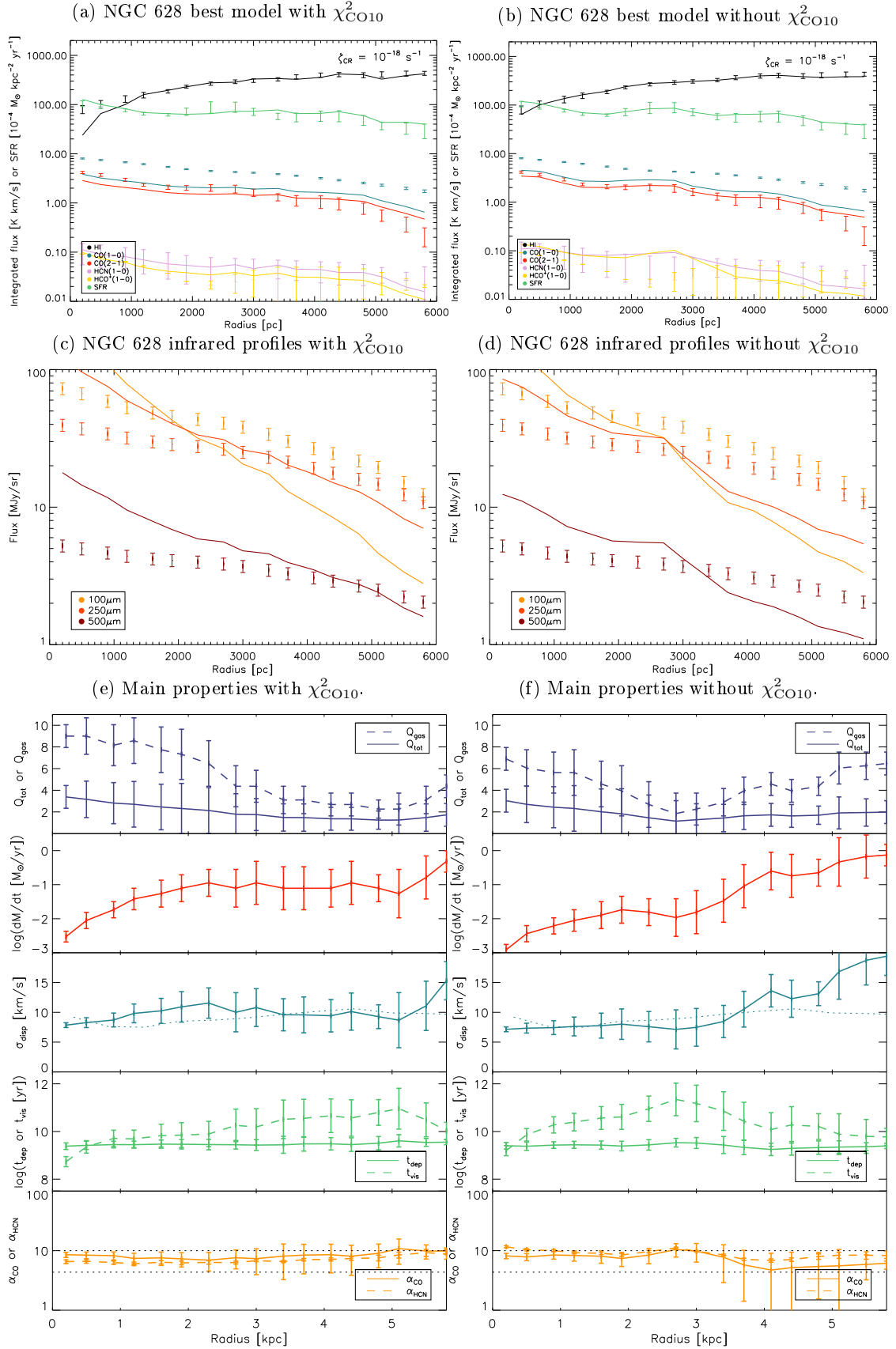


Fig. B.1. NGC 628 best-fit models, infrared profiles, and radial profiles of main physical quantities. See Figs. 1 and 2 for explanations.

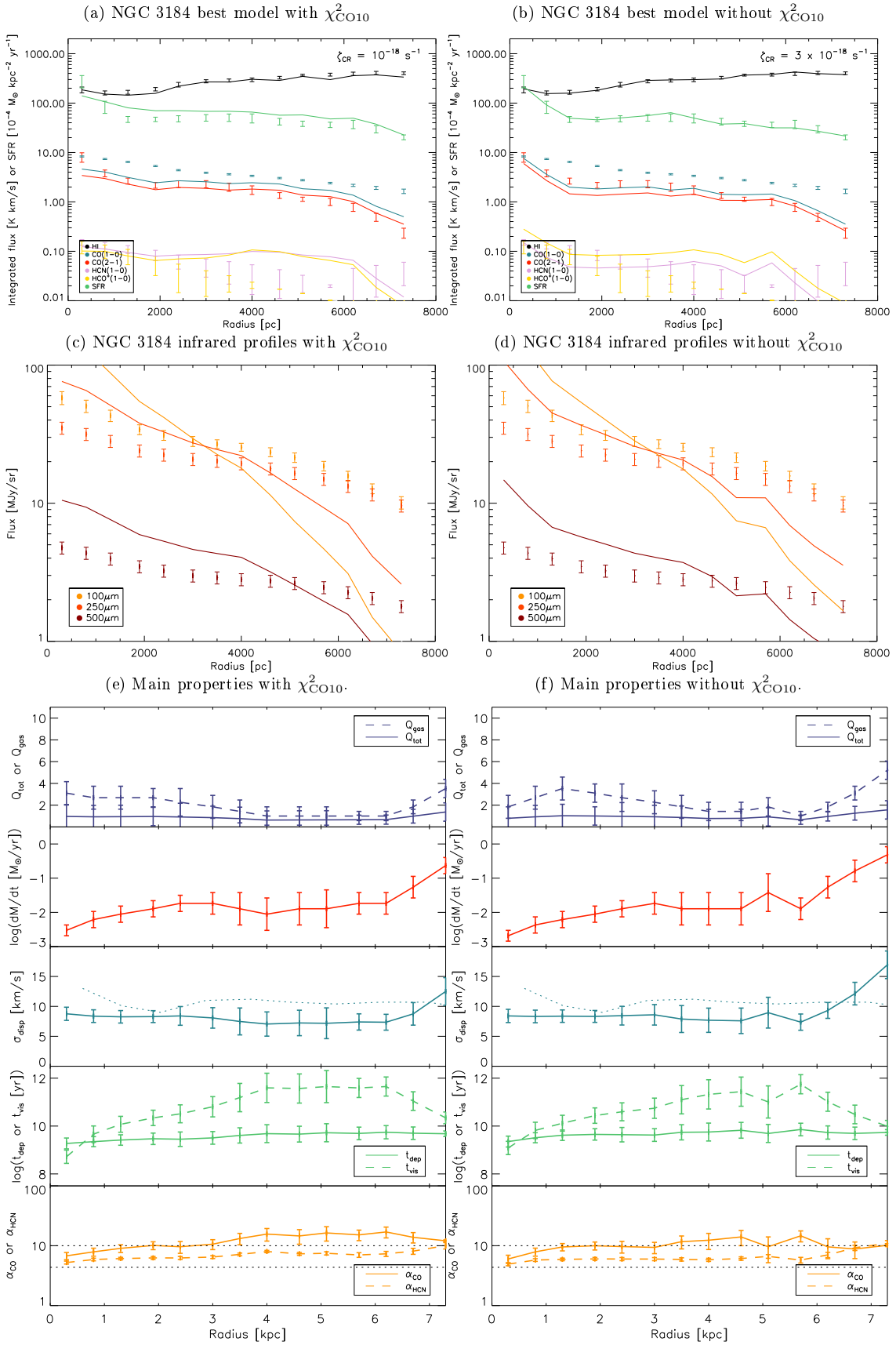


Fig. B.2. Same as Fig. B.1 but for NGC 3184.

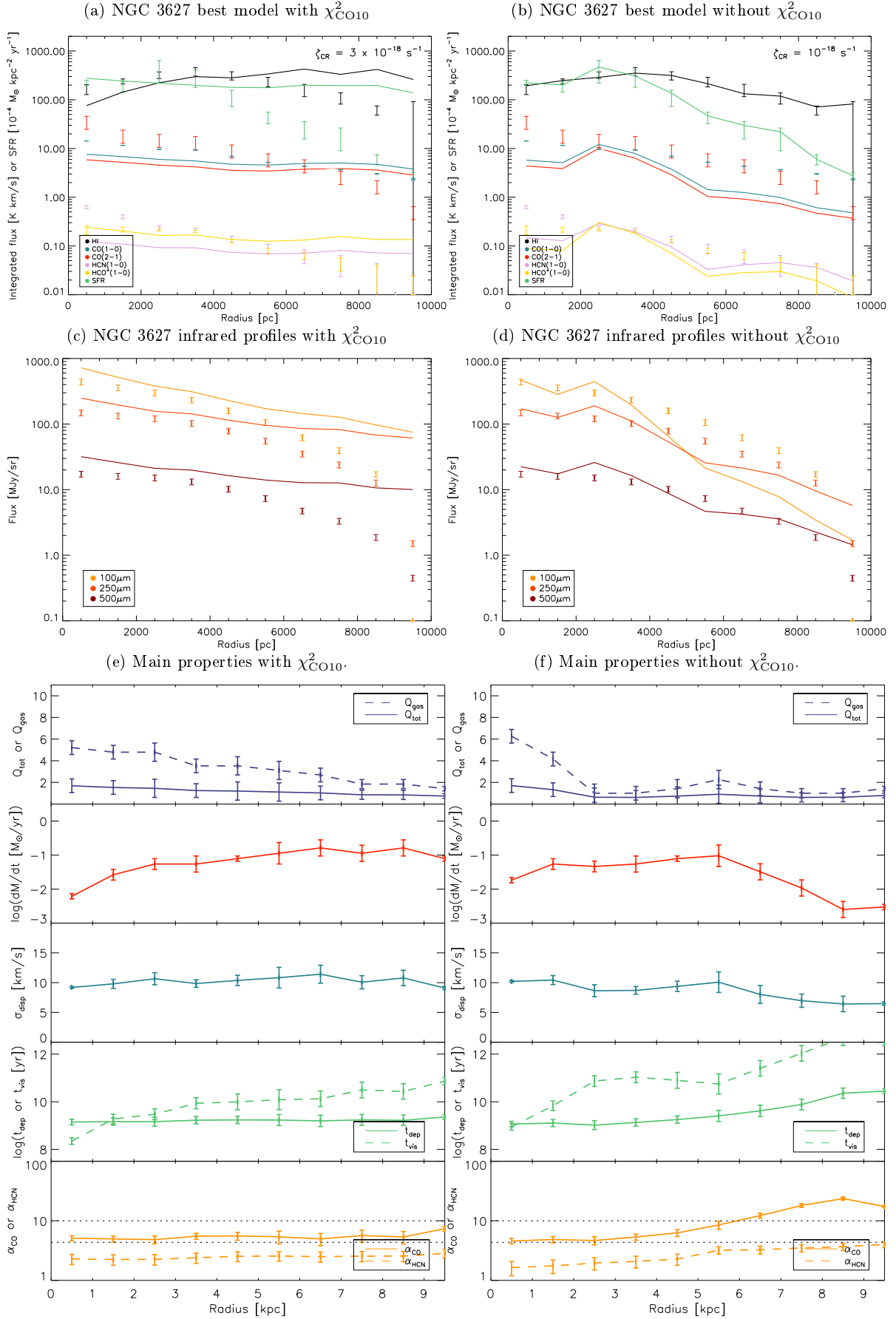


Fig. B.3. Same as Fig. B.1 but for NGC 3627.

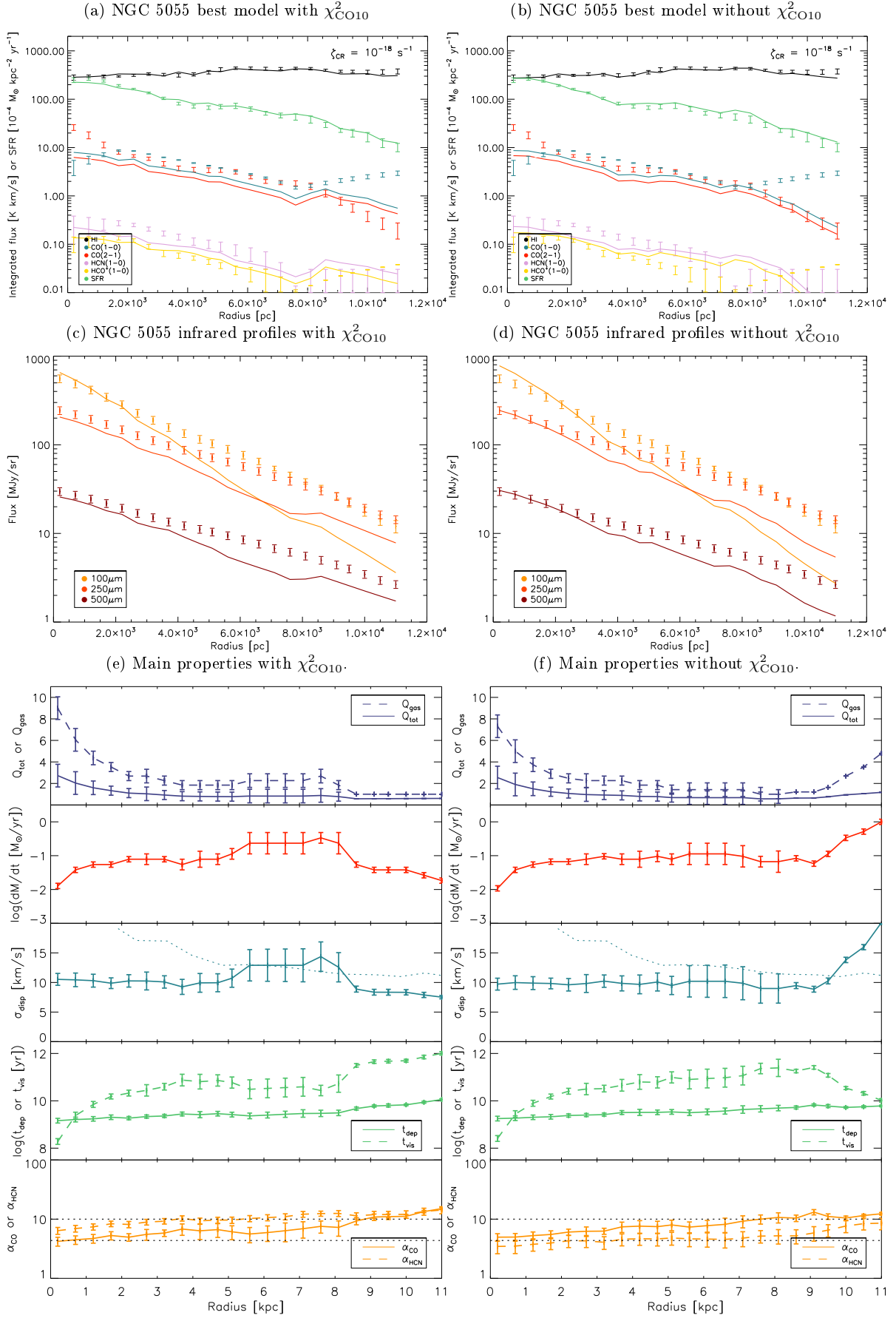


Fig. B.4. Same as Fig. B.1 but for NGC 5055.

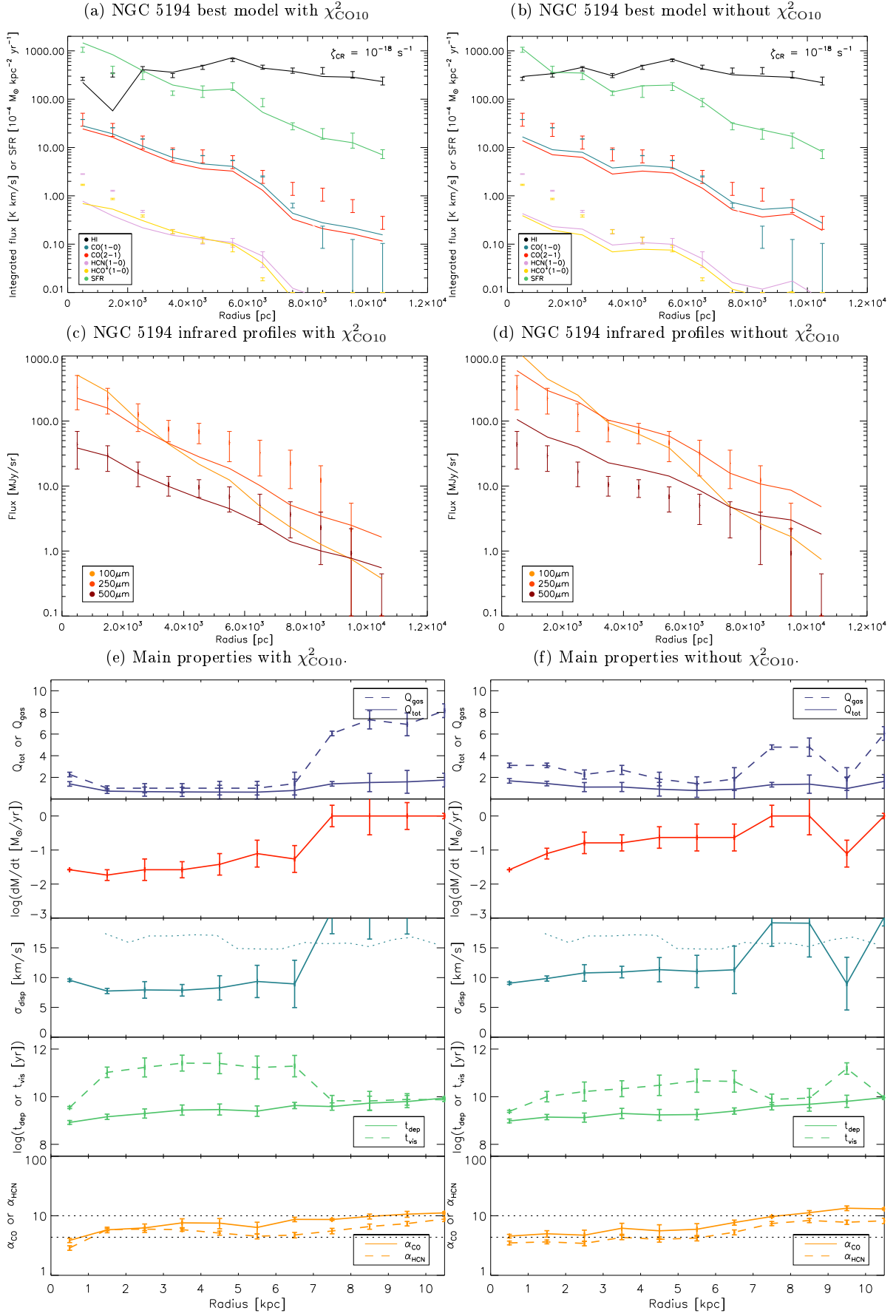


Fig. B.5. Same as Fig. B.1 but for NGC 5194.

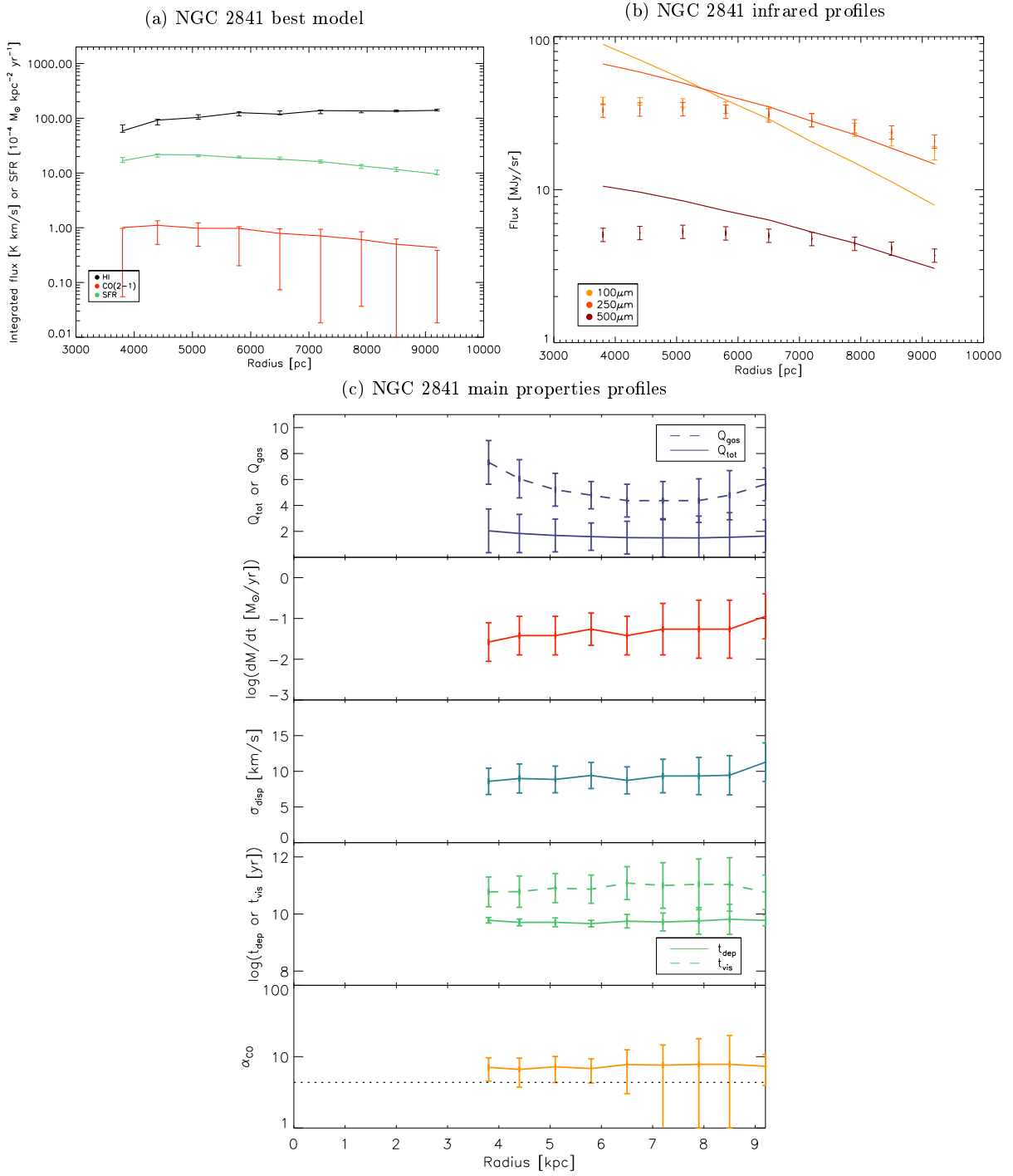


Fig. B.6. Same as Fig. B.1 but for NGC 2841.

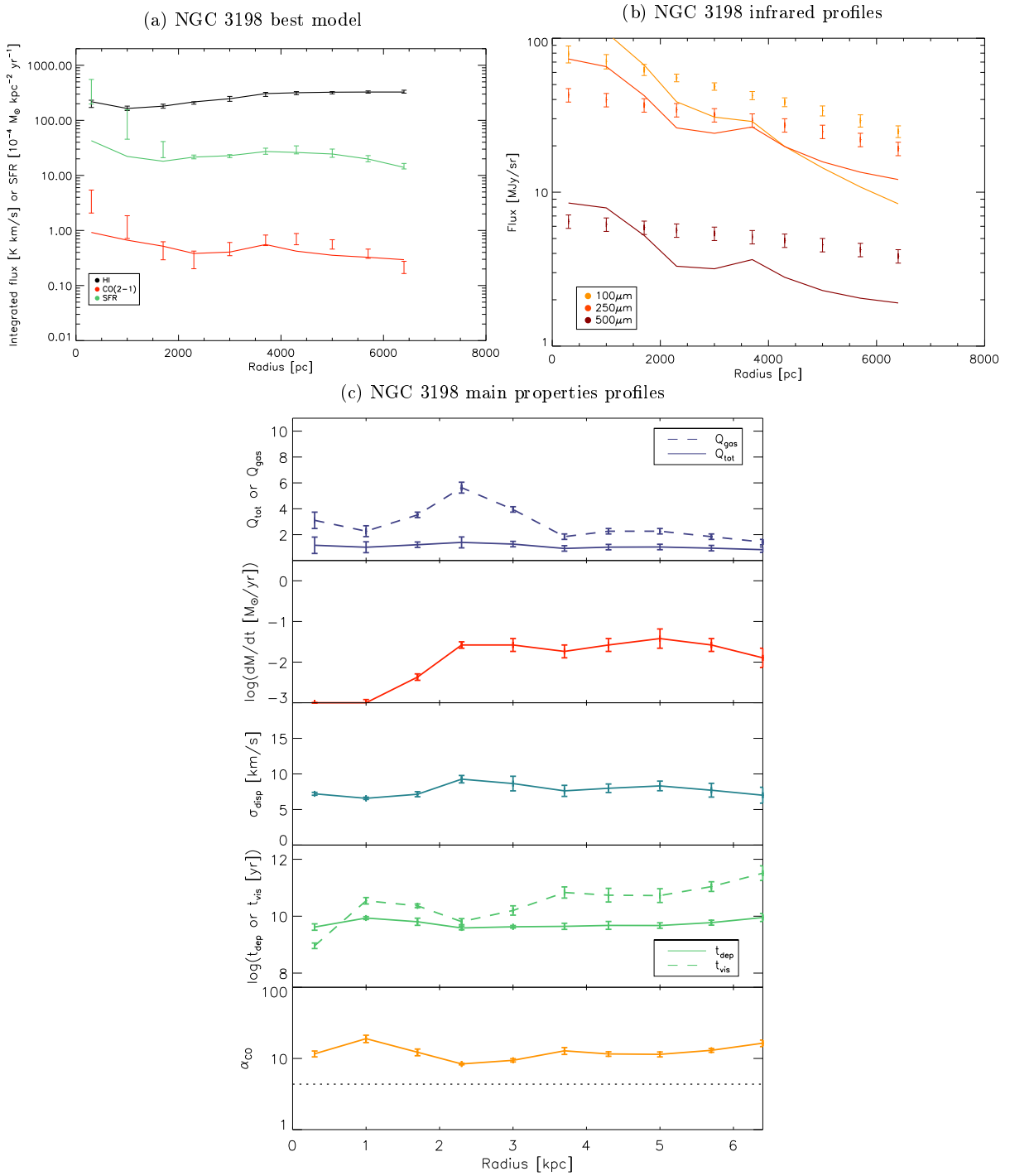


Fig. B.7. Same as Fig. B.1 but for NGC 3198.

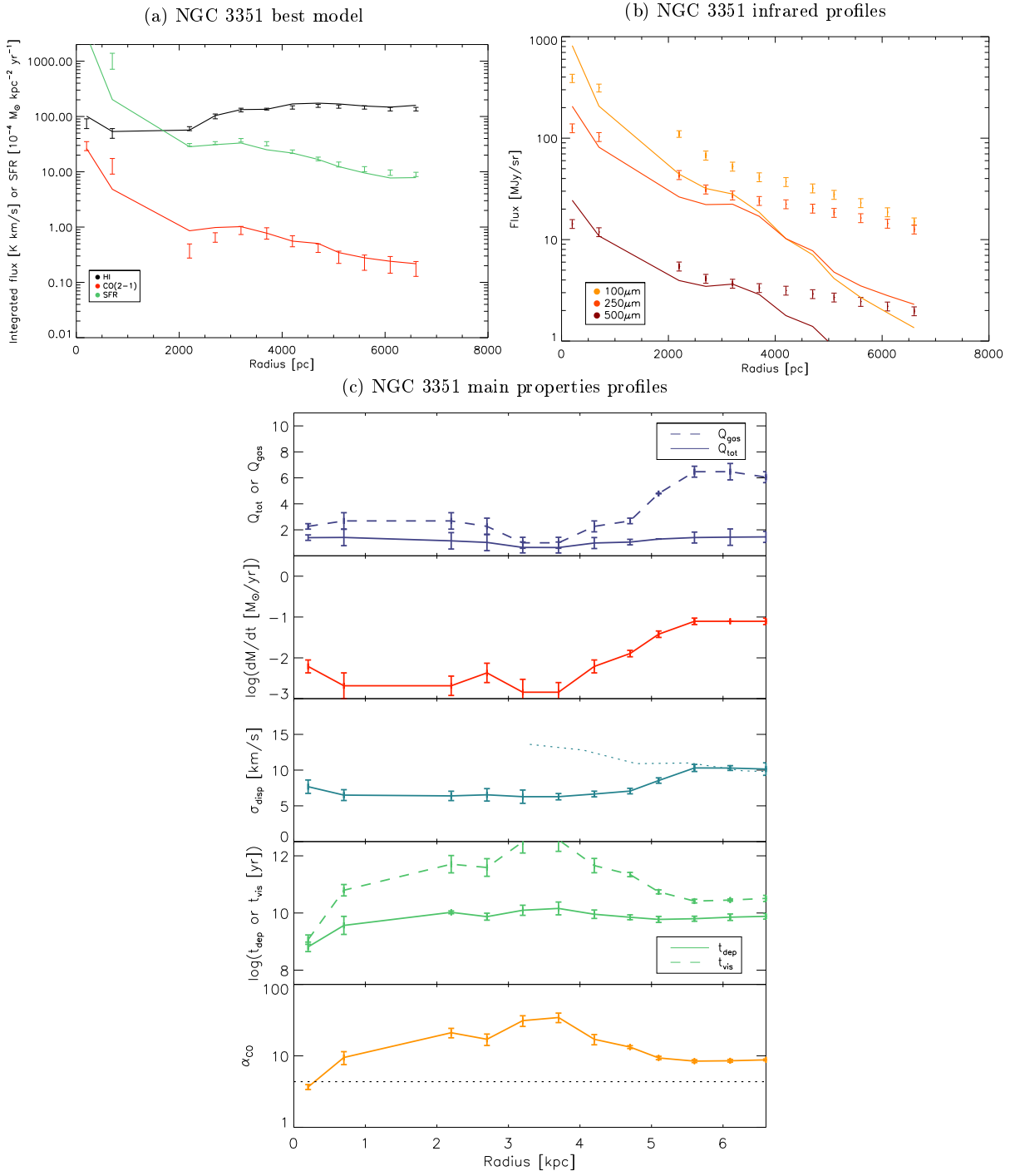


Fig. B.8. Same as Fig. B.1 but for NGC 3351.

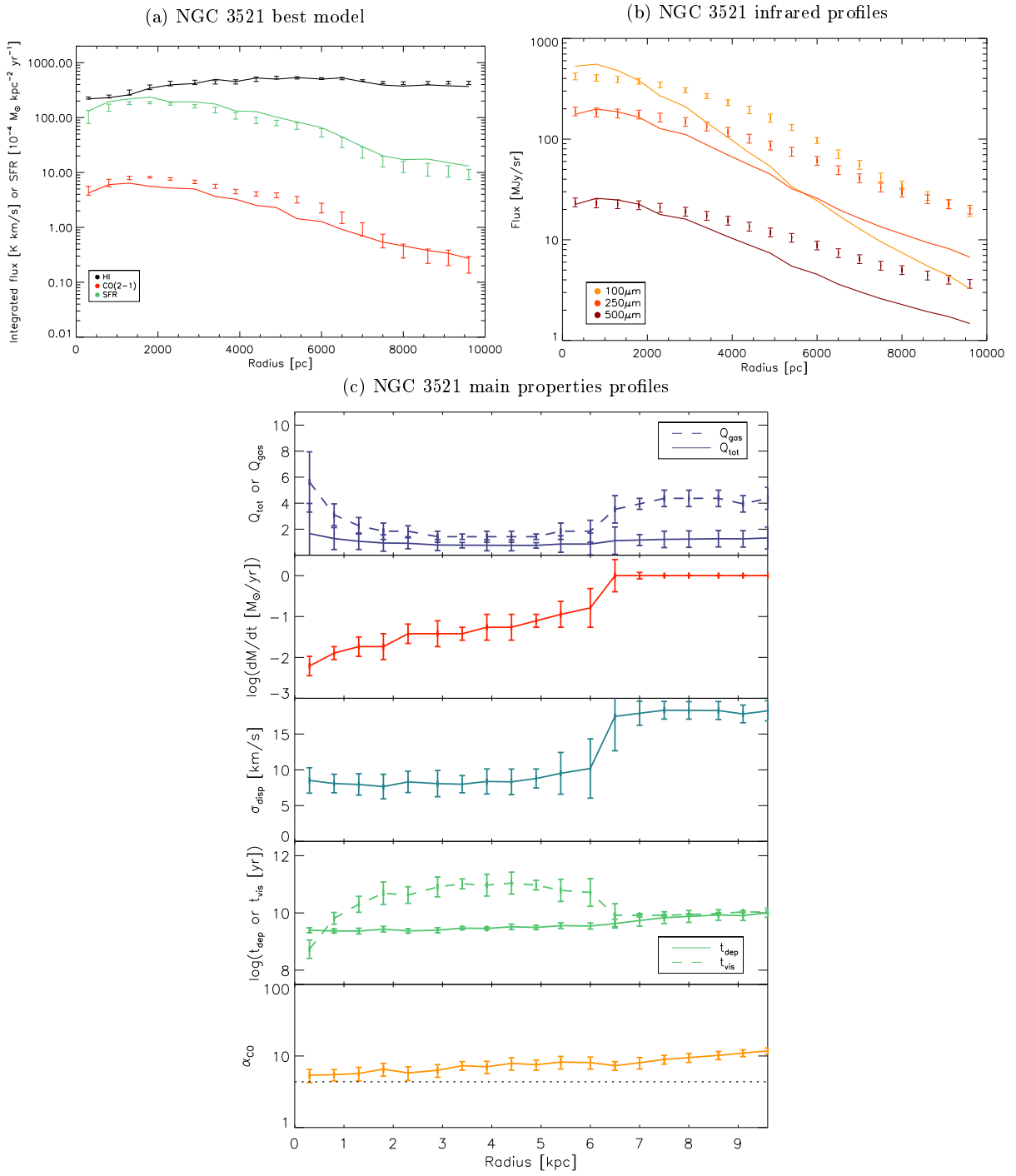


Fig. B.9. Same as Fig. B.1 but for NGC 3521.

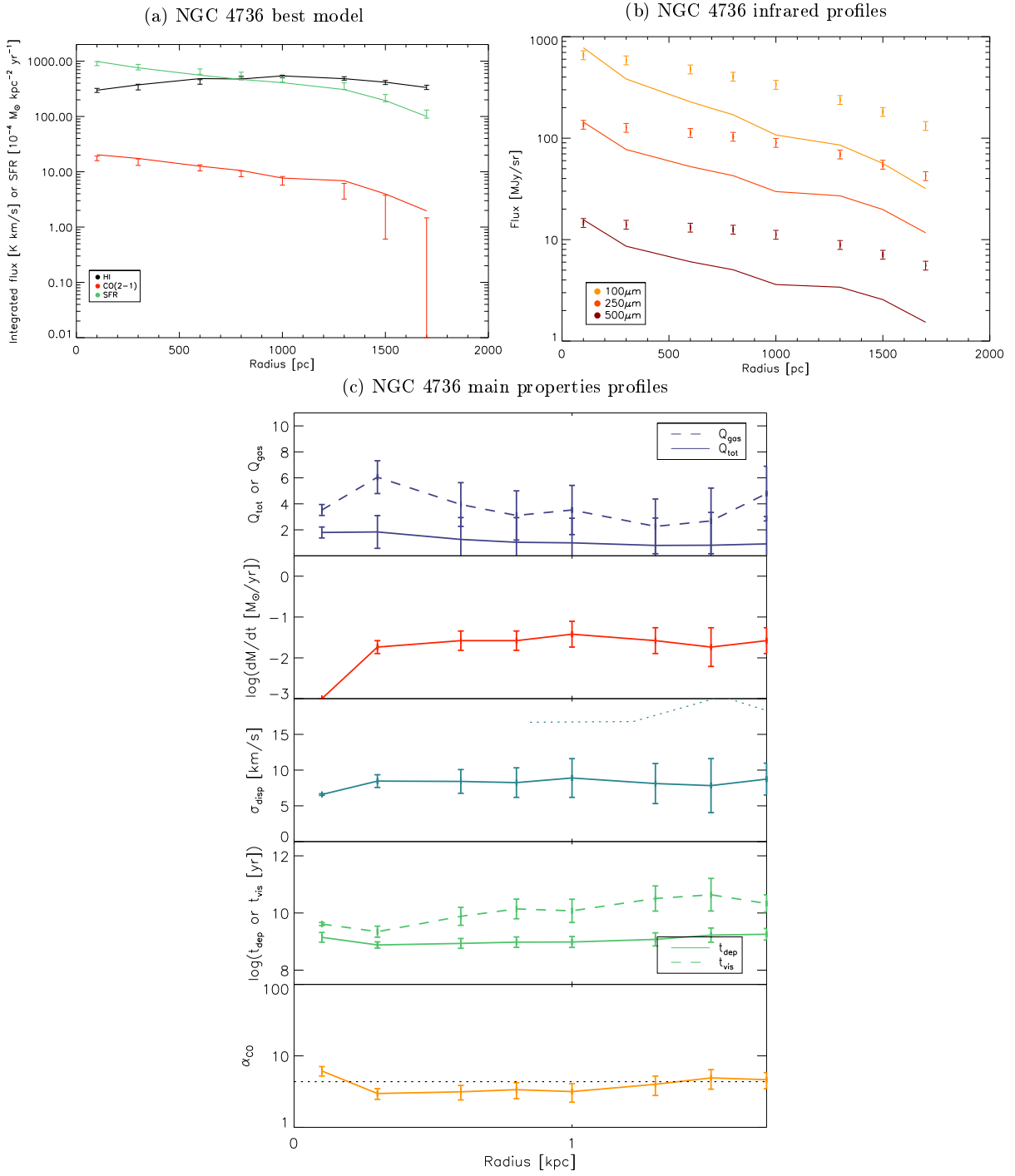


Fig. B.10. Same as Fig. B.1 but for NGC 4736.

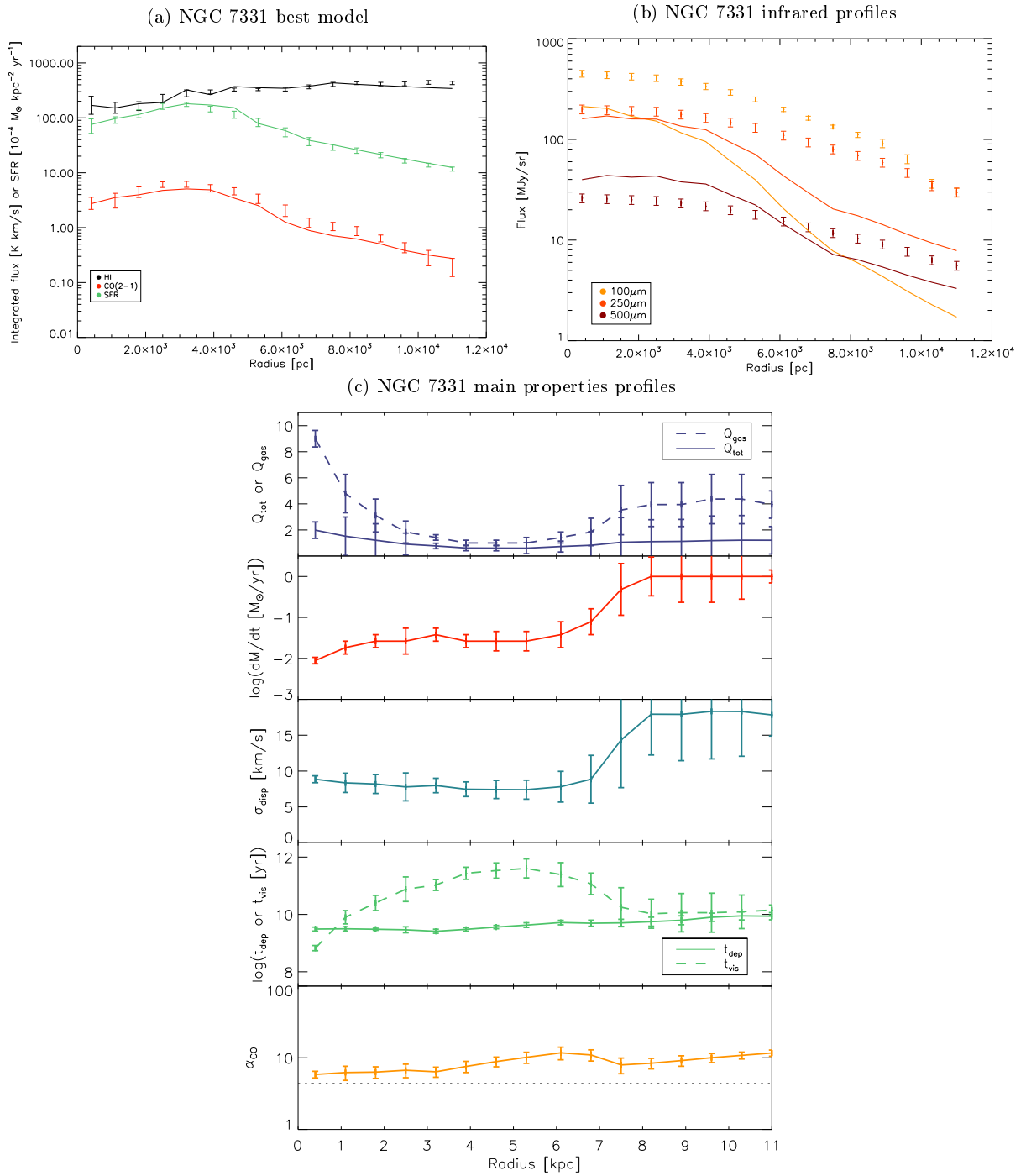


Fig. B.11. Same as Fig. B.1 but for NGC 7331.

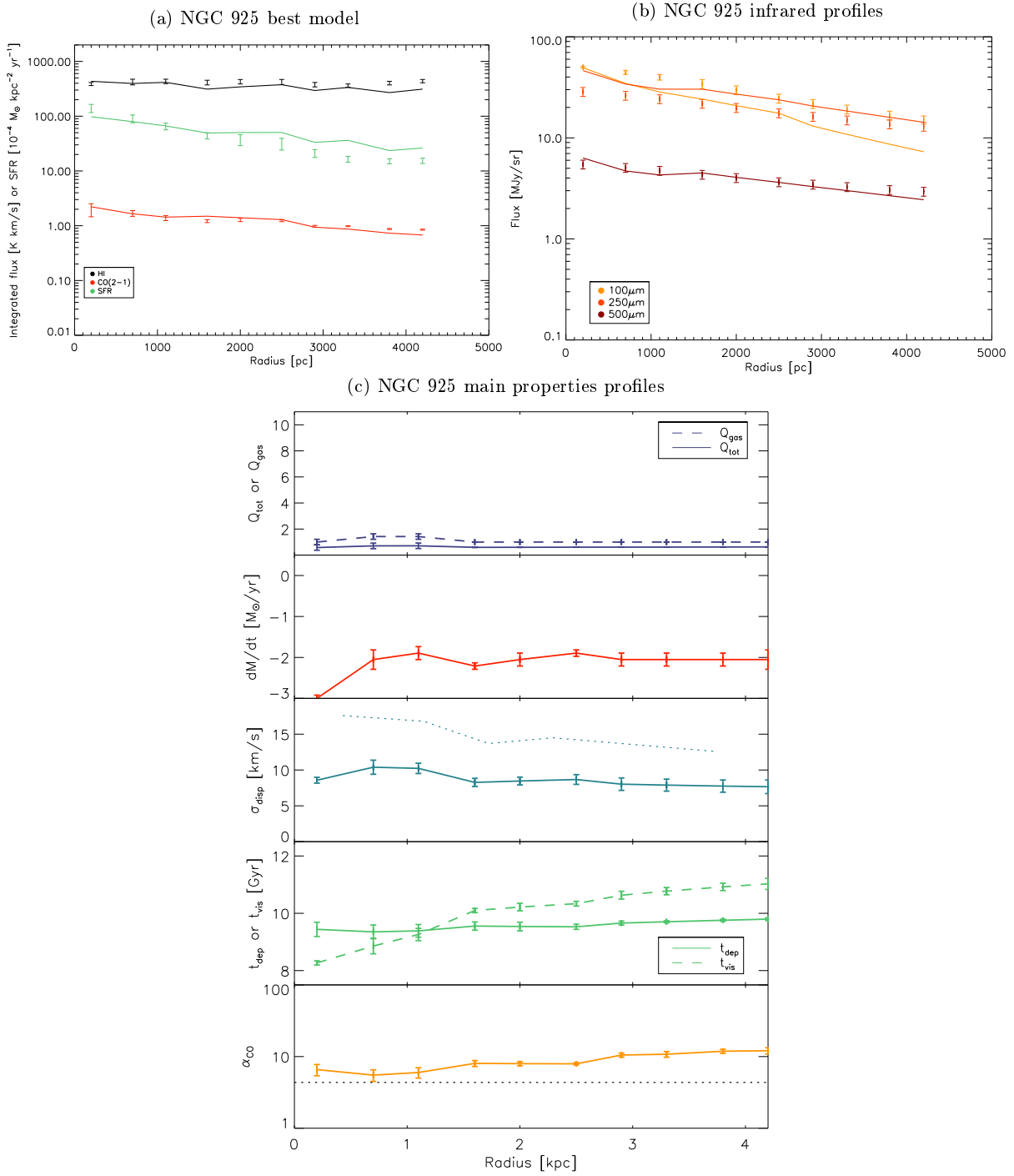


Fig. B.12. Same as Fig. B.1 but for NGC 925.

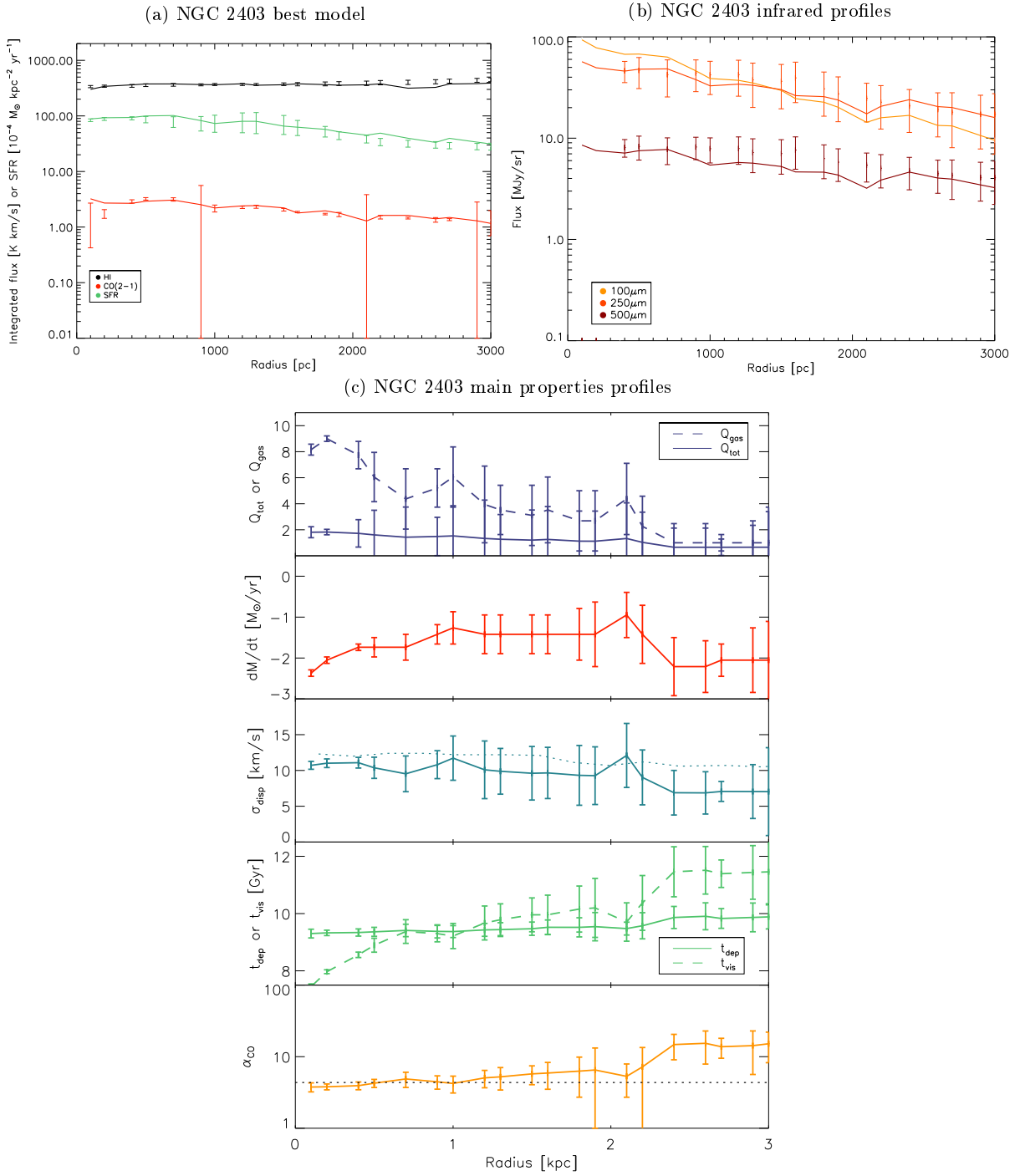


Fig. B.13. Same as Fig. B.1 but for NGC 2403.

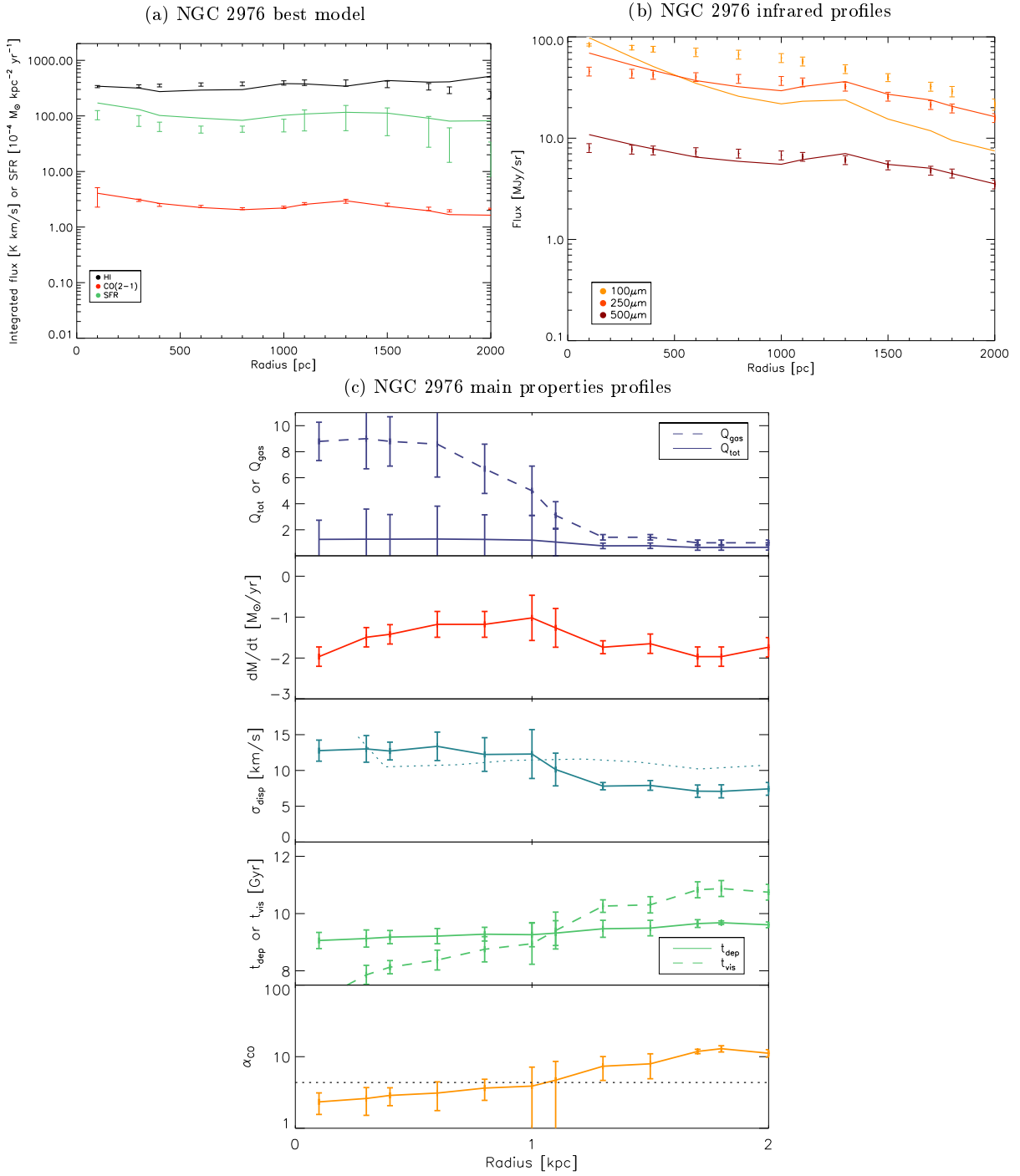


Fig. B.14. Same as Fig. B.1 but for NGC 2976.

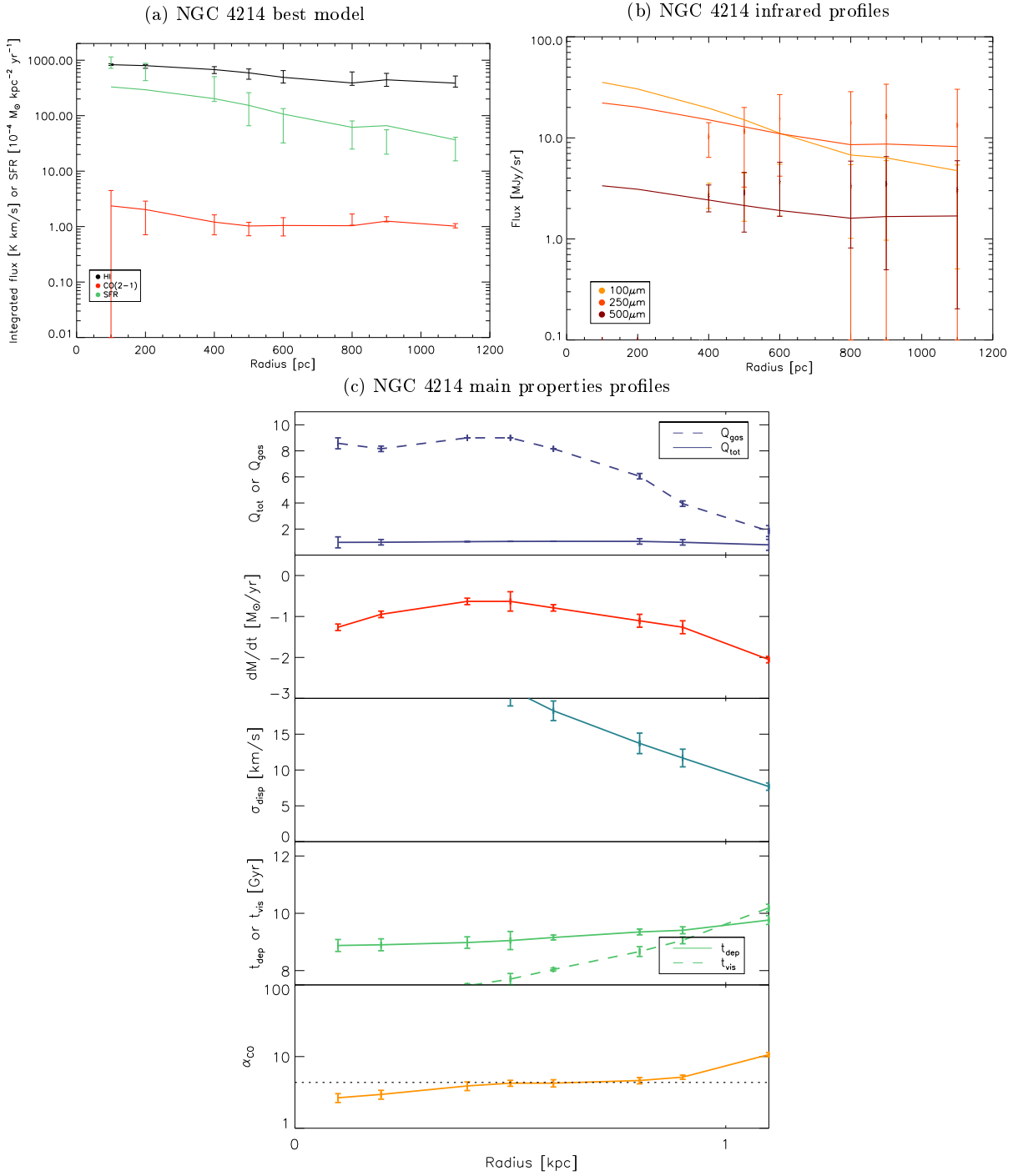


Fig. B.15. Same as Fig. B.1 but for NGC 4214.

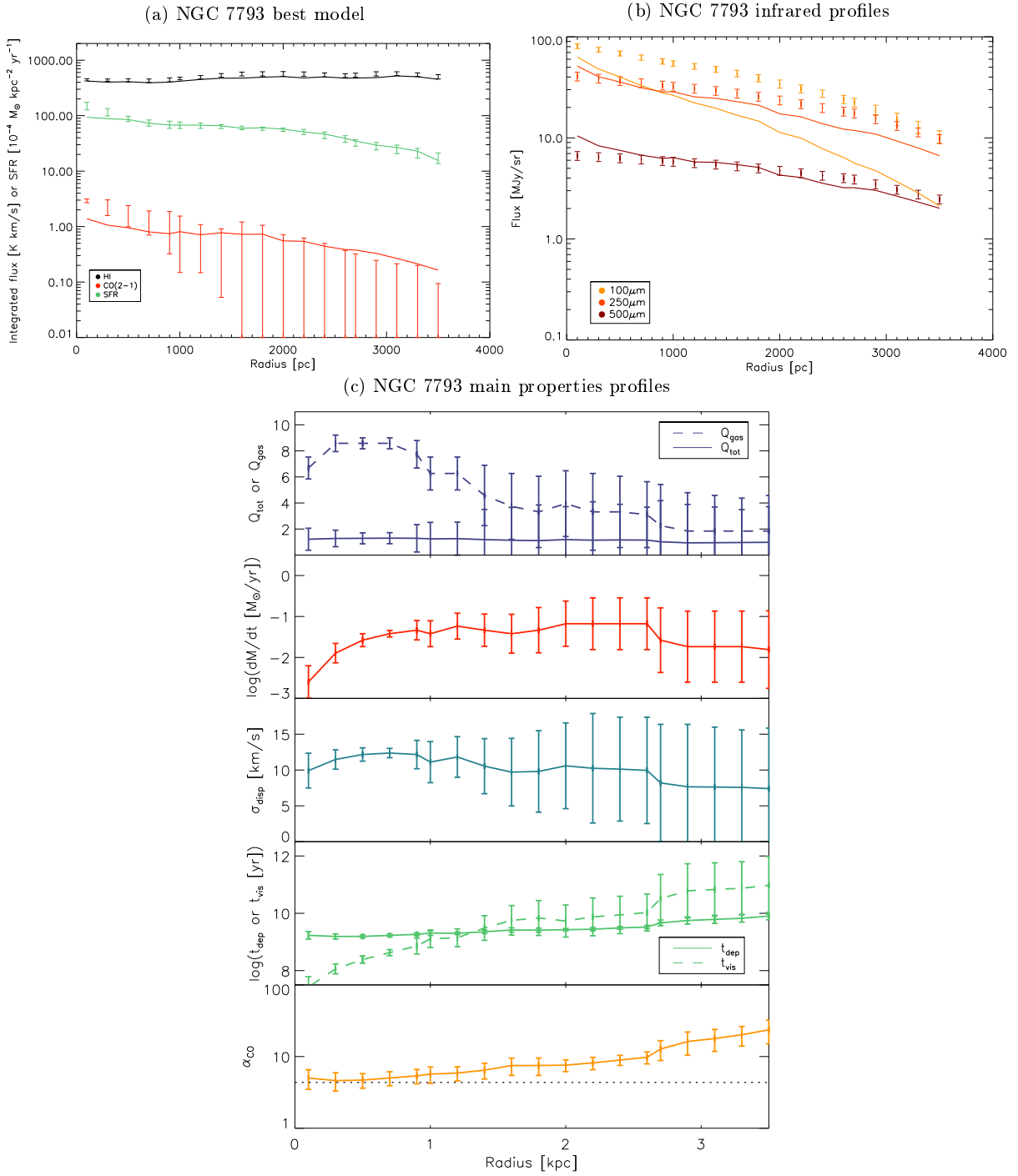


Fig. B.16. Same as Fig. B.1 but for NGC 7793.

Appendix C: Emission from dense gas

The fractions of total flux emitted by gas with densities higher than $n = 10^3$, $10^{3.5}$, 10^4 , and $10^{4.5} \text{ cm}^{-3}$ are presented in Table C.1.

Table C.1. Fraction of the total flux.

Galaxy	Molecule	$n > 10^3 \text{ cm}^{-3}$	$n > 10^{3.5} \text{ cm}^{-3}$	$n > 10^4 \text{ cm}^{-3}$	$n > 10^{4.5} \text{ cm}^{-3}$
NGC628	CO	20 %	9 %	3 %	2 %
	HCN	62 %	50 %	28 %	17 %
	HCO	48 %	31 %	14 %	8 %
NGC3184	CO	13 %	6 %	4 %	1 %
	HCN	53 %	38 %	28 %	10 %
	HCO	39 %	23 %	15 %	4 %
NGC3627	CO	19 %	7 %	4 %	1 %
	HCN	59 %	41 %	31 %	12 %
	HCO	46 %	24 %	16 %	6 %
NGC5055	CO	45 %	11 %	7 %	2 %
	HCN	79 %	48 %	38 %	16 %
	HCO	76 %	31 %	22 %	8 %
NGC5194	CO	39 %	10 %	6 %	2 %
	HCN	80 %	42 %	34 %	15 %
	HCO	69 %	26 %	20 %	8 %
NGC6946	CO	28 %	9 %	4 %	2 %
	HCN	73 %	43 %	25 %	15 %
	HCO	62 %	27 %	13 %	8 %